UNIVERSIDAD NACIONAL AUTÓNOMA DE MÉXICO

POSGRADO EN CIENCIAS FÍSICAS
INSTITUTO DE CIENCIAS NUCLEARES
FÍSICA DE ALTAS ENERGÍAS, FÍSICA NUCLEAR, GRAVITACIÓN Y FÍSICA MATEMÁTICA

ANÁLISIS DE AMPLITUDES EN FÍSICA HADRÓNICA

TESIS
QUE PARA OPTAR POR EL GRADO DE:
DOCTOR EN CIENCIAS (FÍSICA)

PRESENTA:
M. En C. JORGE ANTONIO SILVA CASTRO

TUTOR PRINCIPAL:
DR. CÉSAR FERNÁNDEZ RAMÍREZ
INSTITUTO DE CIENCIAS NUCLEARES / UNIVERSIDAD NACIONAL DE EDUCACIÓN A DISTANCIA

MIEMBROS DEL COMITÉ TUTOR:
DR. ROELOF BIJKER BIJKER
INSTITUTO DE CIENCIAS NUCLEARES
DR. EDUARDO PEINADO RODRÍGUEZ
INSTITUTO DE FÍSICA

CIUDAD UNIVERSITARIA, CIUDAD DE MÉXICO, MÉXICO, FEBRERO DE 2025

PROTESTA UNIVERSITARIA DE INTEGRIDAD Y HONESTIDAD ACADÉMICA Y PROFESIONAL
(Graduación con trabajo escrito)

De conformidad con lo dispuesto en los artículos 87, fracción V, del Estatuto General, 68, primer párrafo, del Reglamento General de Estudios Universitarios y 26, fracción I, y 35 del Reglamento General de Exámenes, me comprometo en todo tiempo a honrar a la Institución y a cumplir con los principios establecidos en el Código de Ética de la Universidad Nacional Autónoma de México, especialmente con los de integridad y honestidad académica.

De acuerdo con lo anterior, manifiesto que el trabajo escrito titulado:

ANÁLISIS DE AMPLITUDES EN FÍSICA HADRÓNICA

que presenté para obtener el grado de ----Doctorado---- es original, de mi autoría y lo realicé con el rigor metodológico exigido por mi programa de posgrado, citando las fuentes de ideas, textos, imágenes, gráficos u otro tipo de obras empleadas para su desarrollo.

En consecuencia, acepto que la falta de cumplimiento de las disposiciones reglamentarias y normativas de la Universidad, en particular las ya referidas en el Código de Ética, llevará a la nulidad de los actos de carácter académico administrativo del proceso de graduación.

Atentamente

JORGE ANTONIO SILVA CASTRO
517025839

(Nombre, firma y Número de cuenta de la persona alumna)

COORDINACIÓN GENERAL DE ESTUDIOS DE POSGRADO

CARTA AVAL PARA DAR INICIO A LOS TRÁMITES DE GRADUACIÓN

Universidad Nacional Autónoma de México
Secretaría General
Coordinación General de Estudios de Posgrado

Dr. Alberto Güijosa Hidalgo
Programa de Posgrado en Ciencias Físicas
Presente

Quien suscribe, **Dr. César Fernández Ramírez**, tutor(a) principal de **Jorge Antonio Silva Castro**, con número de cuenta **517025839**, integrante del alumnado de **Doctorado en Ciencias (Física)** de ese programa, manifiesto bajo protesta de decir verdad que conozco el trabajo escrito de graduación elaborado por dicha persona, cuyo título es:

Análisis de Amplitudes en Física Hadrónica

, así como el reporte que contiene el resultado emitido por la herramienta tecnológica de identificación de coincidencias y similitudes con la que se analizó ese trabajo, para la prevención de faltas de integridad académica.

De esta manera, con fundamento en lo previsto por los artículos 96, fracción III del Estatuto General de la UNAM; 21, primero y segundo párrafos, 32, 33 y 34 del Reglamento General de Exámenes y; 22, 49, primer párrafo y 52, fracción II del Reglamento General de Estudios de Posgrado, **AVALO** que el trabajo de graduación presentado se envíe al jurado para su revisión y emisión de votos, por considerar que cumple con las exigencias de rigurosidad académica previstas en la legislación universitaria.

Protesto lo necesario,

Ciudad Universitaria, Cd. Mx., a 8 de enero de 2025

Dr. César Fernández ramírez

Tutor(a) principal

Con todo mi amor y agradecimiento
a mi familia y amigos, en especial
a mis abuelos Jorge y Josefina,
mis abuelos Mario y Leonor,
a mis padres Lourdes y Antonio,
a mi hermana Montserrat
y a mi amada Danli Yañez.

Agradecimientos Institucionales

Agradezco a la Universidad Nacional Autónoma de México (UNAM) por la oportunidad de realizar mis estudios de Posgrado, así como por todos los apoyos acedémicos y financieros que hicieron posible la conclusión de esta etapa de mi formación profesional.

Asimismo, agradezco al Posgrado en Ciencias Físicas de la UNAM, por todos los servicios y apoyos que me proporcionaron para la realización de mis estudios de posgrado.

De igual manera agradezco al Instituto de Ciencias Nucleares (ICN), por todas las facilidades y apoyos que otorgó durante mis estudios tanto de maestría, como de doctorado.

Agradezco tambíen al Jefferson Laboratory (JLab-USA) por brindarme la oportunidad de realizar una estancia académica en sus instalaciones que contribuyó significativamente a mi desarrollo profesional. Así como a los investigadores y personal del Theory Center de dicho laboratorio.

Especialmente agradezco a todo el personal académico y administrativo tanto del ICN, como del IF y del PCF de la UNAM quienes con amabilidad, empatía y profesionalismo me apoyaron, acompañaron y respaldaron tanto administrativa como personalmente durante todo el proceso de mi posgrado.

Al Consejo Nacional de Ciencia y Tecnología (CONACyT) por el apoyo proporcionado a través de la beca de Posgrado 734789, que me permitiío enfocarme en mis estudios de Doctorado.

Este trabajo ha sido parcialmente apoyado por PAPIIT-DGAPA (UNAM, México) por la beca No. IA10181, No. IA101717 y No. IA101819 y por CONAHCYT (México) a través la beca No. .251817, No. 619970 y proyecto No. A1-S-21389.

Agradecimientos Personales

Este trabajo de tesis representa el cúlmino de un arduo esfuerzo personal y profesional el cual representó por diferentes motivos una tarea muy compleja, pero que finalmente ha sido concluído gracias al apoyo y compañía de personas realmente importantes para mí, por lo que quisiera expresar mi gratitud a:

A mi familia:

En primer lugar, quiero expresar mi más sincero agradecimiento a mis padres, quienes siempre creyeron y confiaron en mí, brindándome su amor incondicional en cada momento. Su ejemplo de dedicación, esfuerzo y resiliencia ha sido mi mayor inspiración. A mi madre, por su fortaleza y por enseñarme el valor de la perseverancia, y a mi padre, por su sabiduría y por inculcarme la importancia de luchar por mis sueños. Sin su guía y apoyo, nada de esto habría sido posible.

A mi hermana, quien ha estado conmigo en las buenas y en las malas, sin importar las circunstancias. Ella no solo es mi gran amiga, sino también uno de los pilares más importantes de mi vida. Le debo tanto, y su cariño, humor y complicidad han sido un faro en los momentos más oscuros.

A mis abuelos, quienes han dejado una huella imborrable en mi vida. A mis abuelos paternos y a mi abuelo materno, quienes ya no están físicamente conmigo, pero su legado de amor, sabiduría y valores sigue vivo en mi corazón. Ellos fueron como unos segundos padres para mí, y su apoyo incondicional durante sus vidas me guió y fortaleció en momentos clave. A mi abuela materna, la única que aún me acompaña, quiero agradecerle por su cariño constante y por ser un pilar de fortaleza en nuestra familia. Su presencia es un regalo que atesoro profundamente.

A mis tíos y primos, quienes forman el núcleo más cercano de mi familia y siempre han estado ahí para celebrar mis logros y apoyarme en los desafíos.

Y de manera muy especial, quiero agradecer a Danli Yañez, mi pareja, por ser mi compañera en este proyecto y muchos otros. Su apoyo constante fue fundamental para concluir este trabajo. Con su amor, motivación y fortaleza, Danli creyó en mí incluso en los momentos más complejos, dándome la fuerza para seguir adelante. Su presencia en mi vida ha sido un regalo invaluable, y le estaré eternamente agradecido por ser mi inspiración, mi refugio en los momentos difíciles y la persona que siempre me impulsa a ser mejor.

A todos, gracias por ser parte de esta etapa tan significativa de mi vida.

Al Doctor César Fernández:

Agradezco profundamente a mi tutor por ser un mentor excepcional, no solo por compartir su vasto conocimiento y experiencia, sino también por brindarme su apoyo incondicional en los momentos más difíciles. Su dedicación y compromiso han sido fundamentales para mi crecimiento académico y personal.

Aprecio enormemente las innumerables horas que dedicó tanto a la supervisión de este trabajo como a mi formación profesional. Gracias a su guía, he podido expandir mi conocimiento y comprensión en diversas áreas de la física, lo que ha enriquecido mi perspectiva y mi pasión por esta disciplina.

Además, quiero reconocer las oportunidades que me brindó, tanto a nivel nacional como internacional, las cuales me permitieron crecer académicamente, conectarme con otros investigadores y explorar nuevos horizontes científicos. Su confianza en mi potencial y su constante motivación han sido un pilar esencial en este camino.

Por todo ello, le estaré eternamente agradecido.

A mis tutores y sinodales:

Agradezco de corazón a mis sinodales por dedicar su valioso tiempo a la revisión y evaluación de este trabajo. Sus comentarios, observaciones y retroalimentación han sido fundamentales para enriquecer el contenido de esta investigación y para fortalecer mi formación académica.

Cada una de sus aportaciones, tanto durante este proceso como a lo largo de mi trayectoria, ha sido una fuente de aprendizaje y crecimiento. Su experiencia y perspectiva han ampliado mi comprensión y me han motivado a seguir mejorando en mi camino como físico.

Por su compromiso, dedicación y apoyo, les expreso mi más sincero agradecimiento.

Contents

Resumen

En esta tesis realiza un análisis de amplitudes en la física hadrónica, abarcando las resonancias bariónicas N^* y Δ^*, el pentaquark $P_c(4312)^+$ y el mesón escalar $f_0(980)$. Se utilizan los principios de la teoría de la matriz-S, la unitariedad, la analiticidad y la simetría de cruce, para mostrar la conexión entre las amplitudes de dispersión y la dinámica cercana al umbral. Las resonancias N^* y Δ^* se investigan mediante las trayectorias de Regge, que mapean el plano de energía en el plano de momento angular complejo. Este método revela propiedades fundamentales de las resonancias utilizando parametrizaciones y métodos de remuestreo, en específico el *bootstrap* para obtener resultados confiables. Los hallazgos proporcionan una mejor comprensión de las estructuras de las resonancias, con indicios de una dinámica más allá del modelo de tres quarks ($3q$) constituyentes. El pentaquark $P_c(4312)^+$, descubierto recientemente por la colaboración LHCb en 2019, se analiza utilizando dinámicas de canales acoplados. Este análisis lo describe como un estado virtual, determinado a partir de su comportamiento de polos en las hojas de Riemann, representando un avance en su interpretación estructural. En cuanto a la resonancia $f_0(980)$, este análisis confirma su naturaleza dinámica, indicando que está moldeada por las interacciones $K\bar{K}$. Las metodologías estadísticas, especialmente las técnicas de remuestreo bootstrap, aumentan la robustez y validan los resultados. Este trabajo combina métodos fenomenológicos con datos experimentales, estableciendo una base sólida para el análisis multicanal.

Abstract

This thesis performs an amplitude analysis in hadronic physics, covering the N^* and Δ^* baryonic resonances, the hidden-charm pentaquark $P_c(4312)^+$, and the scalar meson $f_0(980)$. It uses S-matrix theory principles like unitarity, analyticity, and crossing symmetry to show the connection between scattering amplitudes and near-threshold dynamics. The N^* and Δ^* resonances are investigated using Regge trajectories, which map the energy plane into complex angular momentum. This method exposes fundamental properties of the resonances using parameterizations and bootstrap methods for stable results. The results provide a better understanding of resonance structures that goes beyond the $3q$ constituent model. The recently discovered $P_c(4312)^+$ by the LHCb collaboration in 2019, is investigated using coupled-channel dynamics. This analysis renders it as a virtual state, extracted from its pole behavior on Riemann sheets, furthering its structural interpretation. For the $f_0(980)$ resonance, this analysis argues that its dynamical nature since it is moulded by the $K\bar{K}$ interactions. Statistical methodologies, especially bootstrap resampling techniques, increase robustness and validate results. This work combines phenomenological methods with empirical experimentation, laying a base for multi-channel analysis.

1. Introduction

Science is a way of life. Science is a perspective. Science is the process that takes us from confusion to understanding in a manner that's precise, predictive and reliable - a transformation, for those lucky enough to experience it, that is empowering and emotional.

B. Greene

The current theory of the strong interaction, quantum chromodynamics (QCD) is a nonabelian quantum field theory whose fundamental fields are the quarks (q) and the mediator gauge boson is the gluon (g). The local gauge symmetry is $SU(3)$ and the strong charge is named color [1]. The fact that QCD is nonabelian has deep implications which can be better understood when compared to the quantum field theory of the electromagnetic interaction, i.e. quantum electrodynamics (QED) [2]. QED is based on a $U(1)$ local symmetry, which implies that there is only one *electric charge* which can be either positive, negative or null. There is only one force mediator, the photon, whose electric charge is null. The fact that the photon does not carry electric charge is what makes the theory abelian, and, hence, respect the superposition principle, which is one of the fundamental properties of Maxwell's electromagnetic field equations. In QCD, the $SU(3)$ gauge symmetry implies the existence of three different color charges known as *red*, *green* and *blue*, as well as their respective *anti-colors*. Instead of one mediator as in QED, in QCD we have eight different gluons that actually carry color charge. This implies that the gluons have self-interactions,– we have three and four gluon vertices–, and QCD does not satisfy the superposition principle [3].

In QED it is possible to observe the photons, electrons and positrons (they are part of the spectrum of the theory), but, in QCD it is not the case due to an emergent phenomenon known as *color confinement*. This means that the spectrum is made of

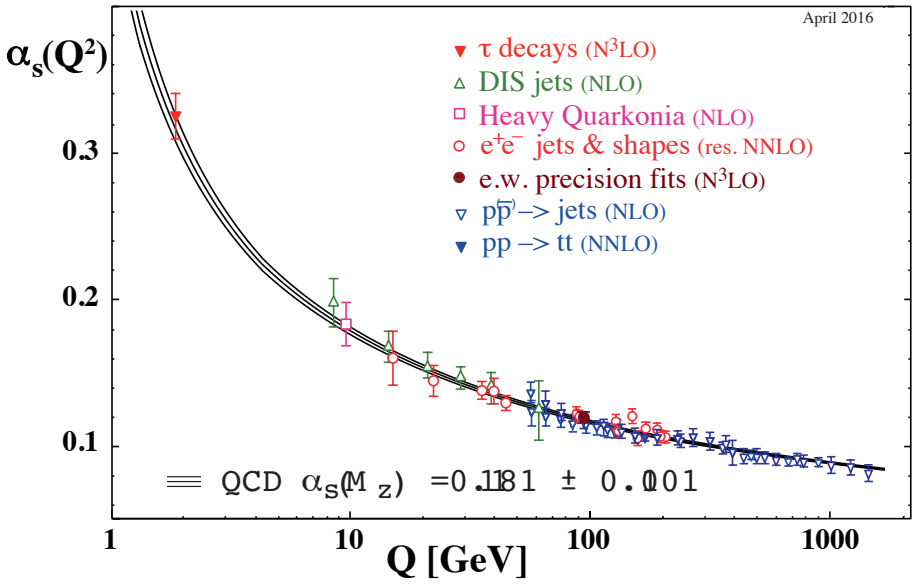

Figure F.1.1: Energy dependence of the strong interaction coupling constant α_s as a function or the energy scale Q. Figure taken from the Review of Particle Physics [8].

color singlets only, in other words, the quark and gluon fields combine in such a way that the resulting asymptotic states are colorless [4]. The particles that conform the spectrum of the theory are called *hadrons*, which are classified into two categories: *mesons* if they are bosons; and (anti)*baryons* if they are fermions.

The typical way to perform calculations in QED (and in general in a quantum field theory) consists on using perturbative techniques. In order to do this, it is necessary that the theory can be expanded in a small parameter, usually the coupling constant, in the energy regime of interest. In QCD this expansion is only possible in the so called *asymptotic freedom* region, i.e. at high energies. In the low energy region of QCD, where the masses of the hadrons lie, the value of the strong coupling constant (see figure F.1.1) does not allow for perturbative treatment of the interaction.[1]

One of the most important challenges of physics is to understand the strong interaction in the nonperturbative regime as well as how quarks and gluons are confined inside hadrons. One of the ways to obtain insight is to study the hadron spectrum, i.e. the color singlets of QCD. The strategy is analogous to that used in

[1]There are other *perturbative* approaches to QCD, for instance the chiral perturbation theory [5], effective lagrangian methods [3], and perturbation theory in the large number of colours (*large* N_c) [6, 7], but those are beyond the interests of this work.

the study of the atomic levels of atoms. The difference is that in the case of atomic physics, the object under study is the discrete part of the spectrum, i.e. the bound states, but in hadron physics, one focuses on the continuum part, i.e. the scattering states.

Most of the hadrons have a short half-life ($\sim 10^{-24}$s) and are called *resonances*, studied in particle accelerators. Once the different experimental collaborations collect data, it is necessary to do an amplitude analysis to determine, or discard, the existence of a hadronic state and to study the dynamics responsible for its generation.

The S-matrix theory [9], using general properties of the scattering amplitudes such as relativistic invariance, spectral decomposition, unitarity, and causality, provides a framework that allows us to extract the QCD states, and analyze the reaction processes as well as experimental data, avoiding some of the several underlying problems using the Lagrangian approach in QCD [10].

As mentioned, the hadrons conform the spectrum of QCD and they are colorless. The simplest way to construct a meson is with a pair quark-antiquark $q\overline{q}$, and for a baryon combining three quarks qqq (or three antiquarks $\overline{qqq}$ for an antibaryon). These configurations for mesons and baryons are known as the *minimal quark model* and was proposed by Gell-Mann [11], Petermann [12] and Zweig [13].[2] In figure F.1.2 the ground states for mesons and baryons with constituent quarks u, d, s and c in the minimal quark model are shown. The minimal quark model provides a classification system for hadrons, as well as an excellent description for the ground states of the spectrum. Quark models are beyond the interest of this work and more information can be found in the literature, for example [16].

However, QCD does not require that hadrons have to adhere to the minimal quark model. Hadrons can entertain more complicated structures and baryons or mesons that go beyond the three quark or quark-antiquark pictures are not precluded by QCD. Therefore, for baryons, it is possible to have hybrid states with gluonic components ($qqqg$, $qqqgg$, ...), pentaquarks $qqq\overline{q}q$, heptaquarks $qqq\overline{q}q\overline{q}q$ and so on. For mesons, the situation is analogous and we can have, for instance, tetraquarks $q\overline{q}q\overline{q}$, etc. For

[2]Petermann developed the quark model at the same time as Gell-Mann and Zweig, although he has not been acknowledged in textbooks. Such unfairness in being corrected thanks to articles like the ones by De Rújula [14] or Glashow [15], which set the record straight.

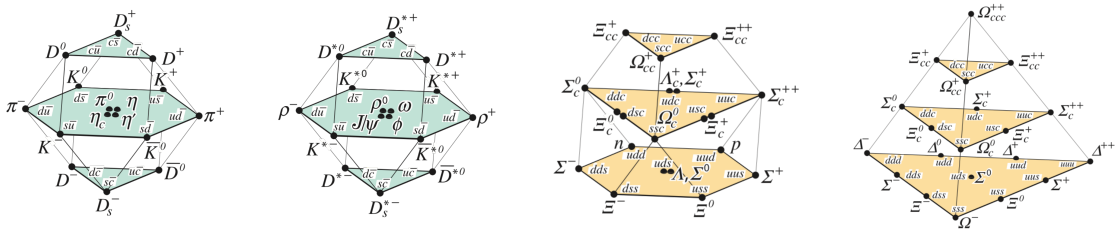

(a) (b) (c) (d)

Figure F.1.2: Ground states in the minimal constituent quark model for mesons [(a) and (b)] and baryons [(c) and (d)] with constituent quarks u, d, s and c. Figure taken from the Review of Particle Physics [8].

example, one can write the general wave function of a meson as:

$$|\text{Meson}\rangle := a_0 |q\bar{q}\rangle + a_1 |q\bar{q}g\rangle + a_2 |q\bar{q}gg\rangle + a_3 |q\bar{q}q\bar{q}\rangle + \cdots \tag{1.1}$$

where the coefficients a_i determine the probability of measuring a specific component and $\sum_i |a_i|^2 = 1$.

An exotic QCD state is a resonance that does not fit within the minimal quark model. There are three kinds of exotic hadrons:

1. States whose quantum numbers cannot be obtained through $q\bar{q}$ o qqq combinations. For a meson, a state of this kind would have $a_0 = 0$ in equation (1.1). The $\pi_1(1600)$ and the $T_{cc}(3875)$ are examples of this kind.

2. States whose minimal quark content cannot be explained through $q\bar{q}$ o qqq combinations. The hidden charm pentaquarks observed by LHCb [17–19] in the $J/\psi p$ spectrum are an example of this kind as their minimal quark content is $c\bar{c}uud$.

3. States whose minimal quark content can be explained through $q\bar{q}$ o qqq combinations, but present properties that indicate that the internal dynamics go beyond such a simple explanation. The $X(3872)$ is the paradigmatic example.

The search for exotic states of QCD [16] has driven a new golden era for hadron spectroscopy, mainly thanks to the numerous experiments of subnuclear physics

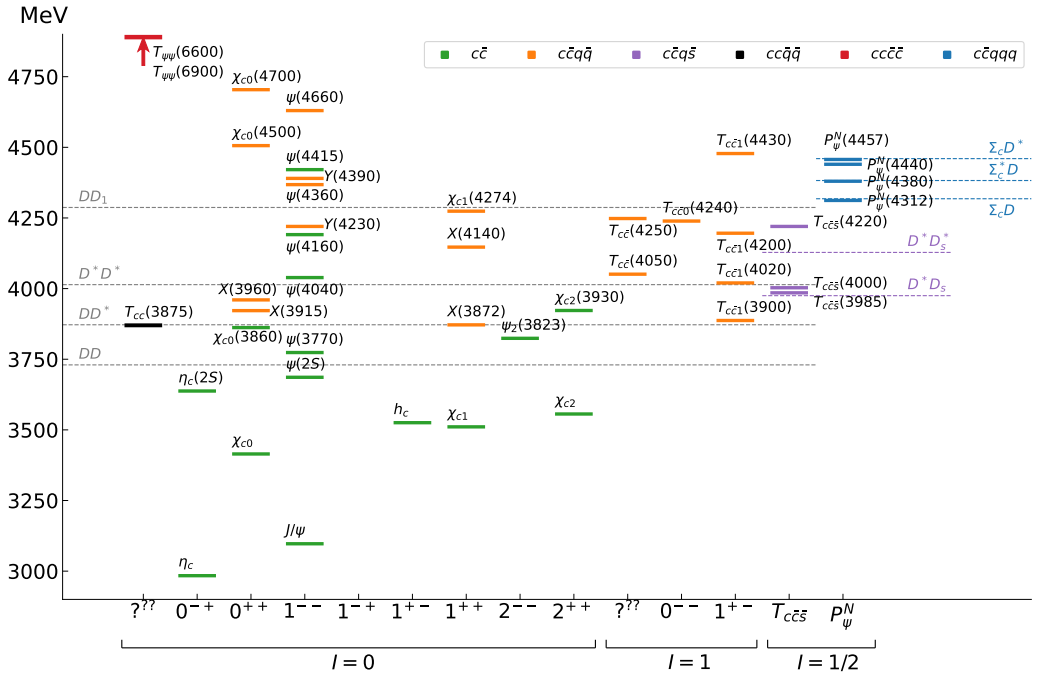

Figure F.1.3: Current spectrum of charmonia and charmonia-like states. Figure from [20] adapted from figure 22 in Ref. [21].

carried out and the many exotic hadrons that have been discovered in the last 20 years. Figure F.1.3 shows the charmonia and charmonia-like spectrum, highlighting the valence quarks of each state.

Amplitude analysis is the tool that allows us to study the experimental data and to determine the existence and properties, i.e. mass, width and residue, of a resonance. In this thesis we use Regge theory and phenomenology and amplitude analysis techniques for near-threshold resonances to study several cases of interest. The theory and methodology employed in this thesis is described in chapter 2. Specifically, the theory is applied to three cases of interest. In chapter 3.1 we study the low-lying nonstrange baryon spectrum to survey deviations from the expected patterns from Regge phenomenology in order to identify missing states and nonordinary states. Chapter 3.2 studies the near-threshold $P_c(4312)^+$ resonance discovered by LHCb [19] within the general principles of the S-matrix theory. This analysis also compares various parametrizations, enabling a comprehensive study of $P_c(4312)^+$ in light of other theoretical models. The obtained results allow more clarity in understanding the structure of the resonance itself and help refine models

already existing about hadron dynamics near thresholds. Chapter 3.3 applies the same ideas to the near $K\bar{K}$ threshold resonance $f_0(980)$. Both $P_c(4312)^+$ and $f_0(980)$ are prime candidates for a molecular resonance generated by the opening of a new threshold. Finally, chapter 4 provides the conclusions of this thesis.

2. Theoretical framework

For a physicist mathematics is not just a tool by means of which phenomena can be calculated, it is the main source of concepts and principles by means of which new theories can be created.

F. Dyson

In this chapter we present the mathematical and physical tools that will be employed in this doctoral research without being exhaustive in its presentation, referring the reader to the corresponding literature. We will emphasize the underlying physical principles. The presented theory is for spinless particles and electromagnetic effects are neglected. However, the results are general, as the extension to particles with spin adds a layer of complexity that can be reduced to the combination of scalar amplitudes like the ones for spinless particles. More information on the inclusion of spin can be found in Refs. [9, 22–31].

2.1 Kinematics of particle scattering

A general and systematic treatment of the principles of special relativity and particle kinematics can be found in many graduate textbooks (see for example [32, 33]). In this section we review some of the main features that will be needed latter in this work.

We start with the $1 + 2 \to 3 + 4$ process, also called $2 \to 2$ reaction because it involves two particles in the initial state and another two in the final. The process is depicted in figure F.2.1. In this reaction, the particles 1 and 2 with four-momenta p_1, p_2, respectively, collide and after the collision the particles 3 and 4 with four-momenta p_3 and p_4 emerge.

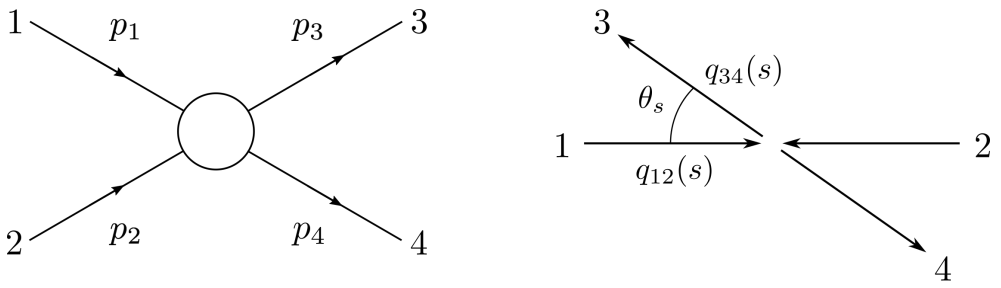

(a) (b)

Figure F.2.1: (a) General $2 \to 2$ reaction, p_i stands for the four-momentum of the ith particle. (b) Reaction $1 + 2 \to 3 + 4$ in the center of mass (CM) system, $q_{12}(s)$ and $q_{34}(s)$ stand for the momentum before and after the collision, respectively, and θ_s is the scattering angle.

The conservation of energy and momentum is expressed as follows:

$$p_1 + p_2 = p_3 + p_4, \tag{2.1}$$

and the asymptotic states, i.e. free states after the collision must be *on shell*, meaning $p_i^2 = m_i^2$ for $i = 3, 4$.

Due to four-momentum conservation (2.1), the momentum vectors $\boldsymbol{p}_i$ of the final particles cannot vary arbitrarily for a fixed initial state. In general, if there are n particles in the final state, the four-momentum conservation imposes the conditions:

$$E_1 + E_2 = \sum_{i=3}^{n+2} E_i, \tag{2.2a}$$

$$\boldsymbol{p}_1 + \boldsymbol{p}_2 = \sum_{i=3}^{n+2} \boldsymbol{p}_i. \tag{2.2b}$$

We shall call the $3n$ dimensional space of unconstrained final state momentum vectors $\boldsymbol{p}_i$ the *momentum space*. The conditions (2.2) define in this space a $3n - 4$ dimensional surface which is called the *phase space*.

For the $2 \to 2$ process we can define the *Mandelstam variables*, which are Lorentz

invariant quantities and are given by [32]:

$$s = (p_1 + p_2)^2 = (p_3 + p_4)^2, \tag{2.3a}$$
$$t = (p_1 - p_3)^2 = (p_2 - p_4)^2, \tag{2.3b}$$
$$u = (p_1 - p_4)^2 = (p_2 - p_3)^2. \tag{2.3c}$$

They satisfy the equality:

$$s + t + u = \sum_{i=1}^{4} m_i^2, \tag{2.4}$$

equation (2.4) implies that only two Mandelstam variables are independent for a given reaction.

Because they are Lorentz invariant scalars, the Mandelstam variables can be evaluated in an arbitrary coordinate system. The simplest choice is the center of mass (CM) frame, where $\boldsymbol{p_1} = -\boldsymbol{p_2}$ and $\boldsymbol{p_3} = -\boldsymbol{p_4}$, depicted in panel (b) of figure F.2.1. In this system the variable s represents the square of the total center-of-mass energy of particles 1 and 2, or 3 and 4.

The particle four-momenta in the CM system reads: $p_1 = (E_1, q_{12}(s))$, $p_2 = (E_2, -q_{12}(s))$, $p_3 = (E_3, q_{34}(s))$, $p_4 = (E_4, -q_{34}(s))$, and the Mandelstam variables (2.3) are given by:

$$s = m_1^2 + m_2^2 + 2[E_1 E_2 + q_{12}^2(s)], \tag{2.5a}$$
$$t = m_1^2 + m_3^2 + 2[E_1 E_3 - q_{12}(s) q_{34}(s) \cos\theta_s], \tag{2.5b}$$
$$u = m_1^2 + m_4^2 + 2[E_1 E_4 + q_{12}(s) q_{34}(s) \cos\theta_s], \tag{2.5c}$$

where θ_s is the scattering angle as shown in figure F.2.1. We can solve the previous equations to obtain the energy:

$$E_1 = \frac{1}{2\sqrt{s}}\left[s + m_1^2 - m_2^2\right], \qquad E_2 = \frac{1}{2\sqrt{s}}\left[s + m_2^2 - m_1^2\right], \tag{2.6a}$$
$$E_3 = \frac{1}{2\sqrt{s}}\left[s + m_3^2 - m_4^2\right], \qquad E_4 = \frac{1}{2\sqrt{s}}\left[s + m_4^2 - m_3^2\right], \tag{2.6b}$$

and momentum of each particle:

$$q_{ij}^2(s) = \frac{[s-(m_i+m_j)^2][s-(m_i-m_j)^2]}{4s} = \frac{\lambda(s,m_i^2,m_j^2)}{4s}, \tag{2.7}$$

where:

$$\lambda(x,y,z) = x^2+y^2+z^2-2xy-2yz-2xz, \tag{2.8}$$

is called the Källén or triangular function, since $1/4\sqrt{-\lambda(x,y,z)}$ represents the area of a triangle with sides $\sqrt{x}$, $\sqrt{y}$ and $\sqrt{z}$ [34]. Inserting equations (2.6) and (2.7) into (2.5) we obtain for the t and u variables:

$$t = \frac{\sum m_i^2 - s}{2} - \frac{(m_1^2-m_2^2)(m_3^2-m_4^2)}{2s} + \frac{\lambda^{1/2}(s,m_1^2,m_2^2)\lambda^{1/2}(s,m_3^2,m_4^2)}{2s}\cos\theta_s, \tag{2.9a}$$

$$u = \frac{\sum m_i^2 - s}{2} + \frac{(m_1^2-m_2^2)(m_3^2-m_4^2)}{2s} - \frac{\lambda^{1/2}(s,m_1^2,m_2^2)\lambda^{1/2}(s,m_3^2,m_4^2)}{2s}\cos\theta_s. \tag{2.9b}$$

The scattering angle θ_s is given by:

$$\begin{aligned}\cos\theta_s \equiv z_s &= \frac{s^2+s(2t-\Sigma)+(m_1^2-m_2^2)(m_3^2-m_4^2)}{4s\ q_{12}(s)q_{34}(s)} \\ &= \frac{s^2+s(2t-\Sigma)+(m_1^2-m_2^2)(m_3^2-m_4^2)}{\lambda^{\frac{1}{2}}(s,m_1^2,m_2^2)\lambda^{\frac{1}{2}}(s,m_3^2,m_4^2)}.\end{aligned} \tag{2.10}$$

Besides the simplicity of the formulae, the three Mandelstam variables are introduced to make apparent the Lorentz invariance of the scattering amplitudes and exploit the concept of crossing symmetry. This symmetry is dynamically very important, but in terms of the kinematics it is almost trivial. We have treated the reaction $1+2 \to 3+4$ assuming that all energies are positive, but the four momentum conservation is an analytic relation [32] and one may then write the four-momentum conservation in the

following alternate forms:

$$p_1 + p_2 = p_3 + p_4, \tag{2.11a}$$
$$p_1 + (-p_3) = (-p_2) + p_4, \tag{2.11b}$$
$$p_1 + (-p_4) = p_3 + (-p_2), \tag{2.11c}$$
$$p_1 = (-p_2) + p_3 + p_4, \tag{2.11d}$$

where the last equation is physical only if the condition $m_1 > m_2 + m_3 + m_4$ holds.

Algebraically there is no objection to the form of equations (2.11), but a minus sign in the four momentum implies nonphysical values for the energy. However, from relativistic quantum mechanics and Quantum Field Theory (QFT) it is possible to give a meaning to this through *crossing symmetry*. We can identify the particle with four-momentum $-p$ as the corresponding antiparticle to the one with four-momentum p [2, 9]. So, crossing symmetry expresses the relation between particles and antiparticles. Crossing symmetry is actually built-in in the Standard Model and the associated Feynman rules [2, 35].

The expressions (2.11) may be interpreted as four-momentum conservation equations for the following reactions:

$$s-\text{channel} : 1 + 2 \to 3 + 4, \tag{2.12a}$$
$$t-\text{channel} : 1 + \bar{3} \to \bar{2} + 4, \tag{2.12b}$$
$$u-\text{channel} : 1 + \bar{4} \to 3 + \bar{2}, \tag{2.12c}$$
$$\text{decay} - \text{channel} : 1 \to 3 + 4 + \bar{2}, \tag{2.12d}$$

where $\bar{\alpha}$ stands for the antiparticle of α and the last expression is physical only if $m_1 > m_2 + m_3 + m_4$. The decay channel is usually referred as a $1 \to 3$ process. These reactions are shown in the figure F.2.2 and each one represents a different *reaction channel*.

The naming scheme for the channels in equations (2.12a), (2.12b) and (2.12c) refers to the variable which is positive in the given channel. The two remaining Mandelstam variables are the invariant momentum transfers [9]. The minimal value that each Mandelstam variable can attain is known as the *threshold* for this channel; for instance in the s channel, it is $s_0 = (m_1 + m_2)^2$. One can show [32] that the

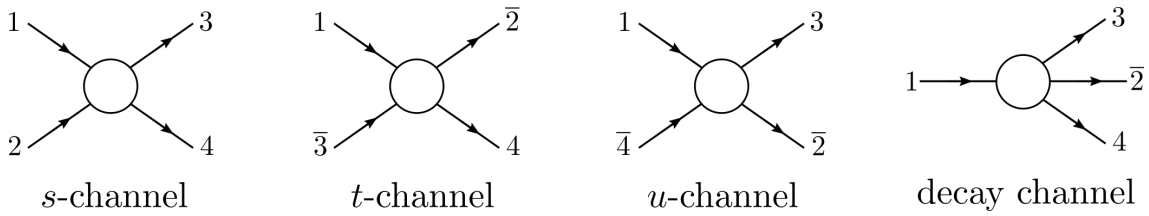

Figure F.2.2: Various channels for the reaction $1+2 \to 3+4$. The decay channel shown is physical if $m_1 > m_2 + m_3 + m_4$. The notation $\overline{\alpha}$ stands for the antiparticle of particle α.

physical region of the reaction $1+2 \to 3+4$ including the decay channel (if it is the case) is given by the Cayley determinant:

$$G(s,t,m_4^2,m_1^2,m_2^2,m_3^2) = -\frac{1}{2}\begin{vmatrix} 0 & 1 & 1 & 1 & 1 \\ 1 & 0 & m_2^2 & s & m_4^2 \\ 1 & m_2^2 & 0 & m_1^2 & t \\ 1 & s & m_1^2 & 0 & m_3^2 \\ 1 & m_4^2 & t & m_3^2 & 0 \end{vmatrix} \leq 0, \tag{2.13}$$

which by the symmetry properties of the determinant, we can write this equation as:

$$G(x,y,z,\alpha,\beta,\gamma) = G(y,x,\beta,\gamma,\alpha,z), \tag{2.14}$$

where s and t have been chosen as independent variables. The G function is also known as the tetrahedron function because it represents the squared volume of a tetrahedron with pairwise opposite sides $\sqrt{x}, \sqrt{y}; \sqrt{z}, \sqrt{\alpha}; \sqrt{\beta}, \sqrt{\gamma}$), scaled by a factor of -144.

It is convenient to use triangular coordinates s, t and u rather than the Cartesian s and t coordinates. The three lines of the coordinate system enter each other at an angle 60°, and s, t, u are the distances from the respective axes. Notice that if the height of the triangle formed by these lines is equal $\sum m_i^2$ then the condition $\sum m_i^2 = s + t + u$ is automatically satisfied. This graphical presentation is called the *Mandelstam plane*, and is presented schematically in fig. F.2.3 for the process $\omega + \pi^0 \to \pi^+ + \pi^-$.

Next we discuss the kinematics of the aforementioned decay channel, considering

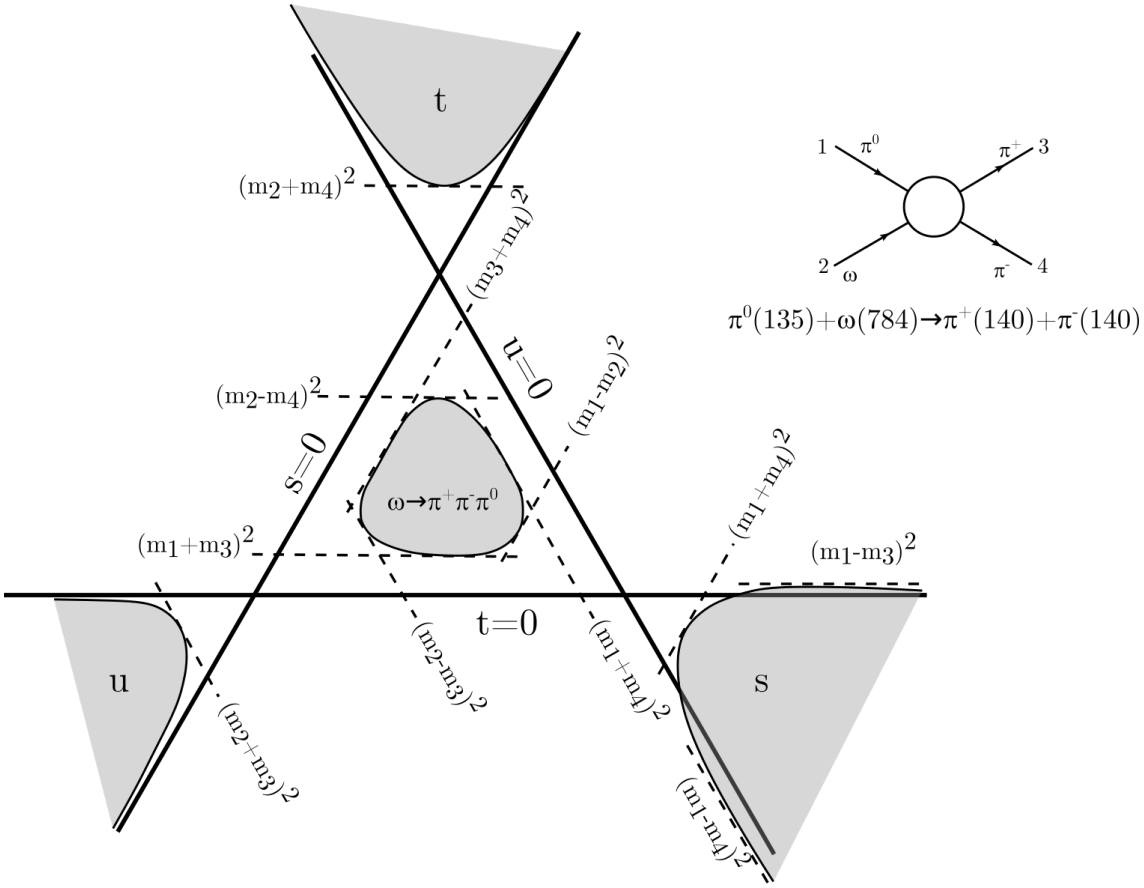

Figure F.2.3: Schematic representation of the physical regions of the $\omega+\pi^0 \to \pi^+ + \pi^-$ reaction in the Mandelstam plane. The central area corresponds to the decay channel, i.e. the $\omega \to \pi^+ + \pi^- + \pi^0$ process, which, in this case, is physical. Figure adapted from Fig. 4.7.7 from [32].

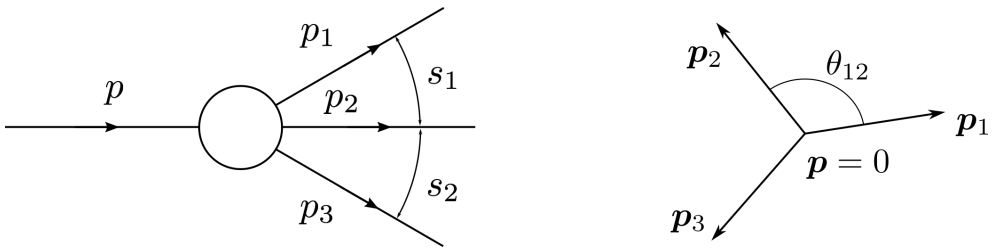

(a) (b)

Figure F.2.4: (a) Three particle decay process $p \to p_1+p_2+p_3$ with invariant variables s_1 and s_2. (b) Rest frame of the decaying system (where total momentum satisfies $\boldsymbol{p}=0$).

the general $0 \to 1+2+3$ reaction[1] for spinless particles as shown in figure F.2.4.

We have highlighted that this reaction is related by crossing to the scattering $0+\overline{1} \to 2+3$, this implies that the number of invariants that describes the reaction must be the same, say two. As invariant variables, for convenience we choose s, t and u as in the $2-2$ scattering processes. Given that in the decay channel, they are all positive we perform a standard name change, defining [32]:

$$s_{12} \equiv s_1 = (p_1+p_2) = (p-p_3)^2, \tag{2.15a}$$
$$s_{23} \equiv s_2 = (p_2+p_3) = (p-p_1)^2, \tag{2.15b}$$
$$s_{31} \equiv s_3 = (p_3+p_1) = (p-p_2)^2, \tag{2.15c}$$

as invariant variables. They satisfy:

$$s_1+s_2+s_3 = s+m_1^2+m_2^2+m_3^2. \tag{2.16}$$

Furthermore, each s_{ij} defines the invariant mass associated with the given ij two-body decay sub-channel.

To obtain the energies and momenta in the decay channel we expand the expression

[1] We rename the particles involved from $\{1,2,3,4\}$ to $\{0,1,2,3\}$ to match the standard notation employed in hadron spectroscopy.

(2.15) in the reference frame $p = (\sqrt{s}, 0)$ to obtain:

$$E_1 = \frac{s - s_2 + m_1^2}{2\sqrt{2}}, \qquad q_1 = \frac{\lambda^{1/2}(s, m_1^2, s_2)}{2\sqrt{s}}, \tag{2.17a}$$

$$E_2 = \frac{s - s_3 + m_2^2}{2\sqrt{2}}, \qquad q_2 = \frac{\lambda^{1/2}(s, m_2^2, s_3)}{2\sqrt{s}}, \tag{2.17b}$$

$$E_3 = \frac{s - s_1 + m_3^2}{2\sqrt{2}}, \qquad q_3 = \frac{\lambda^{1/2}(s, m_3^2, s_1)}{2\sqrt{s}}, \tag{2.17c}$$

the procedure applied here involves obtaining E_1, by considering the two particle decay $p \to p_1 + (p_2 + p_3)$ where the final state masses are m_1 and $\sqrt{s_2}$. The angular relations between momentum vectors follow from the definitions (2.15) by expanding the squares and using the definitions in equations (2.17). For instance the angle θ_{12} between $\boldsymbol{p}_1$ and $\boldsymbol{p}_2$ shown in the figure F.2.4 is given by:

$$\cos\theta_{12} = \frac{(s + m_1^2 - s_2)(s + m_2^2 - s_3) + 2s(m_1^2 + m_2^2 - s_1)}{\lambda^{1/2}(s, m_1^2, s_2)\lambda^{1/2}(s, m_2^2, s_3)}. \tag{2.18}$$

The *Dalitz plot* represents the physical region of the decay process $0 \to 1+2+3$ in the (s_1, s_2) plane, or to any variables related to s_1 and s_2 by a linear transformation with constant Jacobian. This plot is a very useful tool to study the dynamics of three particle decays, because a non uniformity in the plot provides information about final-state interactions and the formation of resonances [8, 36].

The boundary of the Dalitz plot is derived from equation (2.13) and the symmetry properties of the G function (2.14), and is expressed as:

$$G(s_2, s_1, m_3^2, m_1^2, s, m_2^2) = G(s_1, s_2, s, m_2^2, m_1^2, m_3^2) = 0. \tag{2.19}$$

To provide a direct derivation of equation (2.19) and to determine the phase space density of the Dalitz plot, we consider the phase space integral [32]:

$$R(s) = \int \prod_{i=1}^{3} \frac{d^3 p_i}{2E_i} \delta^3(\boldsymbol{p} - \boldsymbol{p}_1 - \boldsymbol{p}_2 - \boldsymbol{p}_3)\delta(\sqrt{s} - E_1 - E_2 - E_3). \tag{2.20}$$

we perform the integration over $\boldsymbol{p}_2$ in the rest frame where the total momentum

satisfies $\boldsymbol{p} = 0$:

$$R(s) = \int \frac{d^3p_1 d^3p_3}{8E_1E_2E_3}\delta(\sqrt{s} - E_1 - E_2 - E_3) \tag{2.21}$$

using the fact that:

$$E_2^2 = |\boldsymbol{p}_1 + \boldsymbol{p}_3|^2 + m_2 = q_1^2 + q_3^2 + 2q_1q_3\cos\theta_{13} + m_2^2, \tag{2.22}$$

and writing the differentials using relative orientations:

$$d^3p_1\, d^3p_3 = q_1^2 q_3^2\, dq_1\, d\Omega_1\, dq_3\, d\Omega_3 \quad = q_1E_1q_3E_3\, dE_1\, d\Omega_1\, dE_3\, d\cos\theta_{13}\, d\phi_3 \tag{2.23}$$

here, the quantity $\Omega_3 = (\cos\theta_{13}, \phi_3)$ represents the orientation of $\boldsymbol{p}_3$ with respect to $\boldsymbol{p}_1$, while the quantity Ω_1 represents the orientation of $\boldsymbol{p}_1$ with respect to a chosen and arbitrary axis. This election can be made since in the decay channel under consideration there is no preferred direction in space (see the figure F.2.4), Ω_1 could be integrated over the full solid angle, yielding a factor of 4π, and the variable ϕ_3 to give another factor equivalent to 2π. The energy delta function can be applied to perform the integration over $\cos\theta_{13}$ using $dE_2/d\cos\theta_{13} = q_1q_3/E_2$ giving the result [32]:

$$\begin{aligned} R(s) &= 8\pi^2 \int \frac{q_1q_3E_1E_3\, dE_1\, dE_3}{8E_1E_2E_3(q_1q_3/E_2)}\,\Theta(1-\cos^2\theta_{13}) \\ &= \pi^2 \int dE_1\, dE_3\,\Theta(1-\cos^2\theta_{13}). \end{aligned} \tag{2.24}$$

where the Heaviside step function Θ, restricts the angle $\cos\theta_{13}$ to physical values. The limits $\cos\theta_{13} = \pm 1$ corresponds to the boundary of the physical region in the (E_1, E_3) plane, i.e., the Dalitz plot. It is worth mentioning that E_1 and E_2 are linearly related to s_1 and s_2 through equation (2.17) with the corresponding Jacobian given by [32]:

$$\frac{\partial(E_1, E_2)}{\partial(s_1, s_2)} = \frac{1}{4s}. \tag{2.25}$$

Then, we can write:

$$R(s) = \frac{\pi^2}{4s}\int ds_1\, ds_2\,\Theta(1-\cos^2\theta_{13}). \tag{2.26}$$

To see the connection with equation (2.19), we introduce the condition of the

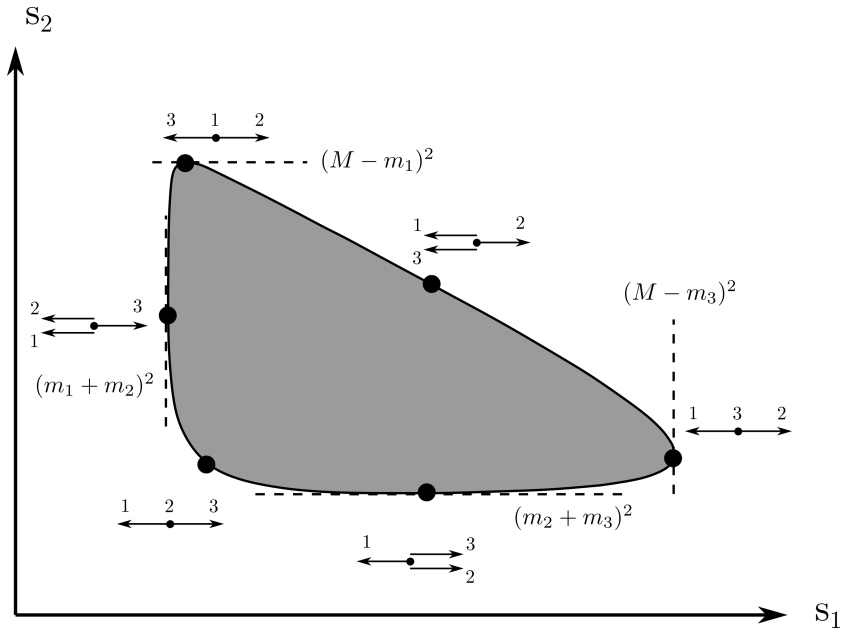

Figure F.2.5: Schematic representation of the physically allowed region for the decay channel $G(s_1, s_2, s, m_2^2, m_1^2, m_3^2) = 0$ in the (s_1, s_2) plane, also known as the Dalitz plot. The alignment of particle's three-momenta at the boundary (2.28) are also shown.

boundary, $\cos\theta_{13} = \pm 1$, into equation (2.22), obtaining:

$$\begin{aligned}(\sqrt{s} - E_1 - E_3)^2 &= q_1^2 + m_2^2 + q_3^2 \pm 2q_1q_3 = |q_1 \pm q_3|^2 + m_2^2 \\ &= E_1^2 + E_3^2 + m_2^2 - m_1^2 - m_3^2 \pm 2\sqrt{[(E_1^2 - m_1^2)(E_3^2 - m_3^2)]}, \quad (2.27)\end{aligned}$$

which implies that, at the boundary, $q_2 = q_1 \pm q_3$, and by cyclic permutations we also arrive to similar expressions for the other momenta $q_3 = q_2 \pm q_1$ and $q_1 = q_3 \pm q_2$. These conditions can be expressed in a concise and symmetric form by recognizing that at the boundary of the physical region it is satisfied:

$$\lambda(q_1^2, q_2^2, q_3^2) = 0, \quad (2.28)$$

which combined with the geometrical interpretation of the Källén function (2.8) implies that the vectors q_1, q_2 and q_3 are collinear [32]. Equation (2.27) can be written as:

$$4(E_1^2 - m_1^2)(E_3^2 - m_3^2) = [2E_1E_3 - 2\sqrt{s}(E_1 + E_3) + s + m_1^2 - m_2^2 + m_3^2]^2, \quad (2.29)$$

which, combined with equation (2.17) allow us to write:

$$R(s) = \frac{\pi^2}{4s} \int ds_1\, ds_2\, \Theta(-G(s_1, s_2, s, m_2^2, m_1^2, m_3^2)). \tag{2.30}$$

This integral is nonzero when the argument inside the Heaviside Θ function is equal to zero, i.e., when equation (2.19) is fulfilled. The physically allowed region of the decay channel is shown schematically in figure F.2.5, alongside with the condition (2.28) which relates to the alignment of the three momenta of the involved particles. From equation (2.26) we can derive the *phase space distribution*:

$$\frac{d^2R}{ds_1\, ds_2} = \frac{\pi^2}{4s}, \tag{2.31}$$

is constant within this region at fixed s.

The Dalitz plot is a very useful tool for studying particle decays. When data of a three-particle decay are plotted as points on the Dalitz plot, the density of these points is proportional to the matrix element squared. This is why resonances and structures related to the dynamics of the decay are apparent in this plot at a glance [34], as long as a sufficiently large number of events is collected.

In the context of this thesis work, the Dalitz plot played an important role in analyzing the decaying reaction $\Lambda_b^0 \to J/\psi p K^-$ in [19], particularly in identifying the $P_c(4312)^+$ signal and other P_c-like structures. The construction of the Dalitz plot in this case involved a detailed and complex experimental data analysis process, which included the use of experimental filters (cuts) to isolate relevant events and reduce background noise effectively as we will discuss briefly in section 3.2.

2.2 S-matrix theory

The S matrix is defined as the quantum operator that relates the incoming and outgoing states in the Fock spaces of a scattering process as depicted in figure F.2.6. It is defined such that its matrix elements quantify the transition from an initial $|i\rangle$ to a final $|f\rangle$ state [37, 38]:

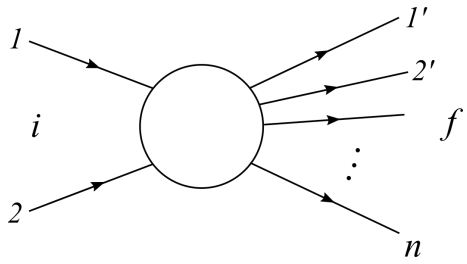

Figure F.2.6: General scattering process between two particles in the initial state $|i\rangle$, and n in the final state $|f\rangle$. Figure adapted from Fig. 1.1 in [38].

$$S = I + i(2\pi)^4 \delta^{(4)} \left(\sum_{j \in b} k_j - \sum_{i \in a} p_i \right) T, \tag{2.32}$$

thus defining the Lorentz invariant T-matrix. I is the identity operator which represents an absence of interaction, the four-dimensional Dirac delta function $\delta^{(4)}$ is introduced to explicitly take into account the energy-momentum conservation, and p_i and k_j are the four momenta of the incoming and outgoing particles, respectively.

In terms of its matrix elements $S_{ba} = \langle b| S |a\rangle$, we can write (2.32) as:

$$S_{ba} = \delta_{ba} + i(2\pi)^4 \delta^{(4)}(p_b - p_a) T_{ba}, \tag{2.33}$$

where p_a and p_b are the four momenta of the incoming and outgoing particles.

A list of fundamental properties that the S matrix must satisfy is [37, 39]:

(a) The superposition principle of quantum mechanics;

(b) The requirements of special relativity;

(c) The conservation of probability;

(d) The short-range character of the forces;

(e) Causality and the existence of macroscopic time;

(f) Specific symmetries associated with the reaction. For instance, parity conservation in the case of strong interactions.

They are essentially based on the general physics principles, that any short-range interaction like the strong interaction must satisfy [40]. We note that these principles do not fix the dynamics of the processes [41].

Property (a) requires that if $|\psi_a\rangle$ and $|\psi_b\rangle$ are physical states then any linear combination $|\psi_c\rangle = \alpha\,|\psi_a\rangle + \beta\,|\psi_b\rangle$ with $\alpha, \beta \in \mathbb{C}$ is also a physical state. (b) is the Lorentz invariance of the scattering process as well as for the S-matrix. (c) implies the unitarity of the S matrix, which by using the equations (2.32) and (2.33) provides:

$$SS^{\dagger} = 1, \tag{2.34a}$$

$$T_{ab} - T_{ba}^{\dagger} = i(2\pi)^4 \sum_n \delta^{(4)}(p_b - p_a) T_{bn}^{\dagger} T_{na}. \tag{2.34b}$$

If the interaction respects time reversal symmetry, as the strong interaction does, we can write [41]:

$$2\Im[T_{ba}] = (2\pi)^4 \sum_n \delta^{(4)}(p_b - p_a) T_{nb}^{\dagger} T_{na}, \tag{2.35}$$

where $\Im[\ ]$ stands for the imaginary part, and the sum is over all states which are allowed by energy-momentum conservation and all the other relevant quantum numbers [42]. The function T_{ab} is called the *scattering amplitude*.

Property (d) means that the elements of the S matrix are evaluated for asymptotic states, $t = \pm\infty$; more precisely, the initial state is defined a long time before scattering (compared to the interaction time, for the strong interaction typically 10^{-24} s), and the final state is defined a long time after the interaction takes place [38]. In this way, such asymptotic states can be regarded as free-particle quantum states. Consequently, the S-matrix theory is convenient for the study of the strong interaction [37].

Condition (e) is one of the most important and stringent ones for the S matrix and for the scattering amplitude, because, it imposes strict mathematical restrictions to the scattering amplitude, even without a specific knowledge of the interaction potential [37, 43]. As we will discuss latter, the causality of physical processes is closely linked to the analyticity of the scattering amplitude [41, 44, 45].

Concerning the point (f), the symmetry principles impose specific constraints on

the S matrix. For instance, it is important to note that the amplitude exhibits a simple but very important symmetry: it remains unchanged when the two incoming particles are interchanged. This indicates that the amplitude is invariant under the simultaneous exchange of p_1 with p_2 and all the corresponding quantum numbers of particle 1 with those of particle 2. This property influences the mathematical structure of the amplitude and is connected to the concept of crossing symmetry [9].

2.3 Analytical properties of the scattering amplitude

In the previous section we have made use of crossing symmetry to establish some kinematical properties for the $2 \to 2$ scattering process, but its implications are beyond kinematical. Crossing symmetry, causality of the physical processes (i.e. the cause must precede effects in time), and the analytical structure of the scattering amplitude are closely intertwined concepts.

In fact there is very good agreement between the phenomenological predictions based on analytic properties of amplitudes, and the experimental results for the scattering of strongly interacting particles. Further support comes from the fact that the kind of analyticity we are going to discuss next is found in several "model" theories, which although they cannot fully describe the strong interaction phenomena might still be expected to share many features with the correct theory. Such "model" theories include scattering from a potential as described by the Schrödinger equation [46, 47], the perturbation series solution to the quantized field equations [39] and the so-called axiomatic [37] and L.S.Z. [2, 35] approaches to field theory.

2.3.1 Partial wave projection

Rotational invariance implies that the total angular momentum is conserved in every scattering process. As a result, the amplitudes can be represented as a sum of scalar functions characterized by well-defined angular momentum, commonly referred to as partial waves. In the discussion that follows, we focus on the single-channel,

spinless case, where both the initial and final states have zero spin.

One of the major characteristics of resonances is that they have a well-defined spin, which restricts them to appear in only one partial wave. The above emphasizes the importance of partial-wave analysis for both the discovery of resonances and determination of their parameters. It should be remembered that the scattering amplitude is expressed in terms of two scalar functions. To be more concrete, in the s-channel representation the amplitude for spinless particles can be written as:

$$T^{fi}(s,t) = T^{fi}(s,t(s,z_s)) = \sum_{\ell=0}^{\infty} (2\ell+1)\, f_\ell^{fi}(s) P_\ell(z_s), \tag{2.36}$$

where f and i are the final and initial states, P_ℓ are the Legendre polynomials of the first kind, $f_\ell^{fi}(s)$ are the *partial wave amplitudes*, and $z_s \equiv \cos(\theta_s)$. The analysis can be generalized to arbitrary spin particles using Wigner d-functions.

The partial waves can be derived by applying the projection of the amplitude, as outlined in [41].

$$f_\ell^{fi}(s) = \frac{1}{2}\int_{-1}^{1} d\cos\theta_s\, P_\ell(z_s)\, T^{fi}(s,t(s,z_s)). \tag{2.37}$$

From the framework of partial waves $f_\ell^{fi}(s)$, an amplitude initially characterized by two variables (s and t or s and z_s) has been reformulated within an orthogonal basis of Legendre polynomials. Consequently, this transformation yields a resultant set of functions that depend exclusively on the parameter s.

The same procedure can be applied to other channels of physical interaction. As an example, in the t-channel, one has the corresponding projection:

$$g_\ell^{fi}(t) = \frac{1}{2}\int_{-1}^{1} dz_t\, T^{fi}(t,s(t,z_t))\, P_\ell(z_t), \tag{2.38}$$

For the t-channel case, it is standard practice to extract the angular momentum barrier as a separate factor $g_\ell(t) \propto [q_{12}(t)q_{34}(t)]^\ell$. The region of convergence of these partial-wave projections is called the Lehmann ellipse [9].

One of the significant advantages of performing the partial wave expansion is that, for small values of s, only a few partial waves are expected to dominate to the

amplitude calculation [38]. Another advantage is that each partial wave satisfies its own unitarity equation:

$$\Im[f_\ell^{fi}(s)] = \sum_n f_\ell^{fn}(s)\rho_n(s)f_\ell^{ni}(s), \tag{2.39}$$

where $\rho_n(s) = \frac{q(s)}{8\pi\sqrt{s}}$ is the phase space [41], $q(s)$ is given by (2.7) and n stands for the open intermediate channels that can appear. The amplitude is evaluated between the final $|f\rangle$ and initial $|i\rangle$ states. We will define a partial wave projected S-matrix as:

$$S_\ell^{fi} = 1 + 2i\rho(s)f_\ell^{fi}(s), \tag{2.40}$$

which fulfills:

$$S_\ell S_\ell{}^\dagger = I. \tag{2.41}$$

where I is the identity matrix. Since probability must be conserved, any given channel will have an absolute upper limit of one:

$$|S_\ell^{fi}(s)|^2 = \eta(s), \qquad \eta(s) \leq 1 \tag{2.42}$$

which to the case of elastic scattering ($f = i$ and no other channel opens), reads:

$$|S_\ell^{ii}(s)|^2 = 1. \tag{2.43}$$

Following equation (2.42) we can always write down a partial wave as [37, 48]:

$$f_l(s) = \frac{\eta_l \exp[2i\delta_l] - 1}{2i\tau(s)}, \tag{2.44}$$

which, in the case of elastic scattering, simplifies to:

$$f_l(s) = \frac{\exp[2i\delta_l] - 1}{2i\rho(s)}. \tag{2.45}$$

The function $\delta_\ell(s)$, commonly known as the phase shift, exhibits analytic characteristics that enable the partial wave to be expressed at low momenta as:

$$\frac{2}{\sqrt{s}}\Re[f_\ell(s)] \sim q^{2\ell}(a_\ell + b_\ell q^2 + \cdots), \tag{2.46}$$

where the leading term, a_ℓ, represents the scattering length. The coefficients arising from this low-energy expansion are fundamental for the understanding of meson-meson interactions [7, 9].

The general case reads [49]:

$$\Im[f_\ell(s)] = f_\ell(s)\Sigma(s)f_\ell(s)^\dagger \tag{2.47}$$

where $f_\ell(s)$ represents the partial wave amplitude matrix and $\Sigma(s)$ is the phase space matrix, which is diagonal and is expressed as:

$$\begin{pmatrix} \rho_1 & 0 & \dots & 0 \\ 0 & \rho_2 & \dots & 0 \\ \vdots & \vdots & \ddots & \vdots \\ 0 & 0 & \dots & \rho_n \end{pmatrix}. \tag{2.48}$$

For any partial wave, the two channel case can be written as:

$$S_\ell = \begin{pmatrix} \eta_\ell e^{2i\delta_{\ell,1}} & i\sqrt{1-\eta_\ell^2}e^{i(\delta_{\ell,1}+\delta_{\ell,2})} \\ i\sqrt{1-\eta_\ell^2}e^{i(\delta_{\ell,1}+\delta_{\ell,2})} & \eta_\ell e^{2i\delta_{\ell,2}} \end{pmatrix}. \tag{2.49}$$

2.3.2 Analyticity

The Mandelstam hypothesis [50, 51] states that the processes in figure F.2.2 described in the s, t and u channels are determined by a single relativistic invariant amplitude which is an analytical function in the s, t and u variables, except for some singularities that we will discuss below [52]. This hypothesis is a consequence of the analyticity of the scattering amplitude and crossing symmetry, that allows to analytically continue the amplitude from one channel to a "crossed one", e.g. from the s-channel to the t-channel, through the unphysical region (unphysical kinematics) in the Mandelstam plane.

The scattering amplitude is not analytical everywhere as singularities can appear. These singularities are classified into two categories, those that come from the choice of a certain channel or representation, whose are called *kinematical singularities*

(encoded in the expressions (2.33), (2.35)), and those whose are independent of this choice [31, 53–57], whose are referred to as *dynamical singularities*. The principle of *maximal analyticity* asserts that, after removing all kinematical singularities, the only singularities that remain in the amplitude are poles and cuts [38].

The Mandelstam hypothesis is generally accepted and proved order by order for Feynman diagrams [9, 58], although, no general proof for arbitrary multi-particle scattering configurations is known [59, 60]. Nonetheless for the $2 \to 2$ scattering of spinless particles the analytical continuation of the s-channel amplitude

$$\langle b| T |a\rangle = \langle 3;4| T |1;2\rangle = T_{1+2\to 3+4}(s,t,u), \tag{2.50}$$

to the t and u channels can be done rigorously [61].

In general, for n particle thresholds there are n cuts in the real energy axis, each one starting at its corresponding threshold, and 2^n Riemann sheets; for the rest of this section let us consider only one cut, i.e. one threshold. These cuts are referred to as right hand cuts (RHC) as they run from the threshold to $+\infty$. Since the physical amplitude is the value of the analytical function along the real axis, it is necessary to specify how to evaluate the amplitude depending on how we approach to the real axis, i.e. if we approach from above or below the cut. The usual way, based on perturbation theory and the Feynman convention [34, 37, 41, 62], is to take the amplitude as the limit from the upper half plane. For instance, in the s channel, if we fix $t = t_0$, this is equivalent to:

$$T_{\text{Phys.}-s} = \lim_{\epsilon\to 0^+} T(s + i\epsilon, t_0, u), \tag{2.51}$$

and in the u channel, by crossing:

$$T_{\text{Phys.}-u} = \lim_{\epsilon\to 0^+} T(s, t_0, u + i\epsilon) = \lim_{\epsilon\to 0^+} T(s - i\epsilon, t_0, u). \tag{2.52}$$

With this choice, the first *Riemann sheet* is called the *physical sheet*, and the second sheet is called the *unphysical sheet*. If more thresholds are added, the first Riemann sheet is still called the physical one and the rest of sheets are called unphysical.

Using the Schwarz reflection principle [9, 63],[2] we can write:

$$T(s+i\epsilon,t_0)-T(s-i\epsilon,t_0)=T(s+i\epsilon,t_0)-T(s+i\epsilon,t_0)^*=2i\Im[T(s+i\epsilon,t_0)] \tag{2.54}$$

and

$$\lim_{\epsilon\to 0^+}[T(s+i\epsilon,t_0)-T(s-i\epsilon,t_0)]=2i\Im[T(s,t_0)], \tag{2.55}$$

which is known as the discontinuity across the cut. Similar expressions are found for the t and u channels. See for instance [9].

The amplitude also has left hand cuts (LHC) which run from a certain real energy to $-\infty$ along the real energy axis. As happens in the potential scattering [46, 47, 64], the LHC, in combination with crossing symmetry, is generated by *exchange forces*. LHC are difficult to treat and many times are not explicitly included in amplitude analysis because they lay far away from the region of interest and any impact in the amplitude can be faithfully modeled through a polynomial background contribution. More information on the LHC can be found, for example, in Refs. [9, 38, 41, 62, 65]

The remaining singularities that can appear are simple poles. These poles can appear onto the real axis in the first Riemann sheet below the first threshold and correspond to the bound states of the system. For example, in proton-neutron scattering the deuteron appears as a pole in the real axis 2.2 MeV below the threshold [66]. Complex poles cannot appear on the physical sheet [9]. Using the Fourier transform one can show that these poles on the first Riemann sheet outside the real axis represents tachyons that violate physical causality [41]. Complex poles can appear on unphysical sheets and they correspond to resonances or virtual states. The latter appear below the first threshold on the real axis of the second Riemann sheet. An example of virtual state pole that appears in the isospin 1 channel of nucleon-nucleon scattering. The real part of the pole can be related to the mass of

[2] This states that if ξ is a finite segment of the real axis and D a domain of the complex z-plane whose intersection with the real axis is ξ, then any function $f(z)$ which is analytic in D and with imaginary part equal to $\Im[f(z)]=0$ in ξ satisfies:

$$f(z^*)=f^*(z), \tag{2.53}$$

where z, z^* belongs to D. Such $f(z)$ function is called *real analytic function* in D.

the resonance and the imaginary part to the decay width.

2.3.3 Dispersion relations

The analyticity of the scattering amplitude can be exploited through *dispersion relations*. A *dispersion relation* is the terminology used for the *Hilbert transform* [44, 67, 68] which is an integral transform and it is based on the Cauchy integral theorem for complex functions. Dispersion relations establish a connection between the amplitude at a specific energy and the integrals of the amplitude. They are utilized as consistency tests for experimental data and as theoretical constraints.

First, we introduce the basic concepts for dispersion relations. Let $f(s')$ be a function of complex variable s' defined along the real axis and with discontinuities (cuts) in the real axis for $s' > s_0$ (RHC) and $s' < \tilde{s}_0$ (LHC) with $\tilde{s}_0 < s_0$. Moreover suppose that $f(s')$ has a pole in M^2 in the real axis such that $\tilde{s}_0 < M^2 < s_0$, and $f(s')$ tends to zero as $|s| \to \infty$. We can define the contour C shown in figure F.2.7(a) and take $r^2 \to \infty$. Then the function $f(s)$ can be reconstructed in the complex plane using:

$$\begin{aligned} f(s) &= \frac{g}{M^2 - s} \\ &+ \frac{1}{2i\pi}\left[\int_{s_0}^{\infty} \frac{f(s'+i\epsilon) - f(s'-i\epsilon)}{s'-s} ds' + \int_{-\infty}^{\tilde{s}_0} \frac{f(s'+i\epsilon) - f(s'-i\epsilon)}{s'-s} ds'\right] \\ &= \frac{g}{M^2 - s} + \frac{1}{\pi}\int_{s_0}^{\infty} \frac{\Im[f(s')]}{s'-s} ds' + \frac{1}{\pi}\int_{-\infty}^{\tilde{s}_0} \frac{\Im[f(s')]}{s'-s} ds', \end{aligned} \tag{2.56}$$

where g represents the residue of the pole in M^2, the analysis employs the Schwarz reflection principle and adheres to the $+i\epsilon$ convention. We note that the orientation of the integration contour of the pole is opposite to that of the cuts. Equation (2.56) is know as the *dispersion relation* for $f(s)$ with zero subtractions [43, 44, 69]. As proven by a theorem due to Sugawara and Kanazawa [70], the dispersion relation expressed in (2.56) holds for any function $f(s)$ which is bounded by a finite power of $|s|$ as $|s| \to \infty$, provided that $f(s)$ vanishes as s tends to infinity along the cut. Under these conditions, the integral over the arc vanishes, and the integral along the

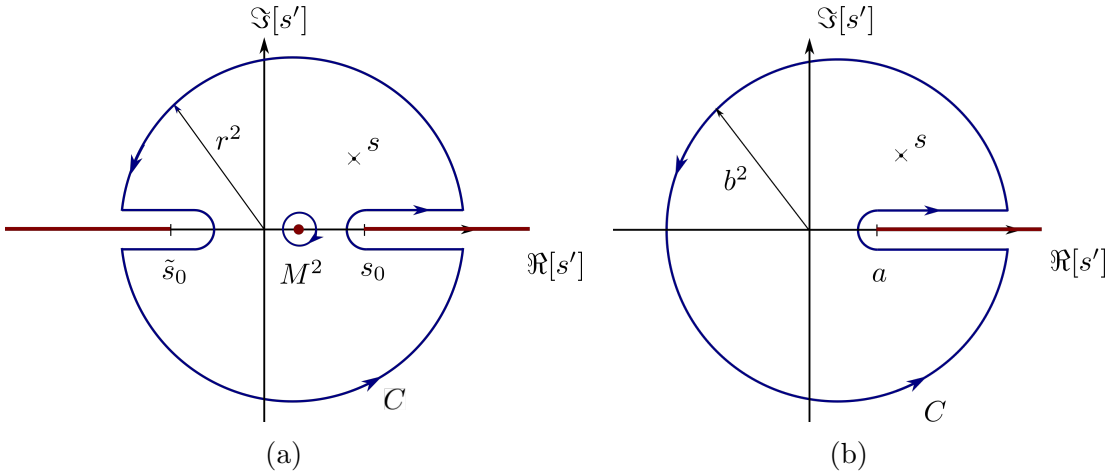

Figure F.2.7: (a) Integration contour for (2.56) where it is considered a left hand cut from $\tilde{s}_0$, a right hand cut from s_0 (both in red), and a pole onto the real axis in M^2. (b) Integration contour for (2.58) in the complex s'-plane, the red line represents a cut for the function.

cut converges.

If these conditions are not met and, for instance, the function $f(s)$ approaches a constant as $|s|$ tends to infinity, it becomes necessary to *subtract* the dispersion relation. This can be achieved by making use of the identity:

$$\frac{1}{s'-s} = \frac{1}{s'-s_\alpha} + \frac{s-s_\alpha}{(s'-s_\alpha)(s'-s)}, \tag{2.57}$$

and employ it in the Cauchy integral for the contour shown in F.2.7(b):

$$f(s) = \frac{1}{2i\pi}\oint_C \frac{f(s')}{s'-s}ds'. \tag{2.58}$$

We find:

$$f(s) = \frac{1}{2i\pi}\oint_c \frac{f(s')}{s'-s_\alpha}ds' + \frac{s-s_\alpha}{2i\pi}\oint_c \frac{f(s')}{(s'-s_\alpha)(s'-s)}ds'. \tag{2.59}$$

The first term is the value of the function at the *subtraction point* s_α, and is referred as the *subtraction constant*. The subtraction point s_α can be chosen arbitrarily, subject only to $s_\alpha < a$. By making this subtraction, the second term in (2.59) decays sufficiently rapidly, that the integral over the arc tends to zero. Hence

the *one-subtracted dispersion relation* takes the form:

$$f(s) = f(s_\alpha) + \frac{s - s_\alpha}{\pi} \int_a^\infty \frac{\Im[f(s')]}{(s' - s_\alpha)(s' - s - i\epsilon)}, \tag{2.60}$$

where we have explicitly used the $+i\epsilon$ physical convention.

In general, when $f(s)$ exhibits asymptotic growth characterized by a power N of s, the condition below must be satisfied:

$$\lim_{|s|\to\infty} \left| \frac{f(s)}{s^N} \right| \to 0, \tag{2.61}$$

it is necessary to introduce $N + 1$ subtractions to construct a converging dispersion relation. For each of these subtractions, it is possible to select a distinct subtraction point [37, 43, 44, 71, 72].

In principle, one can calculate dispersion relations with an arbitrary number of subtractions. However, two subtractions are enough to ensure convergence due to the Froissart [44, 73, 74] bound, i.e. $\sigma_{tot}(s) < c \log^2(s)$ with c an arbitrary constant and σ_{tot} the total cross section. Nevertheless, more subtractions than strictly needed can be made in order to weigh some regions of the integrand more than others or to effectively incorporate dynamics not considered explicitly in the model for $f(s)$.

The strongest and formal support for the relation between causality and the analyticity of the scattering amplitude via the single variable dispersion relations is on the Titchmarsh theorem [75, Chapter 2, pp. 119-128], for the purposes of this work it can be stated as [76–78]:

Let $f(s)$ a squared integrable function onto the real axis s which satisfies one of the following properties [37]

1. Its Fourier transform $F(t) = \mathscr{F}[f(s)]$ is causal, say, $F(t) = 0$ for $t < 0$.

2. When replacing s by $z \equiv x + iy$, the function $f(z)$ is analytic in the upper half plane ($y > 0$) and goes to $f(x)$ in at least a segment of the real axis when $y \to 0^+$. Moreover, the integral $\int_{-\infty}^{\infty} |f(x + iy)|dx < k$, for real k and $y > 0$, is bounded.

3. The real and imaginary part of $F(z)$ are the Hilbert transform of each other. In

other words, satisfies dispersion relations.

automatically has the other two properties. Note that when we introduce subtractions the condition on square integrability is relaxed [34, 42, 79].

It is important to highlight that the number and position of the poles for the amplitude are not fixed in general, and must be determined with strict attach to experimental data. This is mainly due to the *CDD poles* (Castillejo-Dalitz-Dyson poles) [80] that allows an infinite number of poles in the unphysical Riemann sheets. In this way, amplitude analysis requires detailed experimental studies to determine how many poles contribute to the observables.

2.4 Near-threshold amplitudes

The opening of a threshold impacts the shape of the observables as it usually generates a cusp in the S wave [81, 82]. More elaborated structures can appear in any partial wave as a consequence of the interplay between the particles in the newly opened threshold. The simplest example is the nucleon-nucleon scattering, where the deuteron is formed as a consequence of the nucleon-nucleon interaction.

In the near threshold energy region we can approximate the phase space to the absolute value of the outgoing four momentum $q(s)$ in the CM system, i.e. $\rho(s) \simeq q(s)$. Hence, for a single channel, unitarity dictates the S wave amplitude to fulfill $\Im\left[\frac{1}{T(s)}\right] = -q$ [83]. The effective range expansion for a single channel reads:

$$\frac{1}{T(s)} = -\frac{1}{a_0} + \frac{1}{2} r_e \, q^2(s) - iq(s) + \mathcal{O}\left(\frac{q^4(s)}{\Lambda^4}\right), \tag{2.62}$$

where Λ is some hard scale of the order of the force range. The parameter a_0 is the scattering length, and r_e is the effective range. The sign of a_0 depends on convention and is important due to its physical meaning. Namely, if a_0 is positive, there is a pole on the real axis of the first Riemann sheet, which is interpreted as the presence of a bound state. This situation arises, for example, for the case of the deuteron, corresponding to nucleon-nucleon scattering with isospin zero (see Figure F.2.8(a)).

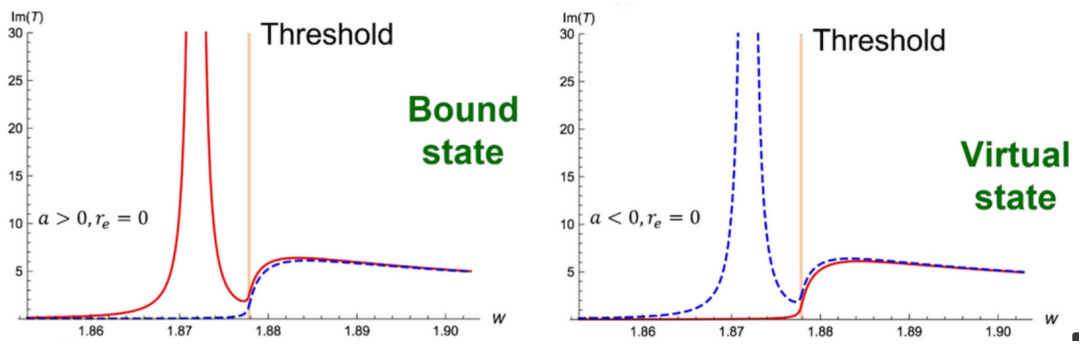

(a) (b)

Figure F.2.8: The amplitude on the real axis for a pole residue $r_e = 0$. When $a_0 > 0$, a bound state is generated, and when $a_0 < 0$, a virtual state is produced. The imaginary part of the amplitude along the real axis above the cut on the first Riemann sheet is shown in red with a solid line, while the amplitude along the real axis below the cut on the second Riemann sheet is shown as a dashed blue line. The vertical orange line highlights the threshold. The appearance of the bound and virtual states below the threshold is apparent.

The physical interpretation is that the interaction between nucleons is sufficiently strong to bind them into a stable system, often referred to as a hadronic molecule.

In contrast, if a_0 is negative, the pole moves to the real axis in the second Riemann sheet, which corresponds to a virtual state. This type of phenomenon occurs for example in nucleon-nucleon scattering with isospin one and is caused by an attractive interaction, which, though too weak to create a bound state, is strong enough to generate a pole and produce a detectable signal. This case is depicted in Figure F.2.8(b). In the literature, such a state is commonly referred as a virtual molecule.

We note that the sign convention for a_0 is not universal and other authors like Dong, Guo and Zou [84] prefer a + sign in front of the $1/a_0$ factor in equation (2.62), flipping the sign interpretation provided in the previous paragraph.

Weinberg's 1965 paper [85], was pivotal in dispelling the idea of the deuteron as an elementary particle. Weinberg demonstrated that the deuteron could be understood as a bound state of two particles (proton and neutron) through its scattering length and pole behavior. His analysis showed that if the deuteron were elementary, its properties would differ from those observed experimentally. The pole associated with the deuteron is on the real axis of the first Riemann Sheet, consistent with a bound

state and the scattering length is positive, so, by the Weinberg criterion, the deuteron is a stable bound and composite system. Additionally, there is an associated virtual state just below the threshold in the neutron proton channel which reinforces the composite nature or the deuteron. Thus, Weinberg's work solidified the understanding of the deuteron as a composite system rather than an elementary particle. In the context of the Weinberg criterion, the scattering length remains a crucial tool for distinguishing between bound and virtual states, it is a powerful tool, but it has some limitations in complex multi-channel systems, with significant relativistic effects as well as the ones with strong coupling to multiple thresholds.

Before extending the formalism to the coupled-channels case, we examine another kind of singularity that can appear in the $1 \to 3$ decay when a new channel opens: the triangle singularity as shown in figure F.2.9.

The triangle singularity happens in a $0 \to 1+2+3$ decay when it is kinematically possible for the three intermediate particles, X, Y and Z as shown in figure F.2.9, to go on-shell. When this is kinematically allowed, the LHC moves towards the RHC and coincide at the threshold, creating a singularity that can show up in the data as a spike at the $X-Y$ threshold. For the S wave case and scalar particles, it is straightforward to compute this singularity. The event distribution in energy for particles 1 and 2 reads:

$$\frac{dN}{d\sqrt{s}} = N_0\, \rho(s)\, |T(s)|^2, \tag{2.63}$$

where N is the measured number of events, $s \equiv s_{12}$, N_0 is the normalization, $\rho(s) = \lambda^{1/2}(s, m_0^2, m_3^2)\, \lambda^{1/2}(s, m_1^2, m_2^2)/\sqrt{s}$ is the phase space, and $T(s)$ is the scalar triangle

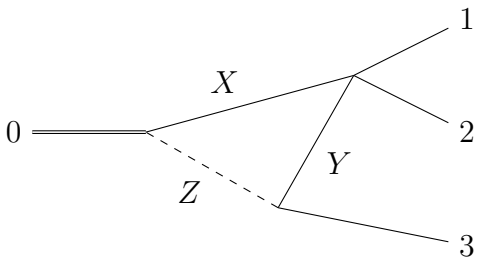

Figure F.2.9: Example of a triangle singularity diagram.

amplitude in figure F.2.9 given by [86]:

$$T(s) = \int_0^1 \frac{dx}{s(y_+ - y_-)} \left[\log \frac{(1 - x - y_+)}{-y_+} - \log \frac{(1 - x - y_-)}{-y_-} \right], \tag{2.64}$$

where

$$y_\pm = \frac{1}{2s} \left(-\beta \pm \sqrt{\beta^2 - 4\alpha s} \right), \tag{2.65a}$$

$$\alpha = x\, m_Z^2 + (1 - x)^2\, m_3^2, \tag{2.65b}$$

$$\beta = m_1^2 - (1 - x)\,(s + m_2^2) - x\, m_0^2. \tag{2.65c}$$

If the contribution from the triangle singularity can be neglected, it is possible to extend the single-channel effective range formalism to coupled-channels. Following (2.62), the two-channel amplitude in the region close to the higher threshold can be written [49, 83, 87]:

$$T_{ij}^{-1}(s) = \mu_{ij}(s) - i k_i\, \delta_{ij}, \tag{2.66}$$

with $i, j = 1, 2$ the two channels considered with 2 the higher-energy threshold. As we did for the single channel case in (2.62) we approximate the two-body phase space with the momentum, and, hence, k_i is the four momentum with respect to the i threshold. Consequently, the S matrix is:

$$S_{ij}(s) = \delta_{ij} + 2i \sqrt{k_i\, k_j}\, T_{ij}(s). \tag{2.67}$$

Due to the unitarity condition, the 2×2 real symmetric matrix $\mu_{ij}(s)$ represents the regular part (singularity free) of the inverse amplitude and can be parametrized as a matrix whose components can be Taylor expanded. At first order, it reads:

$$\mu_{ij}(s) = M_{ij} - c_{ij} s, . \tag{2.68}$$

At this point there are two choices that are made in the literature. The first one, based on [83] consists on approximating the momenta as $k_i \propto \sqrt{s - s_i}$ where s_i is the i threshold [49]. We call this approach the JPAC amplitude after the Joint Physics Analysis Center collaboration that uses such prescription [88]. With this choice, the amplitude is treated relativistically and due to the presence of square roots in k_1

and k_2, the scattering amplitude has branch cuts that originate at the two threshold energies, and, consequently, four Riemann sheets appear and causality is respected. The second option consists on performing a nonrelativistic expansion of the momenta as is done in Dong, Guo and Zou [84]. In this case only the branch cut due to k_2 is kept and k_1 becomes a constant in the region of interest close to the higher threshold. In this case, only two Riemann sheets are present, and the Schwarz reflection principle and causality are not respected. We name this choice as DGZ after the initials of the authors of Ref. [84]. Both approaches assume that other singularities, for example LHC or resonances not related to the opening of the threshold are far away so the $M_{ij}(s)$ is singularity free and its Taylor expansion converges. Additionally, JPAC and DGZ use opposite sign convention for the scattering length. Both JPAC and DGZ can be mathematically related what allows to compare results obtained using either approach. In what follows we compare both approaches under the scattering length approximation, where the c_{ij} parameters defined in (2.68) are set to zero. The amplitude matrix has the form:

$$\begin{bmatrix} m_{11}\, m_{12} \to m_{11}\, m_{12} & m_{12}\, m_{12} \to m_{21}\, m_{22} \\ m_{21}\, m_{22} \to m_{12}\, m_{11} & m_{21}\, m_{22} \to m_{21}\, m_{22} \end{bmatrix}, \tag{2.69}$$

where the m_{ij} simultaneously stand for the particles involved and their respective masses. The momenta in equation (2.62) reads:

$$q = \begin{cases} \nu_2 k_2 & \text{(JPAC)}, \\ \sqrt{2\mu_2 E} & \text{(DGZ)}, \end{cases} \tag{2.70}$$

where:

$$\mu_2 = \frac{m_{21} m_{22}}{m_{21} + m_{22}}, \qquad \nu_2 = \frac{\sqrt{m_{21} m_{22}}}{m_{21} + m_{22}},$$
$$E = \sqrt{s} - (m_{21} + m_{22}), \qquad k_2 = \sqrt{s - s_2} = \sqrt{s - (m_{21} + m_{22})^2}.$$

Both q definitions are equal, but we prefer to keep each group's notation. We start with the non-relativistic amplitude using near-threshold effective theory for two channels

[84]. The amplitude reads (omitting irrelevant global constant terms):

$$T(s) = \frac{1}{\det_{DGZ}} \begin{bmatrix} \frac{1}{a_{22}} + \sqrt{-2\mu_2 E - i\epsilon} & \frac{1}{a_{12}} \\ \frac{1}{a_{12}} & \frac{1}{a_{11}} - iq_1 \end{bmatrix}, \tag{2.71}$$

where:

$$\det_{DGZ} = \left[\frac{1}{a_{11}} - iq_1\right]\left[\frac{1}{a_{22}} + \sqrt{-2\mu_2 E - i\epsilon}\right] - \frac{1}{a_{12}^2}, \tag{2.72}$$

where q_1 is constant and is given by:

$$q_1 = \frac{1}{2\Sigma_2}\sqrt{\Delta\left(\Delta + 2m_{11}\right)\left(\Delta + 2m_{12}\right)\left(\Sigma_1 + \Sigma_2\right)} + \mathcal{O}(E), \tag{2.73}$$

and

$$q_1^{NR} = \frac{\lambda^{1/2}\left(s_2, m_{11}^2, m_{12}^2\right)}{2\sqrt{s_2}} = q_1, \tag{2.74}$$

with $\Sigma_1 = m_{11} + m_{12}$, $\Sigma_2 = m_{21} + m_{22}$, $\Delta = \Sigma_2 - \Sigma_1$, and $\mu_2 = m_{21}m_{22}/\left(m_{21} + m_{22}\right)$. The constants a_{11}, a_{12}, and a_{22} are the scattering lengths. Additionally, in DGZ, an effective $a_{22,eff}$ is defined so the denominator can be written:

$$\det_{DGZ} = \frac{1}{a_{22,eff}} - iq_2. \tag{2.75}$$

So:

$$\frac{1}{a_{22,eff}} = \frac{1}{a_{22}} - \frac{a_{11}}{a_{12}^2\left(1 + a_{11}^2 q_1^2\right)}\left[1 + ia_{11}q_1\right], \tag{2.76}$$

with

$$\Re\left[\frac{1}{a_{22,eff}}\right] = \frac{1}{a_{22}} - \frac{a_{11}}{a_{12}^2\left(1 + a_{11}^2 q_1^2\right)}, \tag{2.77}$$

$$\Im\left[\frac{1}{a_{22,eff}}\right] = -\frac{a_{11}^2 q_1}{a_{12}^2\left(1 + a_{11}^2 q_1^2\right)} \leq 0. \tag{2.78}$$

Given that under this approach q_1 is a constant, the pole is given by:

$$\frac{1}{a_{22,eff}} + \sqrt{-2\mu_2 E_p} = 0 \Rightarrow E_p = -\frac{1}{2\,\mu_2\,a_{22,eff}^2}, \tag{2.79}$$

so the mass and width of the resonance are given by:

$$M_p = \Sigma_2 - \Re\left[\frac{1}{2\,\mu_2\,a_{22,eff}^2}\right], \tag{2.80}$$

$$\Gamma_p = \Im\left[\frac{1}{\mu_2\,a_{22,eff}^2}\right]. \tag{2.81}$$

We can compute the pole position in the momentum space directly:

$$q_p = \eta\frac{i}{a_{22,eff}}, \tag{2.82}$$

with $\eta = +(-)$ if the pole is on the II(I) Riemann sheet.

For the JPAC approach, the amplitude matrix reads:

$$T(s) = \frac{1}{\det_{JPAC}}\begin{bmatrix} M_{22} - i\nu_2 k_2 & -M_{12} \\ -\tilde{M}_{12} & M_{11} - i\nu_1 k_1 \end{bmatrix}, \tag{2.83}$$

$\nu_i = \frac{\sqrt{m_{i1}m_{i2}}}{m_{i1}+m_{i2}}$ where $k_i = \sqrt{s - (m_{i1} + m_{i2})^2}$ and

$$\det_{JPAC} = [M_{11} - i\nu_1 k_1]\,[M_{22} - i\nu_2 k_2] - M_{12}^2. \tag{2.84}$$

The scattering lengths can be obtained from the M parameters:

$$a_{11} = \frac{1}{M_{11}}, \qquad a_{12} = \frac{1}{M_{12}}, \qquad a_{22} = \frac{1}{M_{22}},$$

and the effective $a_{22,eff}$ can be defined as in the DGZ approach [equation. (2.75)]

$$\det_{JPAC} = \frac{1}{a_{22,eff}} - i\nu_2 k_2, \tag{2.85}$$

where

$$\begin{aligned}\frac{1}{a_{22,eff}} &= M_{22} - \frac{M_{12}^2}{M_{11}^2 + \nu_1^2\, k_1^2}\left[M_{11} + i\nu_1\, k_1\right] \\ &= \frac{1}{a_{22}} - \frac{a_{11}}{a_{12}^2\left(1 + a_{11}^2\nu_1^2\, k_1^2\right)}\left[1 + ia_{11}\nu_1\, k_1\right].\end{aligned} \tag{2.86}$$

In this case, the poles are given by the algebraic equation

$$p_0 + p_1\, q + p_2\, q^2 + p_3\, q^3 + q^4 = 0, \tag{2.87}$$

with

$$p_0 = (s_1 - s_2)M_{22}^2 - (M_{12}^2 - M_{11}M_{22})^2, \tag{2.88}$$
$$p_1 = 2(s_1 - s_2)M_{22} + 2M_{11}(M_{12}^2 - M_{11}M_{22}), \tag{2.89}$$
$$p_2 = M_{22}^2 - M_{11}^2 + s_1 - s_2, \tag{2.90}$$
$$p_3 = 2M_{22}, \tag{2.91}$$

and $s_1 = (m_{11} + m_{12})^2$, $s_2 = (m_{21} + m_{22})^2$, and $s = s_2 - q^2$.

Under the scattering length approximation, the poles appear either on the real axis of the first or third Riemann sheets or as conjugate pairs either on the second or fourth Riemann sheets. The structure of the amplitude prohibits complex poles on the first Riemann sheet and, hence, causality is never violated regardless of the values of the M_{11}, M_{22}, or M_{12} parameters. The sheet where a pole belongs to is identified by the (η_1, η_2) pair:

$$\eta_1 = \operatorname{sign}\Re\left[\frac{M_{12}^2}{M_{22} + q} - M_{11}\right], \tag{2.92a}$$
$$\eta_2 = \operatorname{sign}\Re\left[q\right], \tag{2.92b}$$

which correspond to:

$$\text{I sheet: } (+,+), \qquad \text{II sheet: } (-,+),$$
$$\text{III sheet: } (-,-), \qquad \text{IV sheet: } (+,-).$$

2.5 Regge theory

Scattering amplitudes are not only analytical functions of the Mandelstam variables as we discussed in the previous section, Tullio Regge showed [89, 90] (and later Vladimir Gibov fully developed the theory [41, 91]) that it is possible to analytically continue the amplitude in the angular momentum variable. Angular momentum is an either integer or semi-integer physical variable, but as happens with the energy, its extension to complex values broadens our knowledge and allows a better description, and even a better prediction of different high-energy physics phenomena [9, 38, 41].

First of all, note that the scattering amplitude for the process $a+b \to c+d$ can be expressed using *partial wave expansions*, as discussed in the previous section. These expansions are valid only within the constraints of the Lehmann ellipse [9], which depends on the value of s in this case. To obtain a more general description that remains applicable even for large values of the Mandelstam variable s, it becomes necessary to perform an analytic continuation. At this point, extending the concept of partial waves to complex values of ℓ becomes crucial. This extension allows the new partial wave expansion to remain valid throughout the entire s-plane.

The analytical continuation of the function (2.36) to complex values of $l \to \ell$ is not an easy task. For the case of the Legendre functions the extension is natural expressing that in terms of the hypergeometric function (see [92]) but for the partial amplitude we have to use all the physical and most general restrictions to this purpose. These constraints include unitarity, crossing symmetry, analyticity, polynomial boundedness, threshold behavior, Regge behavior, causality (via dispersion relations), and the proper treatment of physical poles and resonances. Additionally, the amplitude must respect spin and symmetry properties and exhibit appropriate asymptotic behavior in ℓ to guarantee convergence, as we mention before in this chapter. Once these constraints are imposed, a model must be constructed based on the specific reaction or process under study and the energy range. One can made use of the *Sommerfeld–Watson* transform [43] to convert the

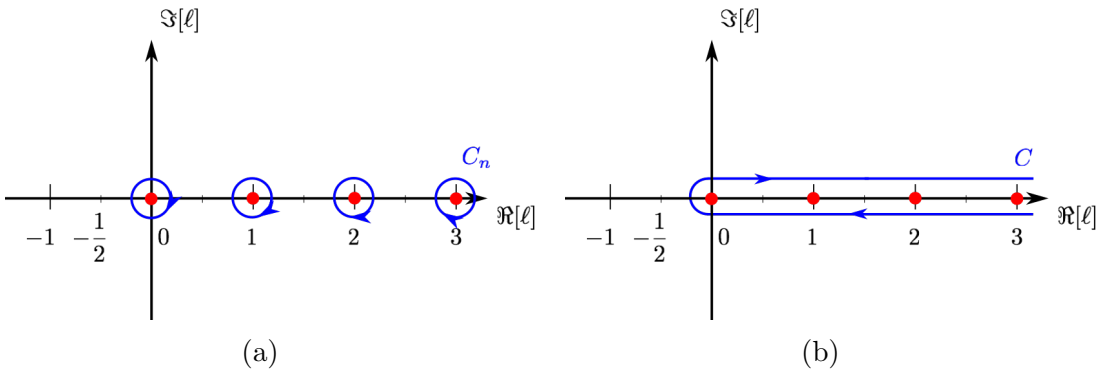

Figure F.2.10: (a) Set of contours that enclose all poles in the real axis of the complex angular momentum plane for the Sommerfeld–Watson transform. (b) Contour deformation into the curve C for the integration in (2.93). The value $\ell = -1/2$ is enhanced due to the behaviour of the Legendre functions (see [9, 92]). Figures inspired in Fig. II.8 from [93].

sum in (2.36) into an integral. Neglecting the spin of the particles this is written as:

$$T(s,t) = -\frac{1}{2i}\int_C \frac{(2\ell+1)f(\ell,s)P_\ell(-z_s)}{\sin\pi\ell}d\ell, \tag{2.93}$$

where $z_s \equiv \cos\theta_s$ is defined in (2.10), C is shown in F.2.10(b) and includes all positive integers and zero, and it is constructed avoiding all singularities from scattering amplitude $T(s,t)$.

The primary challenge with dispersion relations lies in reformulating all integrals in terms of the amplitudes in physical regions. For that, crossing symmetry is an essential tool. While its implementation is very straightforward for fixed-t amplitude dispersion relations, leading to closed and compact expressions, it becomes considerably more complex for partial-wave relations, since for each partial wave in a given channel they may involve the infinite series of partial waves in the crossed channel.

The definition for $f(\ell,s)$ is not unique for all the values of ℓ, but using the *Gribov–Froissart* transform [93] this can be solved with the introduction of two functions, $f^+(\ell,s)$ for even ℓ, and $f^-(\ell,s)$ for odd ℓ. These functions are called *partial amplitudes of definite signature*. In deriving this result one founds another kinematical factor which behaves as $\sim q^\ell$ near the threshold, and is related with the *angular momentum barriers* [22, 38, 41, 49].

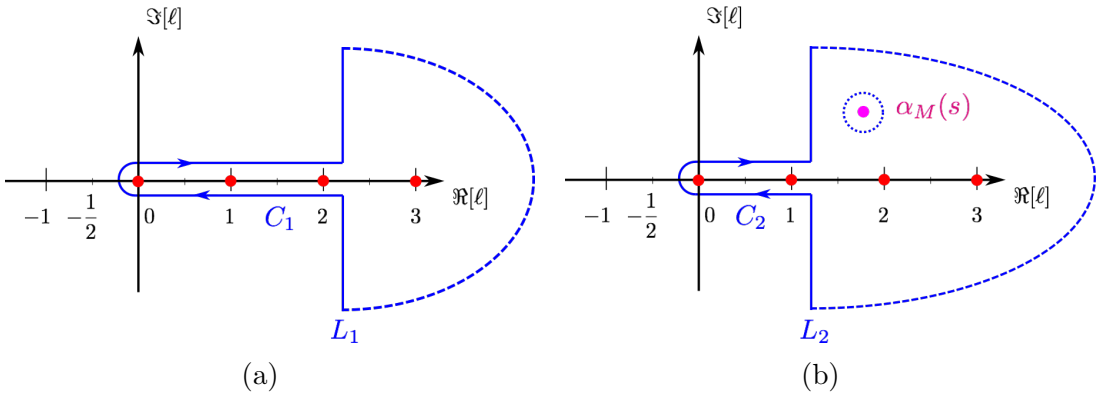

Figure F.2.11: Contour deformation for Sommerfeld–Watson transform (2.93). (a) Deformation with poles just in the real axis, (b) Deformation for the case with a pole in the complex ℓ-plane. For contour deformation in the case of complex Regge cuts can be found in [38]. Figures adapted from Figs. II.10 and II.11 from [93].

Now let us deform the original contour F.2.10(b) into the ones shown in F.2.11 which apart from a semicircle enclosed with a line at $\Re[\ell] = -1/2$ (which is a restriction that comes from Legendre functions properties [38, 46, 92]) it also includes the contours around the Regge poles appearing in the complex ℓ plane.[3]

We will denote the positions of these poles in $f^{\pm}(\ell, t)$ as $\alpha^{\pm}(s)$ while the residues will be denoted as $\beta^{\pm}(s)$. This function $\alpha^{\pm}(s)$ will be also called Regge trajectory, as the position of such poles describes a path parameterized by s in the ℓ plane.

The contribution from the semicircle of the contour L_2 is zero, due to the convergent behavior of the $f^{\pm}(\ell, s)$ partial waves. While the contributions coming from the Regge poles can be directly evaluated using their parameters, the result reads using the first $P_l(z)$ and second kind $Q_l(z)$ Legendre function relation [92]: $P_\alpha(-z) = e^{i\pi\alpha}P_\alpha(z) - \frac{2}{\pi}\sin\pi\alpha Q_\alpha(z)$:

$$T(s,t) = -\pi\left[2\alpha(s)+1\right]\beta(s)\left\{\left[1 \pm e^{-i\pi\alpha(s)}\right]\frac{\sin\pi\alpha(s)}{P_\alpha(-z_s)} \mp \frac{2}{\pi}Q_\alpha(-z_s)\right\}, \qquad (2.94)$$

where $[1 \pm e^{-i\pi\alpha(s)}]$ is known as the *signature factor*.

From this point, the analytical continuation in the angular momentum variable $\ell = l + J_p$, where J is the spin of the particle, allow the construction of an analytical

[3] Cuts contributions are also possible, see [38, 93] for more details.

function $\alpha(s)$, called *Regge trajectory*, which relates the poles of the amplitude in the angular momentum plane (*Regge poles* that matches the spin J_p of a resonance) [93, 94]. The contribution to the partial amplitude (near the pole) can be written as [38]:

$$f^{\pm}(\ell, s) \sim \frac{\beta(s)}{\alpha(s) - \ell}, \tag{2.95}$$

where $\beta(s)$ is also analytic and is known as the residue function, and $\alpha(s)$ has a right hand cut (RHC) above the elastic threshold. Mathematical form depends on the processes analysed.

The function presented in equation (2.95) can be directly compared to the Breit-Wigner amplitude in the vicinity of the pole at s_p, under the assumption of elastic two-body scattering [9]:

$$f_\ell(s) \propto \frac{g^2}{m^2 - s - i\, g^2 \rho(s, s_t)}, \tag{2.96}$$

where m is a real parameter, commonly referred to as the Breit-Wigner mass. The parameter g^2 governs the decay of the resonance and characterizes the coupling to open channels, while $\rho(s, s_t)$ denotes the phase space factor, with s_t representing the threshold energy. The calculation of $\rho(s, s_t)$ which exhibits analyticity along the real axis for $s \geq s_t$ offers a method for looking for the poles of $f(\ell, s)$. The above poles are situated in the lower half of the s-plane and are analytically connected into the physical region at $s + i\epsilon$. The form and position of a pole in the complex s-plane is influenced by two primary factors: the underlying dynamics of quantum chromodynamics (QCD) and the phase space properties. The phase space contribution, given by $\rho(s, s_t)$, manifests unitarity explicitly, while the effects of QCD dynamics are encoded implicitly in the parameters m and g. At the pole position s_p, equations (2.95) and (2.96) have to be equal, hence [95]:

$$\ell - \alpha(s_p) = \frac{m^2}{g^2} - \frac{s_p}{g^2} - i\rho(s_p, s_t) = 0\,. \tag{2.97}$$

This equation (2.97) is employed to establish a connection between the imaginary part of the Regge trajectory and the parameters describing resonance decay[95].

To clarify these concepts, refer to figure F.2.12. The partial amplitude, $f(\ell, s)$,

viewed as an analytical function of s, represents a resonance when $s = s_j$. This condition corresponds to the presence of a pole in the complex energy plane (the s-plane) on the second Riemann sheet. The same pole is present in the complex angular momentum plane, ℓ-plane, and corresponds to a pole onto the real in the position of the resonance spin $\ell = J_p$, say, this is a pole for the partial amplitude as an analytical function of s and ℓ, $f(\ell, s)$. The function $f(\ell, s)$ is analytical and it can take values outside the resonance poles, as the position of this point changes to unphysical values of energy, the corresponding point in the ℓ-plane also changes to unphysical values of ℓ (complex values). The analytical function generated by the motion in the ℓ-plane is the Regge trajectory and in the corresponding pole position matches the angular momentum of the resonances. In this way, from Regge theory perspective, the only difference between a bound state and a resonance is that the former occurs with s before threshold and the latter over the threshold, both with the corresponding ℓ value, so the same trajectory can for instance have a bound state with $\ell = 0$ and a resonance with $\ell = 2$, so Regge trajectories have states sharing the same quark composition but differing in their spin or excitation state [76, 96].

A notable characteristic of the hadron spectrum is the approximate linear behavior observed in its Regge trajectories. This property was first recognized by Chew and Frautschi [97], who introduced a plot—now known as the Chew-Frautschi plot—showing the spin of resonances, J_p, as a function of their squared mass, m^2. The patterns revealed in such plots have proven instrumental in guiding partial wave analyses. For example, gaps in these trajectories can suggest the existence of unobserved or missing states. Within the narrow-width approximation, this linear dependence is directly associated with the structure of a Regge trajectory [95]. The approximate linearity exhibited by these trajectories stands as one of the strongest phenomenological indicators of confinement in quantum chromodynamics (QCD) [4]. Consequently, hadronic states that align with these linear trajectories are often interpreted as being closely related to the predictions of quark models [98, 99].

Regge trajectories are significantly affected by resonance decays, which contribute to these trajectories by introducing imaginary components [91]. These contributions are governed by the principles of unitarity and analyticity and are closely linked to the widths of the resonances [91]. As a result, Regge trajectories serve as mappings from the complex energy plane, or s-plane, to the complex angular momentum plane,

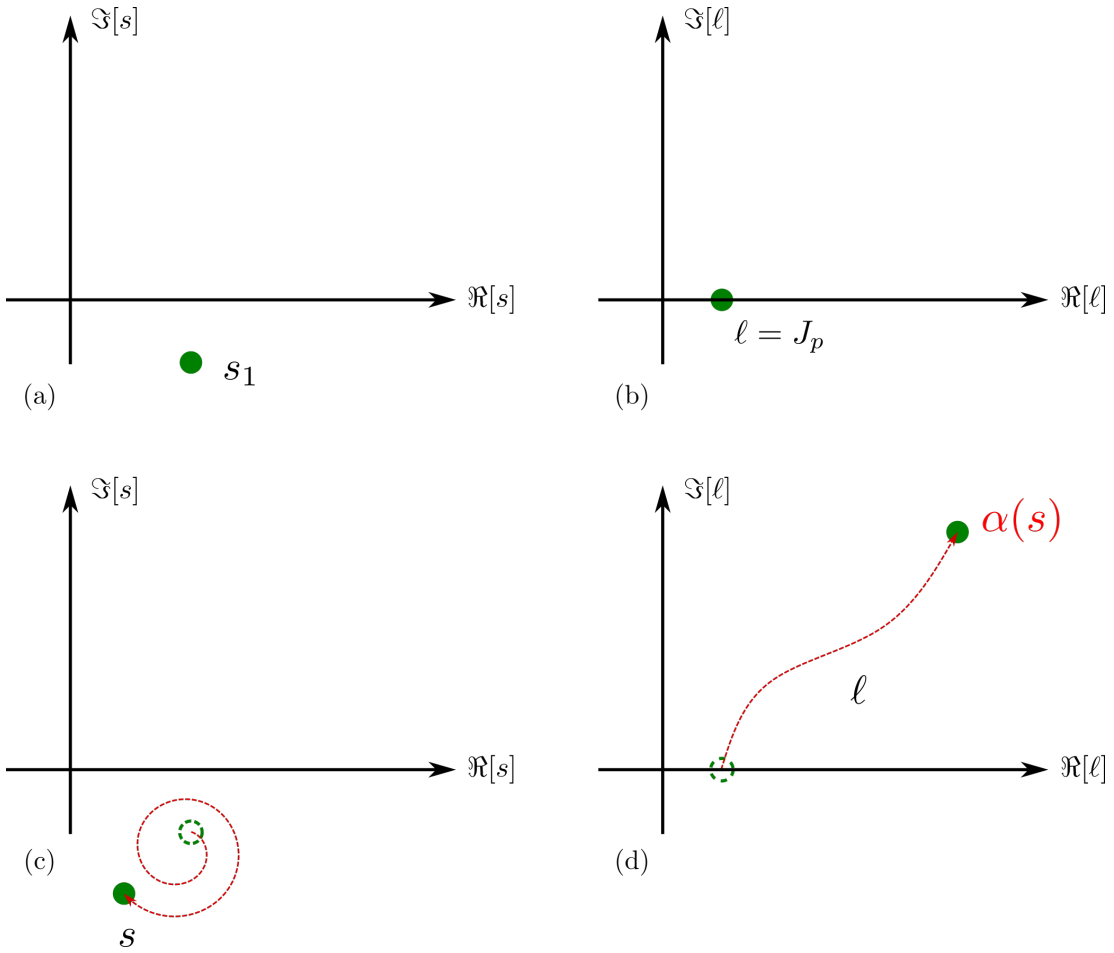

Figure F.2.12: Schematic comparison between the poles in the complex energy plane and in the complex angular momentum plane. (a) For $s = s_j$ there is a pole onto the s-plane for $f_\ell(s_j)$. (b) This pole has a real angular momentum and it represents a pole in $\ell = J_p$ for $f(\ell, s) = f(J_p, s_j)$. (c) The function $f(\ell, s)$ is analytic and can take values outside the resonance poles. (d) As the position in the s-plane changes it also changes in the ℓ-plane; the analytical function generated by this movement in the ℓ-plane is the Regge trajectory and matches the angular momentum of the resonances.

also known as the J-plane. In particular, a resonance is defined by its complex energy s_p and spin J_p, Regge trajectory $\alpha(s)$ is a complex valued function which satisfies the condition $\alpha(s_p) \equiv (\Re\left[J(s_p)\right], \Im\left[J(s_p)\right]) = (J_p, 0)$ [95].

Resonances are defined by their pole parameters, which are the prime object of study for the Regge trajectories. Up to now, Chew-Frautschi plots have been the almost exclusive tool for extracting information on Regge trajectories, with few exceptions [100, 101]. However, when the finite widths of resonances are taken into account, the Chew-Frautschi plot does not give a complete description of the Regge trajectory. To address this limitation, complementary analysis techniques can be employed. For example, two-dimensional plots of $\Im[s_p]$ versus $\Re[J] = J_p$ [102] can give more detailed information on the characteristics of the trajectory. In contrast, surface plots of $\Re[\alpha(s)]$ as a function of the complex energy s offer a more complete picture of the Regge trajectory [95]. These methods allow for a more complete characterization of the trajectory by considering the effects of finite resonance widths.

As we mentioned before symmetries play an important role in physics and its inclusion in the models offer a more robust framework to analyze for instance, Regge trajectories and scattering processes. An additional symmetry for the amplitudes of definite signature is known as the *MacDowell symmetry* [103]. As we mention at low energy Regge trajectories are approximately linear, MacDowell symmetry imposes that the *slope* parameter for Regge trajectories with the same isospin (I), but opposite naturality (η) and signature (τ) are the same, in other words the slope parameter for the trajectory $I^{\eta}_{(\tau)}$ is the same for $I^{-\eta}_{(-\tau)}$. The proof of this is beyond the interest of this work and you can see for instance [9, 38, 104] for a detailed explanation.

2.6 Data fitting and uncertainty analysis

The determination of the existence of each resonance and its physical properties relies on fitting experimental data accompanied by an uncertainty analysis. There are several techniques that can be used. Some are based on a frequentist point of view [105, 106] and others use a Bayesian perspective [107]. In this work we will take the frequentist approach and will rely on Monte Carlo methods. Monte Carlo methods

are a class of computational algorithms that utilize random sampling to approximate solutions to mathematical and physical problems, particularly those involving complex or high-dimensional systems. Generally, these methods are computationally expensive and are applied in situations where an exact analytical solution is not feasible to obtain. Among Monte Carlo methods, the bootstrap technique allows to compute uncertainties. It is a non-parametric resampling technique that operates directly on the experimental data with very few assumptions. In this thesis we will use this technique to perform the uncertainty analysis once the models have been fitted to the experimental data.

The conventional method for fitting data involves maximizing the likelihood function:

$$\mathcal{L}(\{\theta\}|\{y\}s) = \prod_{i}^{N} P_i(y_i|\theta_i), \tag{2.98}$$

where $P_i(y_i|\theta_i)$ represents the probability density function evaluated at a given parameter θ_i and y_i corresponds to the observed experimental data point. This function is multiplicative because it is constructed under the assumption that the observed data points are statistically independent. We will further assume that the data are also identically distributed, i.e. their uncertainties will follow the same distribution. The Likelihood function is constructed to measure the plausibility of a parameter θ given the observed data X. Its goal is to reverse the usual interpretation of probability, normally we use $P_i(y_i|\theta_i)$, the probability of data given the parameter, but, likelihood flips this perspective fixing the data and treating θ as the variable.

Likelihood is defined only up to a positive multiplier, which we have been taken to be one. It is an statistical tool to estimate the probability of certain data under an assumed model or hypothesis. It is used for parameter estimation and statistical hypothesis tests so that they can compare different models and choose the best-fitted model. Properties of likelihood include its dependence on the model parameters and data, and its use in constructing likelihood functions, which can be maximized to find the most probable parameters. In the discrete case the likelihood function (2.98) is the probability of observing our sample. In the continuous case, $\mathcal{L}(\{\theta\}|\{y\}s)\Delta$ is approximately the probability of our sample lying in a smart interval $[x, x + \Delta]$ [108]. The absolute value of the likelihood function does depend

on the sample size n. The larger the dataset, the smaller the likelihood; typically is due to the product structure involving probabilities or densities less than 1. But, it is the relative likelihood between different parameter values or models that carries inferential meaning. If a model estimates a number of parameters, the degrees of freedom associated with the likelihood are reduced by that very number. For example, in many model-fitting scenarios the likelihood leads to the χ^2 estimator, and the ratio $\chi^2/\text{dof} \sim 1$ is what evaluates the goodness-of-fit of the model [109]. The parameter that maximizes likelihood $\hat{\theta}$ corresponds to the value that makes the observed data most probable under the model; maximum Likelihood adheres to the principle of consistency, meaning that as the sample size increases $\hat{\theta}$ converges to the true parameter value under certain regularity conditions. If a Gaussian distribution is assumed for binned data, the corresponding probability density function is expressed as:

$$P_i(y_i|\theta_i) = \frac{1}{\sqrt{2\pi}\sigma_i} \exp\left[-\frac{1}{2}\left(\frac{f_i(\{\theta\}) - y_i}{\sigma_i}\right)^2\right], \tag{2.99}$$

where (y_i) is the value of the experimental data point for the i-th bin, and σ_i is its associated uncertainty. The function $f_i(\{\theta\})$ is the theoretical model or objective function to be fitted. This expression assumes statistical independence among bins, which is a standard assumption. Maximizing the likelihood function is mathematically equivalent to minimizing the χ^2 function:

$$\chi^2(\{\theta\}) = \sum_i^N \left(\frac{f_i(\{\theta\}) - y_i}{\sigma_i}\right)^2. \tag{2.100}$$

The choice of a Gaussian distribution is standard in many physical problems and is adequate if the experimental uncertainties are of statistical origin [21].

The minimization process is usually performed using gradient-based optimization algorithms, for example, MINUIT [110] or the Levenberg-Marquardt method [111, 112]. One must be aware that the occurrence of multiple local minima can trap the optimizer into a local minimum, resulting in convergence to an unphysical solution. One common way to deal with this problem is to attempt a variety of initial parameter values at the outset of optimization along with detailed analysis, from both statistical and physical perspectives, of the resulting minima. Another often powerful strategy

is to initially use some global method such as genetic algorithms [113, 114] and then follow through to the solution by a gradient-based approach. Understanding the shape of the likelihood profile and the proximity of any local minima is important to ensure a robust interpretation of the findings. Another critical aspect is the choice of a suitable set of starting parameters when using the bootstrap method, as discussed in the next section.

2.6.1 Uncertainties estimation with bootstrap

Physical studies go beyond proposing a model and fitting it to the experimental data. They require a comprehensive error analysis to take into account the experimental uncertainties and a robust methodology to propagate those uncertainties to the extraction of the physically meaningful quantities , e.g. masses and widths of the resonances, and to any prediction. A standard approach to perform this analysis is to use the covariance matrix, obtained from the Hessian of the likelihood function. A widely used tool in high-energy physics for optimization tasks is the MIGRAD routine included in the MINUIT package [110]. This calculation relies on the parabolic approximation of the likelihood function around the minimum, which always provides symmetric uncertainties for the fitted parameters. The main benefit with this procedure is that it is computationally cheap and, most of the time, is reliable enough. Another routine within the MINUIT package is MINOS, which is designed to sample the likelihood function in the vicinity of the minimum. It is more expensive computationally but provides better error estimates, in many cases asymmetric. However, it still presents the problem on how to propagate the errors obtained for the parameters to other observables. Especially if correlations among the parameters matter. This problem can be particularly dire for the case of pole extraction, as the error propagation from parameters and amplitudes to the pole extraction can be highly nontrivial. To avoid this limitation, approaches based on Monte Carlo simulations like the bootstrap [108, 115] or the jackknife, provide a robust, albeit computationally expensive, alternative. Bootstrap methods yield rigorous results that are free from the assumptions of likelihood symmetry or linearity in parameter space.

To establish a systematic understanding of resampling techniques for uncertainty estimation, it is worth studying the jackknife method before presenting the bootstrap technique that will be employed. The jackknife was originally designed as a method to estimate the bias and variance of statistical estimators [116]. The jackknife method consists on systematically recomputing the estimator while leaving out one observation at a time, which can give insight into the influence of individual data points on the properties of the estimator. The jackknife procedure works as follows. Let $Y = \{y_1, y_2, \cdots, y_n\}$ denote a dataset of n observations and let $F(Y)$ denote the interested quantity, e.g. mean or variance. The first step consists on creating n subsets by excluding one observation from the dataset, one at a time. These resulting subsets $Y(i) = \{y_1, \ldots, y_{i-1}, y_{i+1}, \ldots, y_n\}$ can now be used to compute the quantity of interest for each leave-one-out sample yielding $F_{(i)}$ for $i = 1, 2, \ldots, n$. Next, pseudo-values are calculated for each observation so that the contribution of this observation to the overall statistic may be assessed. The pseudo-value for the i-th observation is given by:

$$F_i^* = n\,F(X) - (n-1)\,F_{(i)}, \tag{2.101}$$

where $F(X)$ is the quantity of interest computed using the full dataset. These pseudo-values can be used to estimate the bias-corrected and the variance of the statistical estimator. The jackknife bias estimate is defined as the average difference between the leave-one-out estimator and the full estimator:

$$\text{Bias}(F) \equiv \frac{1}{n}\sum_{i=1}^{n}\big(F_{(i)} - F(Y)\big). \tag{2.102}$$

Similarly, the jackknife variance is estimated via variability in the leave-one-out estimator:

$$\text{Var}(F) \equiv \frac{n-1}{n}\sum_{i=1}^{n}\big(F_{(i)} - \overline{F}_{(i)}\big)^2, \tag{2.103}$$

where $\overline{F}_{(i)}$ is the mean of the leave-one-out estimates. Finally, the jackknife variance can be used to construct confidence intervals for the quantity of interest. For example, a confidence interval is given by $F(Y) \pm z_{1-\alpha/2}\sqrt{\text{Var}(F)}$ where $z_{1-\alpha/2}$ is the critical value from the standard normal distribution. The jackknife method is systematic and deterministic, which makes it efficient to compute. The method is especially helpful

for a small number of sample sizes or if the computational resources are limited.

The bootstrap method, developed by Efron [108] is an extension of the jackknife technique. The method is based on using random sampling with replacement in generating a number of resamples from the original dataset, thereby enabling the development of empirical distributions of the estimator that supports reliable estimation of bias, variance, and confidence intervals without dependence on linearity or normality assumptions [117].

There are two main ways to describe the bootstrap method [115]. The first, the "plug-in" approach, views the bootstrap in terms of a functional operation applied to the underlying population distribution function q. More specifically, if a functional $F(q)$ describes some property of the population that is desired, then the corresponding bootstrap estimate is obtained by substituting the population distribution function q with the empirical distribution function $\{q_n\}$ to obtain the expression $F(\{q_n\})$. This approach points out the empirical distribution as a way of estimating population characteristics.

The second perspective, which has significantly contributed to the widespread adoption of the bootstrap envisages a "bootstrap world". In this hypothetical world, the analyst possesses complete knowledge of the data-generating process and the statistical model that replaces all unknown parameters with their observed estimates. This "bootstrap world" replicates the sampling design of the real world as closely as possible. Even though real-world data allows only a single observation from the population, the bootstrap world allows for potentially an infinite number of bootstrap samples, or resamples, taken from the empirical surrogate population. Within this simulated framework, quantities of interest are approximated through computational methods. For instance, to estimate the variance of some complex parameter, one would generate N_B bootstrap samples, recalculate the parameter for every sample, and use the variance of the recalculated values as an approximation of the variance of the parameter. As N_B goes to infinity, the sample variance converges to the true variance within the bootstrap world. This limiting variance acts as an estimator for the actual variance of the parameter observed in the real world. The bootstrap framework therefore provides a systematic way of estimating the statistical properties of real-world situations using statistics computed in the bootstrap world, subject only by Monte Carlo error [109].

Suppose that we have a data set $Y = y_1, y_2, \ldots, y_n$, which is a collection of random variables with a joint distribution P_n and we wish to estimate a population parameter θ. Using this data, an estimator $\hat{\theta}_n$ (e.g., derived via maximum likelihood or method of moments) is constructed. One of the fundamental challenges in statistical inference is determining the accuracy of $\hat{\theta}_n$ often via measures like mean squared error (MSE) or confidence intervals. All these procedures are based on the sampling distribution of $\hat{\theta}_n$, which is usually unknown and, in most cases, analytically infeasible. The bootstrap method solves this problem by approximating the sampling distribution of $\hat{\theta}_n$ through resampling, thereby allowing its characteristics to be estimated.

The key idea underlying the bootstrap may be summarized as follows [117]. First, based on the given data $\mathbf{Y}_n = \{y_1, y_2, \ldots, y_n\}$, an empirical estimate $\hat{P}_n$ of the unknown joint distribution P_n is obtained. This is often represented as the empirical measure that assigns equal probability to each observed data point. From this empirical distribution, further random samples $\mathbf{Y}_n^* = \{y_1^*, y_2^*, \ldots, y_n^*\}$ are drawn by sampling with replacement, thus in effect "bootstrapping the data". If $\hat{P}_n$ is a "good" approximation to P_n and $\mathbf{Y}_n^*$ is obtained from $\hat{P}_n$, then the relation between data and its underlying true distribution is preserved in the bootstrap world as well. In order to estimate the distribution of $\hat{\theta}_n$, a bootstrap replica θ_n^* is created from the resampled data $y_1^*, \ldots, y_n^*$. Hence, the conditional distribution of θ_n^* given the observed data $\mathbf{Y}_n$ approximates the sampling distribution of $\hat{\theta}_n$. This approximation becomes the foundation for further inferential procedures.

One of the strengths of the bootstrap lies in its general applicability to functionals of $\hat{\theta}_n$, such as its variance or quantiles for this we employ the corresponding function to the conditional distribution of θ_n^*. More precisely, the bootstrap estimate of the variance of $\hat{\theta}_n$ is the conditional variance of θ_n^*. On the other hand, the bootstrap estimate of a quantile, namely the α-quantile, is the corresponding quantile of the conditional distribution of $\hat{\theta}_n^*$. By generating a large number of bootstrap replicates through repeated resampling, the method provides a numerical approximation to these and other distributional characteristics, enabling practical inference even in complex, high-dimensional contexts. While this idea sounds simple, the quality of this bootstrap depends on the quality of the empirical estimate $\hat{P}_n$ and the properties of $\hat{\theta}_n$. For the case of dependent data, more refined analyses use block bootstrap depending on dependence structure or sieve bootstrap [117].

Let $Y = y_1, y_2, \ldots, y_n$ be a collection of independent and identically distributed random variables with common distribution function F, and let $\hat{F}_n$ be an estimator of F based on that collection of variables, say:

$$F_n(y) = \frac{1}{n} \sum_{i=1}^{n} I(Y_i \leq y), \tag{2.104}$$

where $y \in \mathbb{R}$ and $I(\cdot)$ is the indicator function (a mathematical function used to represent a condition or event), note that in this case we are assigning equal weight to each observed data point, providing a straightforward and practical approximation of the underlying distribution F. Next let $\{y_1^*, y_2^*, \ldots, y_m^*\}$ random variables with common distribution $\hat{F}_n$, with m denoting the resample size being $m \leq n$. Then, $\hat{F}_n = F_n$ when the y_i^* are generated by simple random sampling with replacement from Y.[4] This process treats the empirical distribution $\hat{F}_n$ as if it were the true population distribution.

Suppose the parameter of interest is $\theta = \theta(F)$, such as the population mean or variance, and a statistic $T_n = t_n(y_1, y_2, \ldots, y_n; \theta)$ is used to estimate it based on the observed data. For instance, the normalized sample mean can be expressed as:

$$T_n = \sqrt{n} \frac{\overline{y}_n - \mu}{\sigma}, \tag{2.105}$$

where:

$$\overline{X} = \frac{1}{n} \sum_{i=1}^{n} y_i, \tag{2.106}$$

denotes the sample mean, and the quantities $\mu = \mathbb{E}[y_i]$ and $\sigma^2 = \mathrm{Var}(y_i)$ are the population mean and variance, respectively. To estimate the sampling distribution of T_n, the bootstrap calculates an analogous statistic $T_{m,n}^*$ based on the resampled data $\mathbf{y}_n^* = \{y_1^*, \ldots, y_m^*\}$. This statistic is defined as:

$$T_{m,n}^* = t_m(y_1^*, y_2^*, \ldots, y_m^*; \hat{\theta}_n), \tag{2.107}$$

where $\hat{\theta}_n$ is the plug-in estimate of θ, obtained by replacing the unknown distribution F with its empirical counterpart $\hat{F}_n$. For example the bootstrap version

[4] In some applications, a smoothed version of $\hat{F}_n$ may be preferred to refine the approximation or address specific requirements.

of the normalized sample mean takes the form:

$$T^*_{m,n} = \sqrt{m}\frac{\overline{y}^*_m - \hat{\mu}_n}{\hat{\sigma}_n}, \tag{2.108}$$

being $\overline{X}^*_m$ the mean of the bootstrap sample, and $\hat{\sigma}_n$ and $\hat{\mu}_n$ represents the sample variance and mean of $\hat{F}_n$. When $\hat{F}_n$ is the empirical distribution, both $\hat{\mu}_n$ and $\hat{\sigma}^2_n$ corresponds to the sample mean and variance of the observed data. By repeating this resampling process and recalculating $T^*_{m,n}$ multiple times the bootstrap approximates the probability distribution $\mathcal{P}(T_n)$ by the conditional distribution of $\mathcal{P}(T^*_{m,n}|y_1, y_2, \ldots, y_n)$.[5] In the case of a parameter $\xi(\mathcal{P}(T_n))$ based on some functional of this distribution, its bootstrap estimator is given by $\hat{\xi} = \xi(\mathcal{P}(T^*_{m,n}|y_1, y_2, \ldots, y_n))$.

It can be shown (see [118]) that the bootstrap approximation for independent and identically distributed random variables with finite variance is asymptotically consistent for quantities like the sample mean the convergence and inference based on the bootstrap approximation is similar or better than the normal approximation for standard discrete distributions such as the Geometric, Poisson or Binomial.

Model-based bootstrap generalizes the traditional bootstrap method to problems where data can no longer be assumed to consist of independent and identically distributed observations, incorporating structured models such as regression and time series in an effort to adapt the resampling process so that it reflects underlying dependencies or patterns in the data. This flexibility is essential for modern statistical applications, where the independent and identically distributed framework is often an unrealistic assumption.

The bootstrap method is an excellent approach to investigate the properties of estimators in multiple linear regression when the traditional parametric assumptions on the distribution of data are not satisfied. In a standard multiple linear regression model, the response variable Y can be expressed as a linear combination of predictor variables x—mathematically represented as:

$$Y_i = x_i'\beta + \epsilon_i \qquad i = 1, 2, \ldots, n, \tag{2.109}$$

[5]The notation $\mathcal{P}(A|B)$ is used for the conditional probability of A given B.

where x_i denotes a p-dimensional vector of predictors, β represents the vector of unknown regression coefficients, and ϵ_i are random errors. The least squares estimator (LSE) for the vector of unknown coefficients β minimizes the residual sum of squares:

$$\hat{\beta} = \arg\min_{\beta} \sum_{i=1}^{n} (Y_i - x_i'\beta)^2. \tag{2.110}$$

Under standard assumptions, such as errors ϵ_i being independent and identically distributed with zero mean and constant variance, the LSE has well-defined properties, including unbiasedness and efficiency. However, these assumptions are frequently violated in practice, necessitating non-parametric methods like the bootstrap [117].

One of the central contributions of the bootstrap lies in its ability to approximate the sampling distribution of the LSE without relying on strict distributional assumptions. By generating pseudo-samples from the empirical distribution of residuals, it provides an empirical basis for inference. In regression models, the residuals from the fitted model are defined as:

$$e_i = Y_i - x_i'\hat{\beta}, \tag{2.111}$$

To preserve the zero-mean property of the errors, these residuals are often centered as follows:

$$\tilde{e}_i = e_i - \overline{e}, \quad \text{where} \quad \overline{e} = \frac{1}{n}\sum_{i=1}^{n} e_i, \tag{2.112}$$

The centered residuals are then resampled with replacement to generate bootstrap pseudo-responses:

$$Y_i^* = x_i'\hat{\beta} + e_i^*, \tag{2.113}$$

where e_i^* are sampled residuals. For each bootstrap sample, a new estimate $\hat{\beta}^*$ is calculated, producing a distribution of bootstrap estimates. Repeating this process a large number of times ensures convergence to the true sampling distribution of $\hat{\beta}$, this is closely tied to results from the Central Limit Theorem (CLT) [119]. Moreover, the validity of the bootstrap hinges on the empirical residual distribution approximating the true error distribution, and the bootstrap achieves second-order accuracy, reducing bias and better estimating variance compared to first-order methods[117].[6]

[6] A method is considered first-order accurate if converges to the true value at the same rate

Another critical focus of the bootstrap is the estimation of covariance and correlation matrices among parameter estimates, which are essential for understanding their joint variability and relationships. In section 2.6.2, we detail an example were we put in practice the bootstrap methodology and evaluate the covariance and correlation matrices.

When data dependencies, such as temporal or spatial autocorrelation, are present, the bootstrap must adapt to preserve these structures. The block bootstrap is a specialized variation designed for such cases. Instead of resampling individual observations, this method divides the data into contiguous blocks to preserve the correlation structure within each block. For example, in a time series context, blocks of consecutive observations are resampled, maintaining the temporal order within each block. This approach ensures that dependencies in the data are reflected in the bootstrap replicates, leading to more accurate estimates of sampling distributions and covariance structures [108, 117].

The bootstrap method is a useful tool in the analysis of experimental data with known uncertainties, especially combined with likelihood-based methods. In such cases, the uncertainties associated with the measurements enter the resampling structure such that the intrinsic variability of the data is faithfully captured in the analysis. Bootstrap resampling methods are explicitly developed by adding perturbations to the observed data based on their stated uncertainties, which are often modeled as stochastic samples from a specific distribution, such as a Gaussian centered on the measured values with a variance equal to the reported uncertainty. This approach strengthens likelihood-based methods by providing a robust, non-parametric means of assessing the variability in parameter estimates in complex models where analytical solutions may be untenable. Combining bootstrap resampling with likelihood maximization methods allows one to construct confidence intervals and estimate uncertainties in a manner that is both computationally tractable and faithful to the empirical character of the data. This methodological synthesis makes sure that irreducible noise inherent in experimental measurement itself is included in the inferential framework and enhances the reliability of the obtained results [117, 120].

as the sample size increases, in contrast, the second order accuracy accounts for corrections beyond the leading-order terms, effectively capturing more refined characteristics of the sampling distribution, such as skewness or higher-order dependencies.

In cases where the dependent variable represents a limitation or a constant value and the primary source of variability exists in the independent variables, there is the possibility of adopting the bootstrap approach through resampling of the independent variables in place of the dependent variable. This technique requires inverting or rewriting the model to express the dependent variable as a function of independent variables so that the property of the constant value nature of the dependent quantity holds good. By resampling independent variables from their empirical or theoretical distributions, one is able to propagate variability through the model and subsequently estimate uncertainties of derived parameters or predictions. The robustness of this approach is based on the principle that the bootstrap fundamentally relies on the approximation of the sampling distribution of an estimator, a property that remains intact under model transformations. By emphasizing the variation in independent variables, this procedure accommodates the limited range of the dependent variable while preserving the statistical integrity of the bootstrap method. Resampling the independent variables ensures proper representation of their empirical distribution and any possible interdependence or correlation among them—conditions that make one's inferences about the dependent variable robust and meaningful when direct resampling of the latter cannot be performed [121, 122]. In the section 2.6.2 we detail an example using the bootstrap technique.

2.6.2 Application of the Bootstrap Method: A Practical Example

To clarify the bootstrap technique, we present a detailed hands-on example involving a quadratic fit. Specifically, we compare the results from the MIGRAD and MINOS routines. Consider a model $y = 0.5x^2 + 0.3x + 0.1$ and generate $N = 50$ datapoints uniformly in the range $x \in [-14, 10]$, and to complement with the error/uncertainty analysis, For each data point, we assign an uncertainty Δy_i sampled from a Gaussian distribution (as described before) with zero mean and $\sigma = 0.9$. Then calculate the noise $\nu_i = \hat{\nu} \times \Delta y_i$ where $\hat{\nu}$ is drawn from a Normal distribution. The final data points are then computed as: $y_i = 0.5x^2 + 0.3x + 0.1 + \nu_i$, with the associated errors Δy_i.

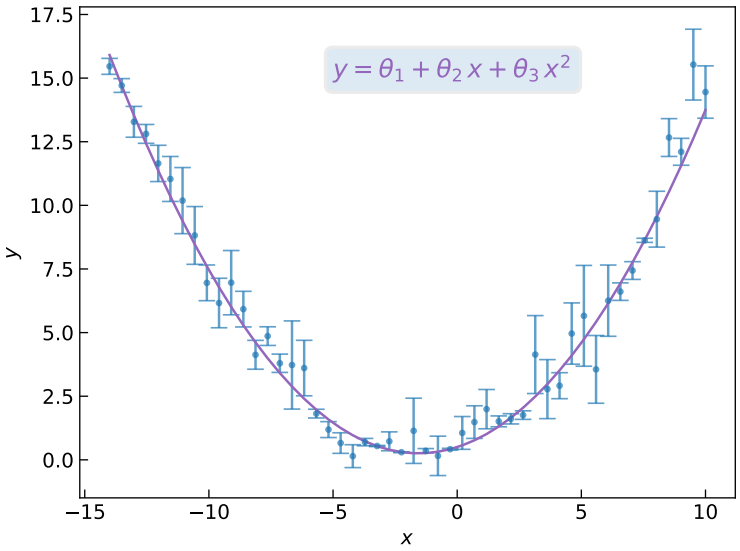

Figure F.2.13: Datapoints and best fit found for the quadratic fit example.

Figure F.2.13 depicts the generated datapoints. To fit this data set to our quadratic model $y = \theta_1 + \theta_2 x + \theta_3 x^2$, we apply the MINUIT χ^2-minimization algorithm. The best fit found (BFF) has $\chi^2_{BFF}/\text{dof} = 55.03/(50-3) = 1.17$ where dof stands for *degrees of freedom* and $\theta_1 = 0.1011 \pm 0.0008$, $\theta_2 = 0.314 \pm 0.006$ and $\theta_3 = 0.501 \pm 0.018$. The errors are computed with the MIGRAD routine, and the MINOS routine gives the same answers in this example because the likelihood is symmetric by construction.

Now, we repeat the analysis using the bootstrap technique. Although often called non-parametric since it does not rely on strong assumptions about the distribution of the underlying data, it can also be used in a parametric context when such assumptions are justified. The idea of bootstrapping is that inference about a population from sample data can be modeled by resampling the sample data and performing inference about a sample, from the resampled data [108]. In doing so, we first find the best fit by minimizing the χ^2. Then we construct new pseudodata sets $\{\tilde{y}\}$ by resampling each data point, consistent with the original experimental measurements. This is shown in Figure F.2.14. The errors on the pseudodata sets are retained at the same values as those of the original values, $\{\Delta y\}$. Each pseudodata set is then refit using the original model, yielding a new set of parameters θ_1 along with the associated $[\chi^2_{BS}]$, where BS stands for the bootstrap method. This is done many times until one has adequate statistical significance. We call each fit to a given pseudodata set a *BS fit*. The output of this procedure are

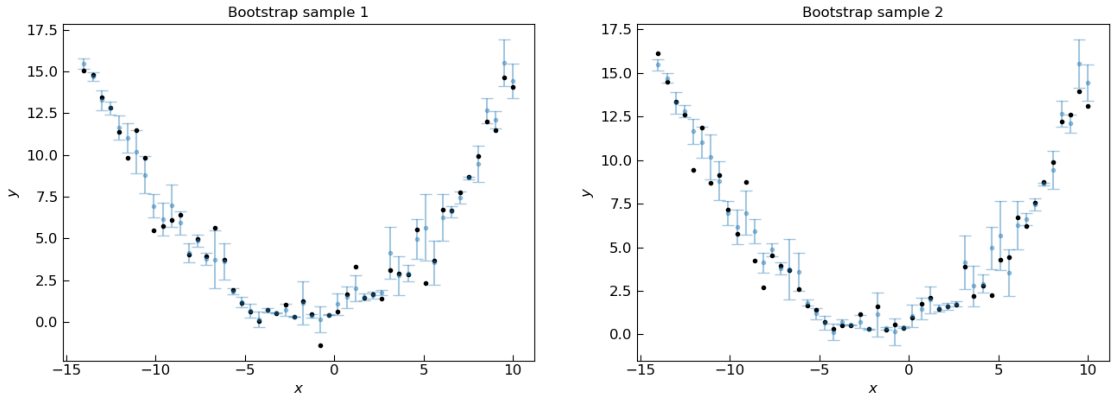

(a) (b)

Figure F.2.14: Pseudodata generated using the bootstrap technique, (a) and (b) are two samples from the $M = 10^3$ used for the example in section 2.6.1. The original dataset is in light-blue and the pseudodata sample are the black points.

histograms for the distribution of the parameters $\{\theta\}$, along with the corresponding χ^2_{BS} values. As the uncertainties Δy_i are assumed to be distributed according to a Gaussian distribution, the χ^2_{BS} values are distributed according to a noncentral χ^2 distribution [21].

$$\chi^2_{nc}(x|k,\nu) = \frac{1}{2}\exp\left[-\frac{\nu+x}{2}\right]\left(\frac{x}{\nu}\right)^{(k-2)/4} I_{(k-2)/2}(\sqrt{\nu x}), \tag{2.114}$$

where $\nu = \chi^2_{BFF}$, k represents the number of degrees of freedom (dof). The figure F.2.15 illustrates the comparison between equation (2.114) and the $\{\chi^2_{BS}\}$ distribution from the $M = 10^4$ BS fits. The peak of the distribution is approximately at $2\chi^2_{BFF}$. The same figure F.2.15 also shows the $\{\theta_1\}$ and $\{\theta_2\}$ histograms, which exhibit Gaussian shapes. These yield parameter estimates $\theta_1 = 0.1011 \pm 0.0008$, $\theta_2 = 0.314 \pm 0.006$ and $\theta_3 = 0.501 \pm 0.018$, consistent with results from MIGRAD. The expected parameter values are computed as the mean of the respective histograms for $\{\theta_1\}$, $\{\theta_2\}$ and $\{\theta_3\}$. The uncertainties are derived as the 16th to 84th quantiles, corresponding to the 1σ (68%) confidence level. Higher confidence levels can be obtained by calculating appropriate quantiles, provided a sufficiently large number of bootstrap (BS) fits are performed. The accuracy of such confidence levels improves with the number of fits, according to a scaling law of $1/\sqrt{M}$, where$M$ is the total number of BS fits. For example, with a total of

$M = 10^3$ bootstrap samples, the resulting accuracy is around 3.2%. Nevertheless, such an accuracy level is not good enough to claim a 2σ confidence interval (95.5%) [21] in our analysis.

The covariance and correlation matrices can be directly calculated from the bootstrap (BS) fits as follows:

$$\mathrm{cov}(\theta_i, \theta_j) = \sum_{k=1}^{M} \frac{([\theta_i]_k - \langle\theta_i\rangle)([\theta_j]_k - \langle\theta_j\rangle)}{M}, \tag{2.115a}$$

and

$$\mathrm{corr}(\theta_i, \theta_j) = \frac{\mathrm{cov}(\theta_i, \theta_j)}{\sqrt{\mathrm{cov}(\theta_i, \theta_i)}\sqrt{\mathrm{cov}(\theta_j, \theta_j)}}. \tag{2.115b}$$

The covariance and correlation matrices closely resemble those computed using the MIGRAD algorithm, demonstrating consistency between the bootstrap analysis and the standard optimization method:

$$\mathrm{cov}(\theta_1,\theta_2,\theta_3)_{Hessian} = \begin{bmatrix} 342.0 & 66.51 & -4.71 \\ 67.0 & 33.01 & 0.29 \\ -5.0 & 0.29 & 0.59 \end{bmatrix} \times 10^{-6}, \quad \mathrm{corr}(\theta_1,\theta_2,\theta_3)_{Hessian} = \begin{bmatrix} 1.00 & 0.62 & -0.33 \\ 0.62 & 1.00 & 0.06 \\ -0.33 & 0.06 & 1.00 \end{bmatrix},$$

$$\mathrm{cov}(\theta_1,\theta_2,\theta_3)_{BS} = \begin{bmatrix} 342.0 & 66.51 & -4.71 \\ 67.0 & 33.01 & 0.29 \\ -5.0 & 0.29 & 0.59 \end{bmatrix} \times 10^{-6}, \quad \mathrm{corr}(\theta_1,\theta_2,\theta_3)_{BS} = \begin{bmatrix} 1.00 & 0.62 & -0.33 \\ 0.62 & 1.00 & 0.06 \\ -0.33 & 0.06 & 1.00 \end{bmatrix}.$$

Hence, we have demonstrated that the bootstrap and the standard Hessian methods yield compatible results, provided that a sufficient number of BS fits are performed.

The calculation of any observable $g(\theta)$ and the propagation of associated uncertainties is a straightforward process. For each parameter set $[\theta]_i$ obtained from a BS fit, the observable is evaluated as $g_i = g([\theta]_i)$, producing M values of g_i. From the resulting histogram, the expected value $\langle g\rangle$ and its uncertainties can be determined, analogous to the method applied for the parameters θ. This procedure is agnostic to the functional form of g, ensuring that both the uncertainties in the parameters and their correlations are fully propagated to the observable. Consequently, despite its computational intensity, the bootstrap method remains a robust and effective tool for analyzing data and quantifying uncertainties [21].

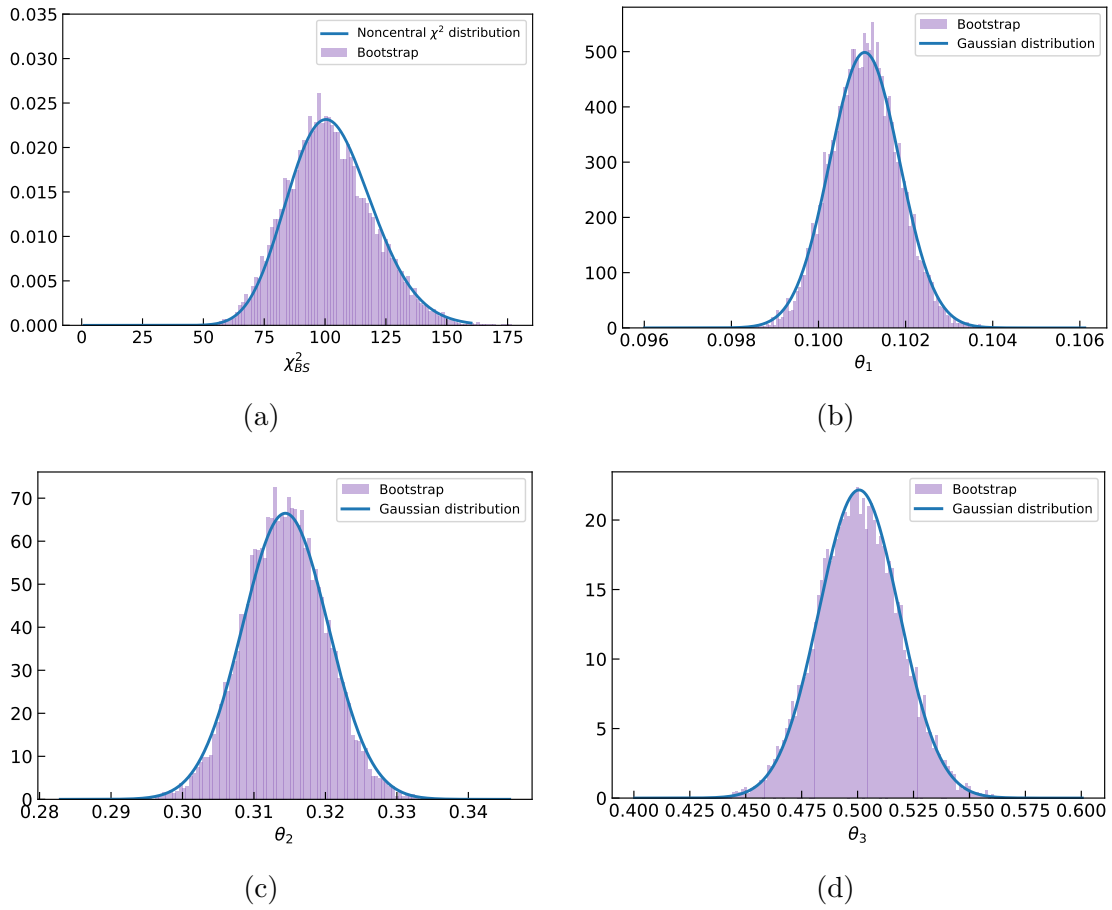

Figure F.2.15: (a) Theoretical non-central χ^2 distribution compared with the histogram derived from bootstrap estimates for χ^2_{BS}. (b) Theoretical Gaussian distribution contrasted with the histogram obtained from bootstrap evaluations for the parameter θ_1. (c) Theoretical Gaussian distribution compared against the histogram generated from bootstrap approximations for the parameter θ_2. (d) Theoretical Gaussian distribution analyzed in relation to the histogram constructed from bootstrap fits for the parameter θ_3.

We have illustrated the method on data from a quadratic model with statistically independent parameters and Gaussian-distributed uncertainties. For a detailed description of the procedure applied to a linear model, we refer the reader to [21]. In this case, there was a unique minimum for the BFF, and the histograms of $\{\theta\}$ and $\{\chi^2_{BS}\}$ were Gaussian and non-central χ^2 distributed, respectively. The extension of the method to other distributions is straightforward, both in terms of the likelihood function and in the process of generating pseudodata sets. When the experimental data points are correlated, one can construct pseudodata consistent with the correlation matrix. In addition, systematic uncertainties can be included as correlated errors. However, a problem arises when systematic and statistical uncertainties are propagated at the same time because these uncertainties can not be disentangled in the resulting observables.

In presence of a nearby local minimum for BFF, the Bootstrap sometimes swings over from global to that particular local minimum. Correspondingly, the distribution of a parameter may take a structure of two peaks, where all expected values, as well as their uncertainties or quantities derived thereof, shall be interpreted carefully. While it is technically possible to compute uncertainties and fit each minimum separately, the question of which minimum is better and what inferences can be drawn requires careful consideration. The answer to this depends partly on whether peaks in parameter histograms are well separated, partly on how correlated model parameters are, and partly on to what extent fits from different minima exhibit consistently diverging likelihoods functions. The problem lacks a universal solution; thus, each case must be examined individually and interpreted within its physical context. Additionally, bootstrap results provide a means of comparing two models of approximately similar quality by analyzing the distributions of $\{\chi^2_{BFF}\}$ and $\{\chi^2_{BS}\}$. For two models, each one can be fitted to the same pseudo-data set, and their results compared for each BS fit. If one is consistently better than the other, then it can be regarded as being the better model [21].

3. Results

We have no right to assume that any physical laws exist, or if they have existed up until now, that they will continue to exist in a similar manner in the future.

M. Planck

In this chapter we provide an overview of the three major analyses where we explore different aspects of hadron phenomenology and resonance studies. In all of them we rely on a combination of theoretical frameworks and statistical techniques.

1. Regge theory and hadronic phenomenology are applied to the low-lying baryon spectrum; the formalism of complex angular momentum is used to investigate N^* and Δ^* resonances within the framework of basic principles of S-matrix theory as a very powerful tool for the analysis of scattering amplitudes with the understanding of the resonance structure. By continuing work on the extension of this formalism, we have been able to identify useful information about the behavior of these resonances at high energies. Results from this work have been published in [95].

2. The near-threshold $P_c(4312)^+$ resonance discovered by LHCb in 2019 is studied within general principles of the S-matrix theory. This analysis also compares various parametrizations, enabling a comprehensive study of $P_c(4312)^+$ in light of other theoretical models. The obtained results allow more clarity in understanding the structure of the resonance itself and help refine models already existing about hadron dynamics near thresholds.

3. The extension of the method applied in the study of $P_c(4312)^+$ to the case of the $f_0(980)$ resonance, which also appears near the $K\bar{K}$ threshold. The proximity of the $f_0(980)$ to that threshold had been a source of great interest in its properties.

The bootstrap technique is employed for all these three cases to pursue a comprehensive statistical analysis and uncertainty quantification. As a matter of fact, this is a very useful method that enhances the reliability and robustness of the results [118, 120, 121].

3.1 Analysis of the N^* and Δ^* spectrum using Regge phenomenology

In the work [95], we employed Regge phenomenology to analyze the pole structure of the N^* and Δ^* spectra, extending and complementing the investigation formerly carried out in the strange baryon sector as reported in Ref. [102].

The sector of low-lying non-strange baryons, containing the N^* and Δ^* resonances (the excited states of nucleons), is a crucial path toward understanding the quark model as well as quantum chromodynamics (QCD) in the non-perturbative regime. Such resonances can be investigated by means of pion-nucleon scattering and photoproduction experiments, providing essential information (see F.1.1).

N resonances correspond to energies where a nucleon may absorb the right amount of energy to move into a higher energy state. Eventually, the resonances will decay into lower states. Examples include the Roper resonance $N(1440)$ and the $N(1520)$ with distinct masses, decay widths, and quantum numbers. Because many parameters, such as mass and width, are extracted experimentally, the hadronic models need to be fine-tuned to develop an understanding of nucleon structure. These resonances appear in pion-nucleon and photon-nucleon scattering experiments.

Δ resonances differ from N resonances only in their isospin. Whereas nucleons have isospin $I = 1/2$, Δ resonances have isospin $I = 3/2$. They therefore come in four distinct charge states: Δ^{++}, Δ^{+}, Δ^{0}, and Δ^{-}. One of the most important one of these is the $\Delta(1232)$ resonance, which is very relevant for pion-nucleon interactions. It gains its accessibility with a relatively low mass and a short lifetime within a wide range of hadronic processes. Extensive studies of the $\Delta(1232)$

resonance in scattering experiments have imposed critical constraints on theoretical models that describe baryon interactions. Its role is not solely confined to the scattering processes but also extends to studies of the spectrum of baryons and the strong interactions within baryons. The N and Δ resonances are more important in the wider context, however, for what they can teach about the non-perturbative aspects of QCD. The perturbative form of QCD explains only high-energy processes where the strong force becomes weak; the low-energy behaviors of baryons involve much stronger coupling between quarks and gluons. N and Δ resonances are interactions that have significant implications for the study of models developed to explain such phenomena as quark confinement and chiral symmetry breaking. Techniques such as partial wave analysis and coupled-channel models offer perspectives for the precise extraction of the parameters of these resonances, thus contributing to refining theoretical approaches in hadronic physics.

Most of the analyses of resonances in this section are based on different datasets, each with its own peculiarities and requiring sophisticated methods for the precise extraction of resonance signals. Data from measurements of hadronic scattering processes often include pion-nucleon (πN) and nucleon-nucleon (NN) interactions, as well as data describing near-threshold phenomena. Each of the various datasets requires due care in considering experimental uncertainties and theoretical models employed to interpret the results.

Extraction of resonance signals from such data sets faces several challenges, which are physical, mathematical as well as computational. The central difficulty lies in isolating the true resonance signals from the background noise and other non-resonant contributions presents itself in the scattering data. This is particularly important when one is dealing with overlapping resonances or those of broad widths where the distinct peak structure in the amplitude is not well defined. Scattering amplitude $T(s,t)$ in those analysis is expanded into partial waves and decomposed into components of angular momentum. Such decomposition allows the identification of individual resonances by analyzing the partial wave amplitudes as functions of energy and momentum transfer.

In [95] we fit complex Regge trajectories to the spectra obtained by several partial wave analyses of meson scattering and photoproduction data, from all available analysis we study only the ones that includes uncertainties in their

extractions as we will apply the bootstrapping technique 2.6.1. In what follows, a brief description of the models employed to extract the pole parameters is presented.

3.1.1 The Carnegie–Mellon–Berkeley pole extractions

The Carnegie–Mellon–Berkeley (CMB) πN partial wave analysis presented in [123, 124] represents an elaborate investigation of pion-nucleon scattering in the energy range between 0.42 and 2.0 GeV. It provides the extraction of important resonance parameters - mass, width, and elasticity - for the resonances under consideration, namely for the N and Δ states. Results of this analysis have been extensively used by the Particle Data Group (PDG) [8], and hence the above-mentioned papers are a vital reference in hadronic phenomenology studies.

The partial-wave amplitudes are parametrized in the multichannel model within the CMB analysis. A scattering matrix has to be used to describe a strong coupling between several inelastic channels; that will give a more accurate description of the complex interactions occurring in the pion-nucleon scattering. In addition to the elastic channel, the model includes the quasi-two-body channels $\pi\Delta$, ρN, ηN, ϵN, ωN, πN^* and $\rho\Delta$. A non-resonant $\pi\pi N$ channel is also included. This multichannel framework is necessary to take into account the couplings with the intermediate states in order that all the physical processes relevant to the analysis can be included.

In order to improve the accuracy of the resonance extraction, the standard Breit-Wigner resonance form is modified by introducing an energy-dependent phase space factor. This modification permits the model to take into account a properly varying phase space that becomes available for given energies, in particular in the πN elastic channel. This factor is included to ensure that the resonances were represented with higher precision, particularly in regions where phase space effects become prominent, like near thresholds.

It also includes dispersion relations and analyticity constraints. Dispersion relations connect the real and imaginary parts of the scattering amplitude and guarantee that the model satisfies basic principles like causality and crossing symmetry. These constraints often enable the extraction of resonance parameters

without ambiguities, which generally appear, in particular when dealing with overlapping resonances or broad-width states. By imposing these conditions, the CMB analysis enhances the stability and robustness of the resonance parameters extracted from the data.

The fitting process in the CMB analysis involves iteratively constructing partial-wave amplitudes and applying these dispersion relations in such a way that the amplitude is always consistent both with the high-energy behavior and with the behavior at low energies calculated by theory. Besides, the fitting procedure treats experimental uncertainties very cautiously, using sophisticated statistical methods to avoid bias and to extract resonance signals with high confidence.

3.1.2 The Jülich–Bonn pole extractions

Pole parameters from [125] were obtained using the Jülich–Bonn (JüBo) 2017 coupled-channel model. The JüBo coupled-channel model conducts an exhaustive analysis of general photoproduction reactions, with a particular focus on the $K^+\Lambda$ final state. This work extends the basic framework of the original JüBo model to include photoproduction, allowing for the determination of nucleon and Δ resonance parameters in this new regime. In this model, a dynamical coupled-channel (DCC) approach is applied, fully respecting unitarity and analyticity. This makes it highly reliable for deducing the resonance spectrum in terms of complex pole positions and residues.

The dataset used in this study totals more than 40,000 data points for various reactions, such as pion-induced processes like $\pi N \to K\Lambda$, and photon-induced reactions like $\gamma p \to K^+\Lambda$. This extensive dataset enables the model to fit a wide energy range, reaching up to 2.3 GeV in the center-of-mass frame, and includes recent high-quality polarization observables.

The JüBo model is designed using time-ordered perturbation theory (TOPT), constructing a scattering potential that is iterated within a Lippmann-Schwinger equation to ensure two-body unitarity. Approximate three-body unitarity is also considered, with effective treatment of channels like ρN, σN, and $\pi\Delta$. These

channels are dynamically included by fitting their phase shifts to the experimental data.

The partial wave decomposition is a method used to express the scattering amplitude, $T_{\mu\nu}(q, p', E_{cm})$, in a partial wave basis, bringing together pole and non-pole terms. The pole terms account for the genuine s-channel resonances, while the non-pole terms capture the t- and u-channel exchanges. This decomposition clearly identifies dynamically generated resonances, which are induced by the unitarization of background processes, even when no explicit s-channel poles are present.

Further analysis of the complex pole structure of the scattering amplitude on unphysical Riemann sheets allows the extraction of the resonance spectrum. Poles closest to the physical axis provide the most reliable resonance information. Several nucleon and Δ resonances have been identified in the JüBo approach, including dynamically generated ones that appear without the need to introduce explicit s-channel poles manually. In particular, the model identifies a second s-channel pole in the P_{13} partial wave and a newly dynamically generated resonance in the D_{15} wave.

In total, the JüBo framework fits more than 48,000 data points using 761 free parameters, which include hadronic couplings, bare masses of the s-channel resonances, and photonic couplings. A parallelized χ^2 minimization using the MINUIT algorithm is employed on a supercomputer to handle the large computational demand. The analysis also incorporates statistical re-weighting techniques to estimate uncertainties in the extracted resonance parameters.

Involved polarization observables, such as recoil polarization P and beam-recoil observables C_x and C_z, have played a significant role in the $K^+\Lambda$ channel in constraining the resonance spectrum. High-quality data from the CLAS and MAMI collaborations have been particularly influential in refining the resonance parameters and photonic couplings.

The JüBo analysis further addresses inconsistencies in various experimental datasets, particularly regarding differential cross sections for $\gamma p \to K^+\Lambda$, where discrepancies between measurements from different facilities are noted. Despite these challenges, the model achieves good agreement with most of the provided

polarization data, contributing to a better understanding of $K^+\Lambda$ photoproduction.

All these features—unitarity, analyticity, and simultaneous fitting of the hadronic and photonic final states—make the JüBo framework a powerful tool in studying baryon resonance spectra and addressing the missing resonance problem.

3.1.3 The Bonn–Gatchina pole extractions

The multichannel partial wave analysis Bonn–Gatchina (BnGa), presented in the works [126, 127], represents a comprehensive effort towards the extraction of both nucleon and Δ resonances in hadronic interactions. In both studies, emphasis is given on the extraction of resonance parameters from scattering and photoproduction data by means of complementary methods that supplement each other for a better conceptual understanding of the resonance spectrum.

In [126] a multi-channel PWA is used that separated the scattering amplitudes into well-defined contributions from different partial waves. This helps in identifying resonance like $N(1900)3/2+$, $N(1900)3/2+$ and $N(1975)3/2+$, $N(1975)3/2+$. The coupled-channel model allows the to perform a fit for several reactions simultaneously. This helps resolve overlapping signals and produces a better fit. This approach again relies heavily on polarization data, since the polarization information is crucial in establishing the nature of spin and parity of the resonances. Overlapping resonances, however, combined with the sensitivity of the model to different sets of data, has created severe difficulties in unambiguously identifying these resonances.

In contrast, the study [127] focuses specifically on the photoproduction of two neutral pions in proton interactions. For this study, data was taken from the Crystal Barrel/TAPS experiment performed at the ELSA accelerator. Similar to the first paper, a coupled-channel model was implemented; however, much focus is put on the search for "missing" resonances-those that are predicted by theoretical models but not yet experimentally confirmed.

The authors point out that these resonances play an important role not only in the investigation of the pion production mechanism but also in the study of nucleon interaction behavior by analyzing photoproduction data and using polarization

observables. The hints which appear indicate that the resonances may be really critical for a fundamental view of strong interaction dynamics, which would therefore provide a considerable motivation for an investigation of those elusive resonances in greater detail.

Whereas both the above studies address different aspects of the analyses, the inherent complexities in determining nucleon resonances are brought out. While differing in their methodologies, the two analyses employ rigorous statistical approaches, including log-likelihood and least squares methods, to ensure that the parameters extracted are indeed proper and meaningful. However, some of the persistent problems in identifying overlapping resonances and ambiguities in parameter assignments remain part of the problem in baryon spectroscopy.

The following datasets we use in our Regge analysis apply the Laurent-Pietarinen (LP) technique, which is a technique for resonance parameters extraction via efficient modeling of both resonant and non-resonant parts of the scattering amplitudes. The LP method is an analytical technique extensively employed in hadronic spectroscopy to extract resonance parameters, such as pole positions and residues, directly from experimental data. It grounds itself on the elementary principles of complex analysis in that it combines in one role-that of a Laurent series-responsible for encapsulating the resonant or pole contribution within the Pietarinen series, tailored for nonresonant background effects. This approach yields a flexible, model-independent framework that avoids the need for an explicit general theoretical model of the scattering amplitude. Instead, the method focuses attention on the analytic properties of the amplitude, making it particularly effective for a wide variety of scattering processes.

In its central formulation, the LP method splits the amplitude in resonant and non-resonant parts. The resonant contributions are parameterized by a Laurent series expansion about the complex poles corresponding to physical resonances. For a resonance at the pole W_i, the amplitude can be expanded as:

$$T_R(W) = \sum_{i=1}^{k} \frac{R_i}{W - W_i} + \text{regular terms}, \tag{3.1}$$

In this notation, R_i denotes the residue of the particle associated with the $i - th$

resonance, while W_i is its corresponding pole position. In this framework, the resonant properties, namely mass and width of a resonance, are explicitly defined by means of the analytic continuation of the amplitude in the complex plane. The Laurent series represents a proper parametrization of resonant phenomena even in situations when the resonances may partly overlap or show broad structures since the series effectively converges around the mentioned singularities.

The methodology follows the Pietarinen series in characterizing the non-resonant background, which is based on a method of conformal mapping. The series effectively captures the general effects caused by the presence of branch cuts due to multiple physical thresholds. The series has the following representation:

$$T_B(W) = \sum_{n=0}^{N} c_n X(W)^n, \tag{3.2}$$

where $X(W)$ is the Pietarinen function, introduced by the branch point x_p and c_n denotes coefficients obtained from a fit to experimental data. The Pietarinen function is given in the following form:

$$X(W) = \frac{\alpha - \sqrt{x_P - W}}{\alpha + \sqrt{x_P - W}}, \tag{3.3}$$

Here, α is a free parameter and x_P denotes the position of the branch point due to physical cuts, either from the πN or ηN thresholds. Further, more complicated inelastic contributions can be added by adding branch points at x_Q and x_R, each series representing an independent non-resonant background contribution. The flexibility in the Pietarinen series allows a good description of a wide variety of physical phenomena with no explicit and necessarily complicated theoretical assumptions for each branch cut. In fact, the Laurent plus Pietarinen series constitutes the basic formalism of the LP approach, enabling one to effectively separate the resonant and non-resonant parts of the scattering amplitude. This procedure proves especially useful in those cases where the standard methods of PWA face specific technical problems, such as the case of overlapping resonances, or when the non-resonant structures become complicated.

In contrast to the PWA, which defines the angular momentum components of the amplitude, the LP method focuses on the analytic properties of the amplitude. For

this reason, the approach allows one to obtain precise resonance parameters, even in situations where the basic theoretical model is uncertain or incomplete, and hence can provide a high level of model independence. The key advantage of the LP approach follows from its ability to enhance only selectively the amplitude around the relevant poles, without any need to characterize the full amplitude over the complete energy spectrum. That makes the method particularly well-suited for SE (Single Energy) fits, where the standard techniques face serious problems due to the discreteness in the database.

It has equal efficiency in ED (Energy Dependent) fittings, as it has been applied with success to analyze multi-channel data in a rather wide range of scattering phenomena. The flexibility of the Pietarrien series permits to parametrize non-resonant background terms in many channels, while the Laurent series maps precisely the resonant poles. In practice, the parameters of the Laurent and Pietarinen series are changed to fit the experimental data using optimization algorithms such as MINUIT. The fit aims at the minimum difference between the theoretical model and the data observed. This fitting procedure ensures that not only the resonant part but also the non-resonant part is accurately described. Thereafter, the LP approach was applied proficiently to the analysis of several hadronic processes that demand high accuracy within the GWU-SAID and Karlsruhe-Helsinki frameworks, where it plays a vital role in extracting reliable pole parameters from pion-nucleon scattering and photoproduction data.

3.1.4 The SAID (SE) pole extractions

Pole parameters obtained in [128] from a fit to the single-energy (SE) SAID–GW WI08 partial waves of πN elastic scattering [129] using the Laurent+Pietarinen (LP) approach.

The SE technique used in the SAID analysis provides an approach to the understanding of pion-nucleon elastic scattering. It allows for the model-independent framework for partial-wave amplitude studies at specific energies. Unlike the ED (energy dependent) fits, the SE solutions do not assume an analytic continuous function over a very large energy interval and hence enable a

more detailed study of the nature of the scattering amplitude at a specified interval of energy. This may be an important local point of view for distinguishing deviations from global solutions of equilibrium distributions and for finding additional resonances which are difficult to obtain in the global treatment.

The SE method begins with the extraction of partial-wave amplitudes in narrowly defined energy intervals, assuming that the energy dependence is linear within each interval. While this procedure lacks the smoothness or analyticity constraints of ED fits, it gives the SE solutions the latitude to reflect possible structures in the scattering amplitude that might otherwise be smoothed over in ED analyses. The SE fits are thus particularly useful for discovering new resonances or finer structure in known resonances that may not be well-resolved in ED solutions. One of the advantages of the SE fits is that they are able to extract detailed snapshots of the scattering process unencumbered by global assumptions concerning the analytic structure of the amplitude. In [128] additional poles in the S_{11} and P_{11} partial waves-resonances were uncovered by the SE fits not present in the ED fits. Furthermore, the spectral evolution analysis manifested the formations in both the D_{13} and F_{15} partial waves, which hinted at the complex resonance dynamics not captured by the more uniform energy-dependent solutions. These additional resonances agree with previous studies from the CMB and BnGa analyses; thus, they underpin the important role of SE fitting in refinement toward more accurate determination.

One of the key developments in the present analysis is the application of the Laurent-Pietarinen (LP) approach to SE fitting. This explicitly incorporates analyticity into what otherwise are SE solutions with discontinuities. The Laurent series captures singular behavior near poles, while the Pietarinen series accounts for the non-resonant background contributions, including branch cuts associated with physical thresholds. The LP method provides a totally independent and robust way of extracting the poles from the SE data. An error analysis is provided by varying the branch points, which ascertains the stability of the extracted resonance parameters. Application of the LP methodology in the SE approach extended the list of supplementary resonances by the ones seen in the S11 and P11 partial waves. These SE solutions, combined with the LP extraction technique, provide an essential glimpse of the resonance structure associated with pion-nucleon scattering. However, the SE fits are more susceptible to statistical noise and lack most of the

physical constraints such as unitarity and dispersion relations that guide the ED fits. The SE methodology retains a very significant role in the identification of resonances and the determination of the most complicated features they have.

3.1.5 The SAID (ED) pole extractions

Poles extracted in [128] from the energy-dependent (ED) SAID–GW WI08 partial waves of πN elastic scattering [129] also using the LP approach.

The Energy-Dependent (ED) method provides a smooth, continuous representation of the scattering amplitude over a very large energy range. ED fits are usually made using the K-matrix formalism that ensures the fit function obeys basic physical constraints like unitarity and analyticity. The K-matrix is related to the scattering amplitude $T(E)$ by:

$$T^{-1}(E) = K^{-1}(E) - i\rho(E), \tag{3.4}$$

where $\rho(E)$ includes the phase-space factor which ensures proper behavior near all physical thresholds, including the pion-nucleon channel. By imposing these constraints, ED fits produce a far more regular and smooth result across the whole energy range. ED solutions are, therefore especially suitable to give an overview of the scattering process and hence, the extracted resonance parameters will follow physical expectation. The most important advantage of ED fits comes from their ability to extract the resonance parameters using the analytic continuation of the scattering amplitude into the complex energy plane. Such methods allow for pole identification associated with physical resonances and provide, at the same time, information on the mass, width, and coupling to different channels. In [129], ED fits checked the stability of the positions of the resonances for various K-matrix parametrizations. Indeed, the investigations showed that the pole locations of prominent resonances like $N(1440)$ (Roper resonance) and $\Delta(1232)$ were stable, independent of the form adopted for the parametrization. This makes the ED approach even more reliable in pole extraction by employing the LP method for the whole analysis of the resonance structure. The Laurent-Pietarinen method provides a complementary way to the ED fits in decomposing the T-matrix into its resonant

and non-resonant parts. The Laurent expansion defines the properties due to poles, the Pietarinen series contains the non-resonant background, and discontinuities at physical thresholds are nicely accounted for. Branch point selection in the Pietarinen series is guided by physical considerations; for example, inelastic channels. This provides a flexible data-fitting method without the need for additional model assumptions. ED analysis also applied fixed-t dispersion relations to improve the fit to experimental data. In any case, these constraints had the effect of making the resonance parameters extracted in the ED solutions consistent with the theoretical expectations, hence particularly reliable in high-precision studies of hadronic interactions. These smooth ED fits nevertheless captured most of the essential resonance structures, including the well-known nucleon and delta resonances but also less conspicuous structures in the S_{11} and F_{15} partial waves. While the ED fits represent a globally consistent solution, they are less sensitive to fine, localized structures that might be revealed by SE fits. For example, additional resonances uncovered by the SE approach in the P_{11} and S_{11} partial waves were not as prominent in the ED analysis. On the other hand, the added physical constraints in ED solutions provide a more stable and smooth representation of the scattering process throughout the full energy spectrum.

3.1.6 The Karlsruhe–Helsinki pole extractions

Pole extracted in [130] from the Karlsruhe–Helsinki (KH80) [131] partial wave analysis of πN elastic scattering employing the LP approach.

The KH80 analysis is one of the most extensive and pioneering analyses in the realm of πN scattering. It spans a vast energy range from the threshold of pion-nucleon to about 2 GeV and uses fixed-t dispersion relations with partial wave analysis to extract vital resonance parameters from experimental data. The work focused on the study of elastic and inelastic πN -scattering, invoking from the very beginning a complex mathematical framework that would guarantee that the deduced amplitudes satisfy the unitarity and analyticity principles.

KH80 analysis begins with the partial-wave series associated with the scattering amplitude. The total scattering amplitude $T(s, \theta)$ is written as a sum over partial

waves, each of which an independent partial-wave amplitude $T_\ell(s)$ is associated with given angular momentum ℓ. This decomposition defines the strength of the contributions from each angular momentum state and therefore allows for a straightforward identification of resonances, poles in the complex energy plane. The analytic continuation of the partial-wave amplitudes determines the poles of resonance, carrying information on the mass, width, and properties of the coupling, of the resonance. Amplitudes in KH80 are constrained by fixed-t dispersion relations which exploit analyticity of the scattering amplitude. These formulae relate real and imaginary parts of the amplitude via integral transforms, and thereby ensure explicit enforcement of the fundamental principles of causality and unitarity. The dispersion relations take the form:

$$\Re\,[T(s,t)] = T_{\text{Born}}(s,t) + \frac{1}{\pi}\int_{s_{\text{th}}}^{\infty} \frac{\Im\,[T(s',t)]}{s'-s}\,ds', \tag{3.5}$$

Born term is the lowest-order approximation to the scattering phenomenon, meaning involvement of the tree-level direct exchange of particles. In pion-nucleon scattering, for example, this term often comes from the direct exchange of pions or nucleons in the s-channel, t-channel, or u-channel is responsible for interactions. These contributions are the "classical" or lowest-order components of a perturbative series expansion of the scattering amplitude. One of the major problems with using the Born approximation is that it does not inherently satisfy the requirement of unitarity: the requirement that the total probability (cross-section) for all possible outcomes of a scattering phenomenon.

The parameters of the KH80 analysis estimate the resonance properties for several nucleon and delta states, notably including the $\Delta(1232)$. Its parameters, in particular mass, width, and coupling, are fundamental input parameters for pion-nucleon dynamics as we mention before. The precision obtained in determining the $\Delta(1232)$ parameters makes these results an integral part of hadronic physics. These results enable the developing of new theoretical models, which can also rest on quark models and lattice QCD calculations. In addition, KH80 identifies several higher-mass resonances, such as the $N(1440)$ and $N(1535)$, which both improve the understanding of the nucleon excitation spectrum.

Another important characteristic of KH80 is the inclusion of inelastic channels,

which become important at higher energy where pion scattering can produce final states involving ηN, $\pi\Delta$, and ρN. The channels in question convey critical information on resonance couplings and decay behaviors, hence providing insights into the structural and dynamic characteristics of the resonances within the framework of hadronic physics. Inclusion of such inelastic contributions leads to a more comprehensive view of the resonance spectrum by KH80 and sets methodological standards that have influenced further research in pion-nucleon scattering and baryon spectroscopy.

3.1.7 The Karlsruhe–Amsterdam pole extraction

Pole extracted in [130] from the Karlsruhe–Amsterdam 1984 (KA84) [132, 133] partial wave analysis of πN elastic scattering employing the LP approach.

The KA84 analysis improves the KH80 framework by extending the energy spectrum and applying more advanced coupled-channel methods together with advanced mathematical tools, in particular, the LP expansion. This specific expansion allows KA84 to describe accurately both resonant and non-resonant features of the scattering amplitudes and thus to improve significantly the treatment of inelastic channels in pion-nucleon (πN) scattering. The analysis separate the amplitude into a Laurent series of resonant contributions and a Pietarinen series for non-resonant backgrounds, thereby getting round the difficulties of handling overlapping resonances in intractable multi-channel systems.

The incorporation of inelastic scattering channels, such as ηN, $\pi\Delta$, and multi-pion final states, represents a significant progress in the KA84 framework. These channels are essential for analyze resonance couplings and decay processes and are systematically incorporated through coupled-channel fitting methodologies. This concurrent fitting of both elastic and inelastic datasets is crucial for the precise characterization of resonances that engage in interactions across multiple channels, including $N(1650)$ and $N(1710)$, as their coupling to diverse decay pathways offers profound understanding into baryonic structure and the dynamics of hadronic decay.

KA84 further incorporates fixed-t dispersion relations, adapting them to

accommodate multi-channel interactions by sharpening phase-space factors and threshold behaviors peculiar to each channel. The connection between the real and imaginary parts of the amplitude is retained from channel to channel, thus ensuring dispersion constraints enforce analyticity and causality. This alteration is crucial for a realistic depiction of energy-dependent phase-space fluctuations and for the maintaining of the analytic integrity of the amplitude through inelastic thresholds, leading to a far more coherent determination of mass, width, and coupling parameters.

KA84 increases the energy range of the analysis, which improves the resolution of higher-mass resonances participating in the non-perturbative regime of QCD. This extension allows for the identification of complex resonances and overlapping structures, therefore making the characterization of the baryon-resonance spectrum better. Using this extended data set and new techniques for statistical analysis to handle parameter uncertainties, KA84 provides extracted parameters with increased precision and therefore sets reliable benchmarks for further studies.

Several pole extractions have been documented in the literature; however, a significant number of these studies either omit uncertainty estimations in their pole determinations or concentrate solely on the N^* spectrum, neglecting the Δ^* states (see [95]). For this reason, our comparisons are restricted to the extractions and analyses explicitly referenced above. To present a representative overview of the available studies, we summarize several notable pole extractions without intending to provide an exhaustive list. These include the SAID parameters reported in [128], based on the SAID-GW WI08 partial wave analysis [129]; Höhler's speed plot analysis of $\pi N \to \pi N$ amplitudes [134]; the Pittsburgh–Argonne National Lab (P-ANL) pole extraction [135]; the multichannel parameterization of πN amplitudes developed by Kent State University (KSU) [136]; the Argonne National Lab–Osaka (ANL-O) analysis [137]; the Giessen group's coupled-channel [138]; and the Zagreb group's CMB coupled-channel approach to the N^* spectrum [139].

In Figure F.3.1, we show the Chew–Frautschi plots [97], namely, the real part of s on the pole position and the real part of the angular momentum J in the pole position *i.e.* $(\Re[s_p], \Re[J] = J_p)$, for the N^* and Δ^* resonances. Correspondingly, in Fig. F.3.2 are the imaginary part of s on the pole position and the real part of the angular momentum J also in the pole position $(\Im[s_p], \Re[J] = J_p)$ plots of [102].

Table C.3.1: Summary of pole positions M_p, Γ_p (in MeV) for $I^\eta = \frac{1}{2}^+$ states. The pole mass is defined as $M_p = \Re[\sqrt{s_p}]$, and the width is given by $\Gamma_p = -2\Im[\sqrt{s_p}]$. Here, I represents isospin, η denotes naturality, J_p corresponds to spin, and P indicates parity. The relationship between naturality and parity is expressed as $\eta = \tau P$, where τ is the signature. For baryons, $\eta = +1$ (natural parity) if $P = (-1)^{J_p - 1/2}$, and $\eta = -1$ (unnatural parity) if $P = -(-1)^{J_p - 1/2}$. Data adapted from [95].

Name	$N(939)$	$N(1520)$	$N(1680)$	$N(2190)$	$N(2220)$
Status	****	****	****	****	****
$I^\eta_{(\tau)}\, J^P_p$	$\frac{1}{2}^+_{(+)}\, 1/2^+$	$\frac{1}{2}^+_{(-)}\, 3/2^-$	$\frac{1}{2}^+_{(+)}\, 5/2^+$	$\frac{1}{2}^+_{(-)}\, 7/2^-$	$\frac{1}{2}^+_{(+)}\, 9/2^+$
CMB	939(1), 0	1510(5), 114(10)	1667(5), 110(10)	2100(50), 400(160)	2160(80), 480(100)
JüBo	939(1), 0	1509(5), 98(3)	1666(4), 81(2)	2084(7), 281(6)	2207(89), 659(140)
BnGa	939(1), 0	1507(3), 111(5)	1676(6), 113(4)	2150(25), 325(25)	2150(35), 440(40)
SAID(SE)	939(1), 0	1512(2), 113(6)	1678(4), 113(3)	2132(24), 550(25)	2173(7), 445(21)
SAID(ED)	939(1), 0	1515(2), 109(4)	1674(3), 114(7)	2060(11), 521(16)	2177(4), 464(9)
KH80	939(1), 0	1506(2), 115(3)	1674(3), 129(4)	—	2127(27), 380(29)
KA84	939(1), 0	1506(2), 116(4)	1672(3), 132(5)	—	2139(6), 390(7)

Table C.3.2: Summary of pole positions M_p, Γ_p (in MeV) for $I^\eta = \frac{1}{2}^-$ states. The definitions of M_p and Γ_p, as well as the notation for isospin, naturality, spin, and parity, are consistent with Table C.3.1. In this case, M_p denotes the real part of the pole position, while Γ_p is derived from the imaginary part and represents the width. Data adapted from [95].

Name	$N(1720)$	$N(1675)$	$N(1990)$	$N(2250)$
Status	****	****	**	****
$I^\eta_{(\tau)}\, J^P_p$	$\frac{1}{2}^-_{(-)}\, 3/2^+$	$\frac{1}{2}^-_{(+)}\, 5/2^-$	$\frac{1}{2}^-_{(-)}\, 7/2^+$	$\frac{1}{2}^-_{(+)}\, 9/2^-$
CMB	1680(30), 120(40)	1660(10), 140(10)	1900(30), 260(60)	2150(50), 360(100)
JüBo	1689(4), 191(3)	1647(8), 135(9)	2152(12), 225(20)	1910(53), 243(73)
BnGa	1670(25), 430(100)	1655(4), 147(5)	1970(20), 250(20)	2195(45), 470(50)
SAID(SE)	1668(24), 303(58)	1661(1), 147(2.4)	2157(62), 261(104)	2283(10), 304(31)
SAID(ED)	1659(11), 303(19)	1657(3), 139(5)	—	2224(5), 417(10)
KH80	1677(5), 184(9)	1654(2), 125(4)	2079(13), 509(23)	2157(17), 412(51)
KA84	1685(5), 178(9)	1656(1), 123(3)	2065(14), 526(9)	2187(7), 396(25)

Table C.3.3: Summary of pole positions M_p, Γ_p (in MeV) for $I^\eta = \frac{3}{2}^+$ states. The definitions of M_p and Γ_p follow the same conventions as described in Table C.3.1, where M_p represents the real part of the pole position, and Γ_p corresponds to the width derived from its imaginary part. The notation for isospin, naturality, spin, and parity is consistent with that table. Data adapted from [95].

Name	$\Delta(1700)$	$\Delta(1905)$	$\Delta(2200)$	$\Delta(2300)$
Status	****	****	***	**
$I^\eta_{(\tau)}\, J^P_p$	$\frac{3}{2}^+_{(-)}\, 3/2^-$	$\frac{3}{2}^+_{(+)}\, 5/2^+$	$\frac{3}{2}^+_{(-)}\, 7/2^-$	$\frac{3}{2}^+_{(+)}\, 9/2^+$
CMB	1675(25), 220(40)	1830(40), 280(60)	2100(50), 340(80)	2370(80), 420(160)
JüBo	1667(28), 305(45)	1733(47), 435(264)	2290(132), 388(204)	—
BnGa	1685(10), 300(15)	1800(6), 290(15)	—	—
SAID(SE)	1646(11), 203(17)	1831(7), 329(17)	—	—
SAID(ED)	1652(10), 248(28)	1814(5), 273(9)	—	—
KH80	1643(9), 217(18)	1752(5), 346(8)	—	—
KA84	1616(5), 280(9)	1790(5), 293(12)	—	—

Table C.3.4: Summary of pole positions M_p, Γ_p in MeV for $I^\eta = \frac{3}{2}^-$ states. Notation as in Table C.3.1. Table taken from [95].

Name	$\Delta(1232)$	$\Delta(1930)$	$\Delta(1950)$	—	$\Delta(2420)$
Status	****	***	****	—	****
$I^\eta_{(\tau)}\, J^P_p$	$\frac{3}{2}^-_{(-)}\, 3/2^+$	$\frac{3}{2}^-_{(+)}\, 5/2^-$	$\frac{3}{2}^-_{(-)}\, 7/2^+$	$\frac{3}{2}^-_{(+)}\, 9/2^-$	$\frac{3}{2}^-_{(-)}\, 11/2^+$
CMB	1210(1), 100(2)	1890(50), 260(60)	1890(15), 260(40)	—	2360(100), 420(100)
JüBo	1215(4), 97(2)	1663(43), 263(76)	1850(37), 259(61)	1783(86), 244(194)	—
BnGa	1210.5(1.0), 99(2)	—	1888(4), 245(8)	—	—
SAID(SE)	1211(0), 100(2)	1845(31), 174(40)	1888(3), 234(6)	—	—
SAID(ED)	1211(2), 98(3)	1969(23), 248(36)	1878(4), 227(6)	1955(24), 911(24)	2320(13), 442(23)
KH80	1211(2), 98(3)	1848(28), 321(24)	1877(3), 223(5)	—	2454(15), 462(58)
KA84	1210(2), 100(2)	1844(36), 334(26)	1878(3), 246(7)	—	2301(7), 533(17)

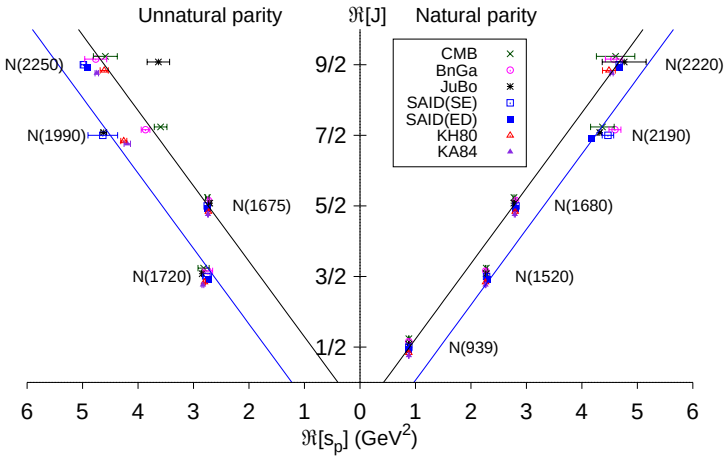

(a) N^* resonances.

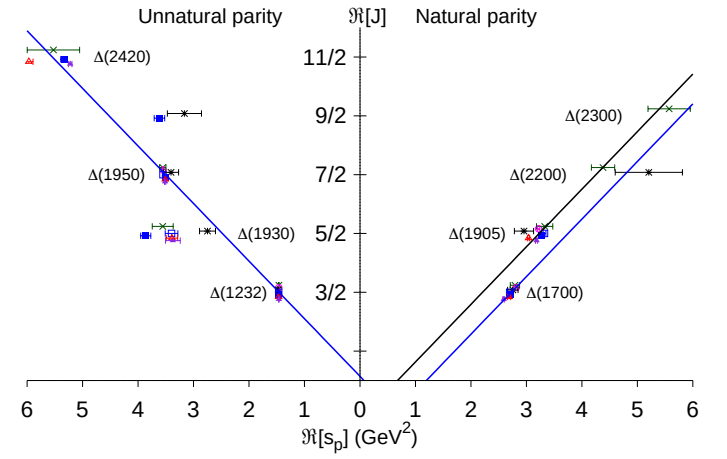

(b) Δ^* resonances.

Figure F.3.1: Chew–Frautschi plots ($(\Re[s], \Re[J])$) depicting the leading N^* and Δ^* Regge trajectories from [95]. Solid black (blue) curves represent linear fits ($J_p = a + b \times \Re[s_p]$) to the displayed positive (negative) signature data points. All trajectories share the same slope (b), consistent with the MacDowell symmetry constraint [103]. A fit for the $\frac{3}{2}^+_{(+)}$ states is omitted, as the $\Delta : 9/2^-$ pole is deemed unreliable, as detailed in [95]. To enhance clarity, the poles are slightly offset from their precise $\Re[J] = J_p$ positions. Figure adapted from [95].

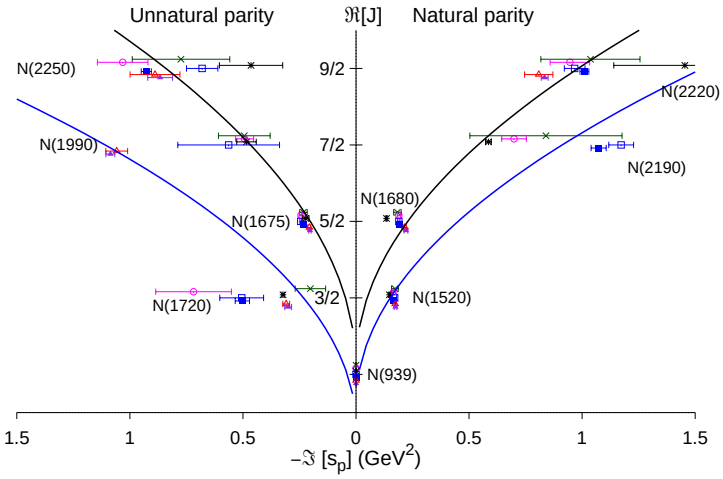

(a) N^* resonances.

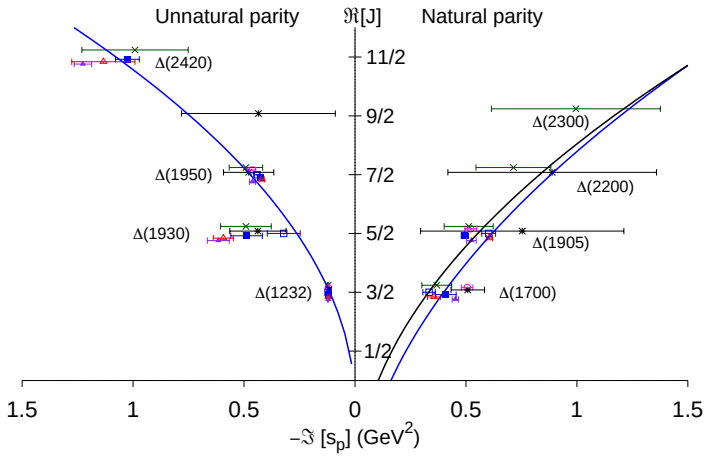

(b) Δ^* resonances.

Figure F.3.2: Plots of $(\Im[s_p], \Re[J] = J_p)$, as introduced in [102], for the leading N^* and Δ^* Regge trajectories presented in [95]. Solid black (blue) curves represent square-root fits ($J_p = c + d \times \sqrt{-\Im[s_p]}$) to the displayed positive (negative) signature data points. A fit for the $\frac{3}{2}^+_{(+)}$ states is omitted due to the unreliability of the $\Delta 9/2^-$ pole, as discussed in [95]. The pole sets are labeled as in Figure F.3.1. To enhance readability, the poles are slightly offset from their exact $\Re[J] = J_p$ values, as in Figure F.3.1. Additionally, the SAID(ED) Δ $9/2^-$ pole, part of the unnatural parity trajectory, has an exceptionally large $\Im[s_p]$ value and is omitted from plot (b). Figure adapted from [95].

The two figures give a qualitative display of the resonance spectrum. The spectrum reveals an approximate linear behavior in $(\Re[s_p], J_p)$ and a square root-like behavior in $(\Im[s_p], J_p)$, similar patterns were seen previously in the hyperon spectrum [102]. It is important to note that the fits presented in Figures F.3.1 and F.3.2 for $(\Re[s_p], J_p)$ and $(\Im[s_p], J_p)$ respectively were performed independently. These fits are exploratory in nature, as emphasized in the introduction of this work. As emphasized, Regge trajectories are typically intricate functions that translate the complex energy plane (s-plane) to the complex angular momentum plane (ℓ-plane). Consequently, these graphs should be interpreted as initial estimations rather than conclusive evaluations.

In order to carry out a quantitative analysis of Regge trajectories, one has to adopt a model in which the real and imaginary parts of the pole positions are introduced simultaneously. This ensures the underlying dynamics is better described and reduces the potential bias due to the isolated or piecemeal analysis of these quantities. Besides the fitting of pole data, the analysis can be complemented by studying other relations present in two-dimensional plots. As an example, the relation found between $\Im(s_p)$ and $\Re(J) = J_p$ provides important information about the dependence of the imaginary part of the pole on spin, as discussed in [102]. In a similar way, one can make use of surface plots of $\Re(\alpha(s))$ over the complex variable s in order to give a more complete characterization of the Regge trajectory. This approach is implemented in the analysis presented below.

We base our analysis on the working hypothesis that the square-root-like behavior observed in figure F.3.2 corresponds to the leading singularity of the Regge trajectories due to unitarity [140]. This ensues because the dominant two-body decay channels, which contribute most significantly to the cross section, produce an imaginary part proportional to the relative momentum $q \sim \sqrt{s - s_t}$, where s is the two-body squared invariant mass and s_t is the threshold. Observe that contributions from multi-body final states can be effectively included in model parameters [95].

The Regge trajectory can be parameterized in a general form as follows [95, 102, 141, 142]:

$$\alpha(s) = \alpha_0 + \alpha' s + i\,\gamma\,\phi(s, s_t)\,, \tag{3.6}$$

where α_0, α' and γ are real constants, and $\phi(s, s_t)$ encapsulates the contributions related to resonance decay. The slope α' is frequently linked to the tension of the

confining string in flux tube models [143–145] and to the range of the strong interaction in Veneziano models [146]. The figure F.3.2 reveals a square-root-like behavior suggesting that the term $\rho(s, s_t)$ is the dominant component of $\phi(s, s_t)$. However, the position of poles in the complex plane depends on two factors: the phase-space structure and the intrinsic dynamics of QCD. Both aspects jointly influence the functional form of $\phi(s, s_t)$. In this context, $\phi(s, s_t)$ explicitly incorporates the phase-space contribution to the pole positions, ensuring that any discrepancies in the overall form of the Regge trajectory can be attributed to additional effects arising from QCD dynamics. However, it is necessary to account for systematic uncertainties arising from the phase-space factor, particularly when describing regions far from the threshold. These uncertainties can be systematically studied by employing different models for $\phi(s, s_t)$. In particular we use (see [95]):

$$i\,\phi_0(s, s_t) = 0\,, \tag{3.7a}$$

$$i\,\phi_{\mathrm{I}}(s, s_t) = i\,\sqrt{s - s_t}\,, \tag{3.7b}$$

$$i\,\phi_{\mathrm{II}}(s, s_t) = i\beta(s, s_t) + 2i\tau(s, s_t), \tag{3.7c}$$

where:

$$i\beta(s, s_t) = \frac{s - s_t}{\pi} \int_{s_t}^{\infty} \frac{\tau(s', s_t)}{s' - s_t} \frac{ds'}{s' - s} = \frac{2}{\pi} \frac{s - s_t}{\sqrt{s(s_t - s)}} \arctan \sqrt{\frac{s}{s_t - s}}\,, \tag{3.8}$$

is the analytic continuation of the two-body phase space.

We propose that the nature of resonances can be understood through their relationship to Regge trajectories. Specifically, a resonance that aligns with a linear trajectory on the Chew–Frautschi plot *and* exhibits a square-root-like pattern in the $(\Im\,[s_p]\,, J_p)$ plot would be mostly a compact $3q$ state candidate. In this scenario, the majority of the state's width, represented by $\phi(s, s_t)$, would primarily comes from phase-space contributions. To reinforce this hypothesis we propose a more quantitative way of matching the resonance poles to the models described by Eq. (3.7). Assuming these states correspond to compact $3q - 3q$, their poles should agree approximately with our prediction from Regge trajectory. Such kind of an agreement would imply that indeed phase-space effects mainly fix the extent to which the poles extend into the complex plane, and only smaller contribution comes from the additional dynamics of QCD. Large deviations of the model would indicate

the involvement of more complex QCD behavior in the resonance. Such results would give clear indication that the state cannot be described by the simple picture of a compact three-quark structure and point to other physical phenomena at work.

The structure of our quantitative analysis is methodically defined as follows. First, we fit the poles of a given trajectory to theoretical models, ensuring the inclusion of both linear and square-root-like behavior that allows for an approximate but sufficiently good description on average. It is important to emphasize that the Regge trajectory model only contains the *phase space* contribution, which inherently renders the framework incomplete. As a consequence, discrepancies between the theoretical models and the empirical data point to the existence of extra QCD dynamics that go beyond the present model's formulation. These discrepancies are hypothesized to represent novel physics extending beyond the conventional $3q$ picture, and give insight into the physical processes that have not been accounted for in the present trajectory formulation.

To determine the values of the model parameters α_0, α', γ and s_t in Eq. (3.6) for a given pole extraction, we employ the least-squares method. This approach minimizes the squared distanced d^2 between the trajectory $\alpha(s)$, evaluated at the complex pole position s_p and the angular momenta J [95]:

$$d^2 = \sum_{poles} \{ \, [\, \Re[J] - \Re[\alpha(s_p)] \,]^2 + [\Im[J] - \Im[\alpha(s_p)] \,]^2 \, \} \, . \tag{3.9}$$

with $\Re[J] = J_p$ and $\Im[J] = \Im[J_p] = 0$ for the resonance poles. The value of the parameter s_t must align with its interpretation as an effective threshold in the resonance region. This serves as a criterion for selecting the physically meaningful minimum when multiple local minima appear during the fits. We estimate the errors in the parameters through the bootstrap technique [108, 115, 147]. It is important to emphasize that this represents a case of a modified bootstrap, as described in section 2.6.1. In this particular scenario, the independent variable carries the uncertainty, while the dependent variable is fixed due to the physical constraints that define a specific, definite value of J for each resonance. Specifically, we perform 10^4 fits to pseudodata generated based on the uncertainties of the pole positions. The expected value of each parameter is computed as the mean of the 10^4 samples and the uncertainty is given by the standard deviation. This method is described in detail

in [95, 102, 148] and allows to propagate the uncertainties from the poles to the parameters accounting for all the correlations. However, systematic errors related to model dependencies in the amplitude analyses are not explicitly included in the pole extractions. To gauge these uncertainties, we compare the differences among models and treat them as indicative of potential systematic effects. See [95] for details.

The evaluation of fitted Regge trajectories in relation to resonances at their pole positions, denoted as s_p, entails rigorous consistency checks as elaborated in [102]. This process involves a comparative analysis of $\alpha(s)$ with the spin values J_p associated with the poles. Once the fitting parameters are determined, they are utilized to compute trajectory values at these pole positions. For a resonance characterized by a pole s_p and spin J_p, the anticipated outcomes are $\Re[\alpha(s_p)] = \Re[J] = J_p$ and $\Im[\alpha(s_p)] = \Im[J] = \Im[J_p] = 0$, with the latter condition representing a fundamental physical constraint. This procedure provides a direct comparison between $\alpha(s)$ (both real and imaginary parts) and the poles, offering a more precise visual appraisal of the fit's accuracy by juxtaposing the fitted curve with the pole values of the angular momentum J_p. The condition $\Im\left[\alpha(s_p)\right] = 0$ represents a particularly stringent criterion since is a physical restriction, so, deviations from this condition can be interpreted as we discuss before. Furthermore, the consistency check plot serves as the appropriate figure for visually comparing the outcomes of the fit with the pole positions. However, for trajectories containing only two poles, these checks provide no meaningful insight due to overfitting, as four experimental points (two masses and two widths) are matched using four parameters. Consequently, consistency checks are restricted to trajectories involving more than two poles. The uncertainties in both the pole positions and the parameters are propagated through the calculation of $\alpha(s)$, ensuring that the results accurately reflect the physical differences (see [95]).

In Figures F.3.3(a) and F.3.3(b), we present the consistency checks for the trajectories $I^{\eta}_{(\tau)} = I = \frac{1}{2}^{+}_{(+)}$ and $I^{\eta}_{(\tau)} = I = \frac{3}{2}^{-}_{(-)}$, respectively. The comprehensive results for each analyzed Regge trajectory are detailed in [95]. While these findings substantiate the qualitative conclusions, they also reveal significant physical phenomena beyond the compact $3q$ (three-quark) framework, particularly for the $N(1680)$, $N(1720)$, and certain members of the $\frac{3}{2}^{-}_{(-)}$ trajectory. The accuracy of the pole positions for these states is sufficient to make our analysis sensitive to effects

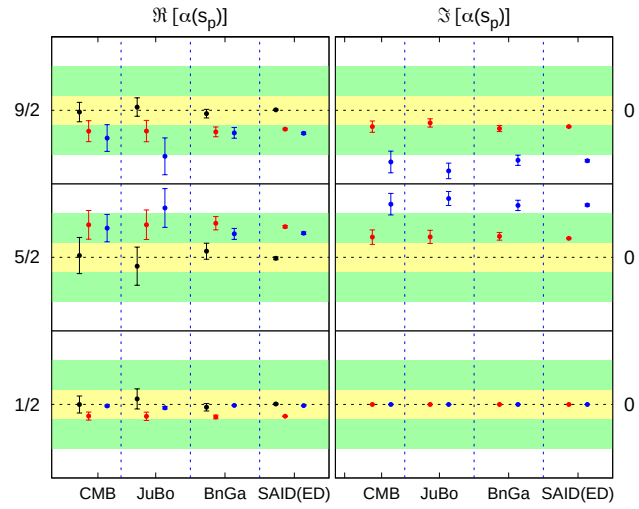

(a)

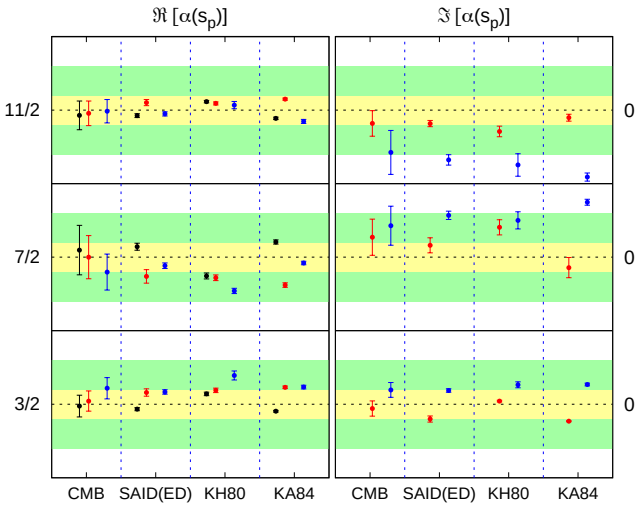

(b)

Figure F.3.3: (a) Consistency checks plots for the $I^{\eta}_{(\tau)} = \frac{1}{2}^{+}_{(+)}$ poles, stemming from extractions from CMB, JüBo, BnGa, and SAID(ED). The left panel shows $\Re[\alpha(s_p)]$, evaluated at the resonance poles (s_p) for models 0 (black), I (red), and II (blue). Ideally, these should fall on the corresponding angular momentum $\Re[J] = J_p$ (vertical axis) for each resonance. The right panel shows the results for $\Im[\alpha(s_p)]$, which are expected to fulfill the condition $\Im[J] = \Im[J_p] = 0$. For this analysis, model 0 is not shown in the right panel as $\Im[\alpha(s_p)]$ is defined to be 0. The yellow band represents deviations up to 0.1, while the green band represents deviations between 0.1 and 0.3. The white band corresponds to deviations ranging from 0.3 to 0.5. (b) Consistency checks for the $I^{\eta}_{(\tau)} = \frac{3}{2}^{-}_{(-)}$ poles, obtained from CMB, SAID(ED), KH80, and KA84 extractions. The notation is the same as in Fig. F.3.3(a). This figure is reproduced from [95].

extending beyond the compact $3q$ picture.

The results presented shows a strong breaking of exchange degeneracy for the nonstrange sector, while in the strange sector, this degeneracy seems to be preserved. Such a breaking demonstrates the crucial role played by the exchange forces in the determination of the low-lying nonstrange baryon spectrum. Furthermore, we see that the $\frac{1}{2}^-$ and $\frac{3}{2}^+$ trajectories are badly parameterized, restricting the information that Regge phenomenology can supply on the inner structure of the baryons on these trajectories. Nonetheless, Regge phenomenology is still an indispensable tool, mainly for conducting resonance searches. It provides the basis to investigate whether the fits of the experimental data could be ameliorated by adding the resonances in the vicinities of expected positions predicted by Chew–Frautschi plots and $(\Im[s_p], J_p)$ representations. The presented procedure outlines possible areas where so-far-unknown resonances might exist and supports the systematic description of the baryon spectra and dynamics. The outlined procedure highlights regions where previously undetected resonances may exist, contributing to a systematic and comprehensive description of the baryon spectra and their underlying dynamics.

The parameters of the $\frac{1}{2}^+_{(+)}$ (nucleon) and $\frac{3}{2}^-_{(-)}$ (Δ) Regge trajectories are determined with high precision from the pole extractions. For the nucleon trajectory, we estimate a slope of $\alpha' = 0.99 \pm 0.12$ GeV^{-2}, while for the Δ trajectory, the slope is $\alpha' = 1.21 \pm 0.15$ GeV^{-2}. Notably, the slopes of these trajectories are compatible within their respective uncertainties. This range of α' values aligns with those derived from fits to Chew–Frautschi plots, predictions of constituent quark models, and analyses of high-energy proton-antiproton annihilation data [149]. These consistent results further validate the theoretical framework and its applicability to describing baryon dynamics and resonance structure.

The origin of Figures F.3.1 and F.3.2 is revealed by a study of the surface plot of $\Re[\alpha(s)]$ versus the complex variable s depicted in Figure F.3.4. This three dimensional plot gives an intuitive understanding of the behavior of the Regge trajectory as the complex s plane, , illustrating the underlying structure that gives rise to the patterns observed in the earlier plots. In this plot a resonance is represented as a point in the space $(\Re[s], \Im[s], \Re[J])$. The plots F.3.1 and F.3.2 are then the projections in the planes $(\Re[s], \Re[J])$ and $(\Im[s], \Re[J])$, respectively. Since in the poles $\Im[\alpha(s_p)]$ is zero,

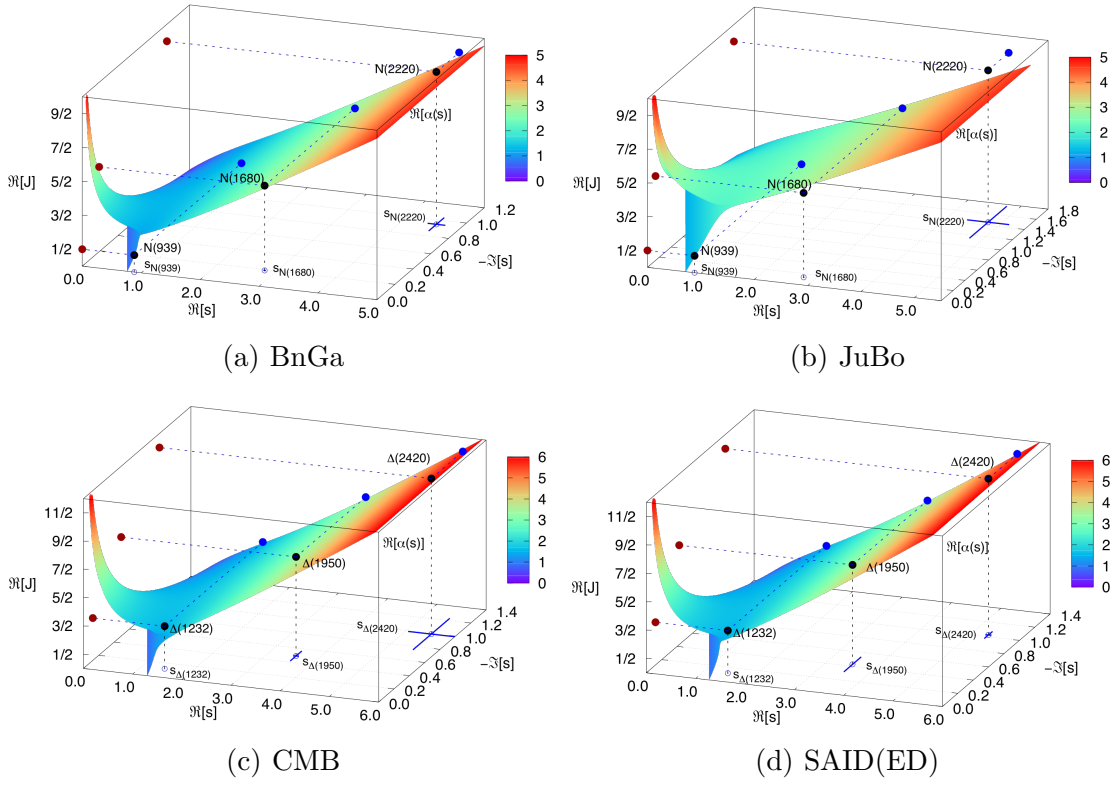

(a) BnGa (b) JuBo

(c) CMB (d) SAID(ED)

Figure F.3.4: The Regge trajectory is a complex function here we show the $\Re[\alpha(s)]$ adjusted to the trajectory $\frac{1}{2}^+_{(+)}$ the pole extractions of BnGa (a), JüBo (b), CMB (c) and SAID(ED) (d) for the model II. The black points are the position of the resonance in the space $(\Re[s], \Im[s], \Re[J])$. The blue circles are the position of the poles with uncertainties, and the blue and red points are the projection of the resonances positions (black points) in the planes $(\Re[s], \Re[J])$ and $(\Im[s], \Re[J])$, i.e. the Chew–Frautschi and the $(\Im[s], \Re[J])$ plots.

the surface plot of $\Im[\alpha(s)]$ as a function of complex s is a flat surface that does not provides any further information.

3.2 Study of the $P_c(4312)^+$ signal

In section 1, we briefly introduced the minimal quark model, its benefits, and extensions beyond the $q\bar{q}$ and qqq ($\bar{q}\bar{q}\bar{q}$) pictures for mesons and baryons, respectively. One of the most prominent exotic states that has been discovered

recently is the $P_c(4312)^+$, whose valence quark content is $uudc\bar{c}$, and hence is a hidden-charm pentaquark. This state, discovered by LHCb [19] in the $J/\psi\, p$ subchannel of the $\Lambda_b^0 \to J/\psi p K^-$, sits just 5 MeV below the $\Sigma_c^+ \bar{D}^0$ threshold, making it a prime candidate for a meson-baryon molecular state generated by the opening of the $\Sigma_c^+ \bar{D}^0$ channel. Molecular hidden-charm pentaquarks were postulated [150–154] prior to their discovery by LHCb [155] and their spectrum can be a test of the predictions from heavy-quark spin symmetry [154, 156–158].

There are several interpretations of this signal. The most popular is the $\Sigma_c^+ - \bar{D}^0$ molecule interpretation mentioned above, bound [150–154, 159–162] or virtual [88], but neither the compact [163–166] nor the double triangle [167] interpretations cannot be ruled out. The single-triangle interpretation was ruled out by the LHCb collaboration [19] as the intermediate states needed to have for the singularity to show up with the necessary strength do not exist.

In this section we present the analysis of the $P_c(4312)^+$ signal using the near-threshold theory presented in section 2.4. We perform an amplitude analysis of the signal and extract the pole position and its uncertainties. Additionally, albeit model dependent, we provide an explanation of the nature of the resonance. Before detailing the amplitude analysis, we dive into the experimental data that will be used.

3.2.1 LHCb datasets for the $J/\psi p$ subchannel

The existence of the $P_c(4312)^+$ was sustained at a 7.3σ confidence level, employing three datasets of the $J/\psi p K^-$ subchannel from the collected $\Lambda_b^0 \to J/\psi p K^-$ decay events at LHCb [19]: the inclusive, the $\cos\theta_{P_c}$-weighted, and the $m_{K_p} > 1.9$ GeV datasets. Before analyzing the $P_c(4312)^+$ signal we provide the details on the three dataset, as all of them will be studied in our amplitude analysis.

1. **The inclusive dataset.** The inclusive dataset provides the most complete and widest view of the $J/\psi p$ subchannel; it's unfiltered, showing the distribution of the $J/\psi\, p$ invariant mass. This dataset comprises inputs for all possible processes in the decaying phase space and includes signal components from the P_c^+ resonances, along with various distinct background sources. These consist

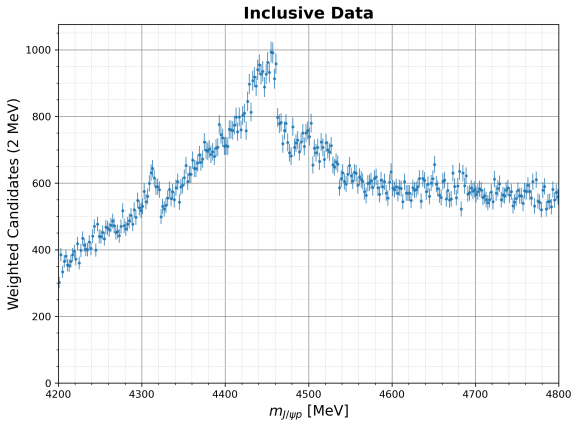

(a)

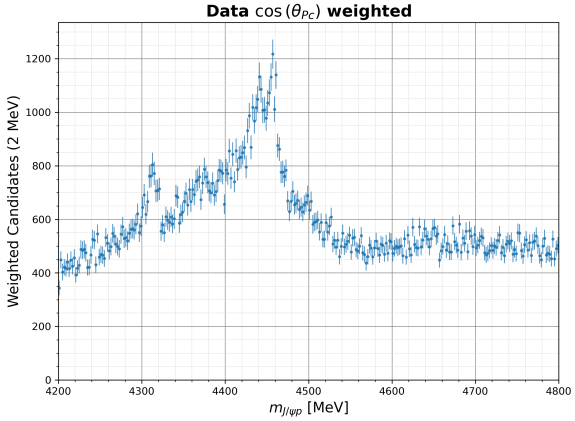

(b)

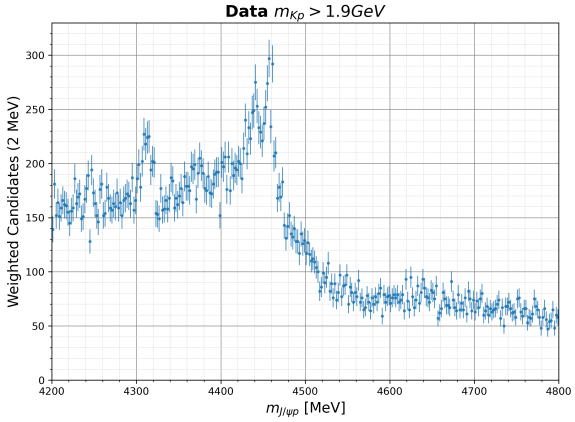

(c)

Figure F.3.5: The three datasets for the $J/\psi p$ subchannel reported by LHCb in [19]. (a) corresponds to the inclusive dataset, (b) to the $\cos\theta_{Pc}$ weighted dataset and (c) to the $m_{Kp} > 1.9GeV$.

of reflections from $\Lambda^* \to pK^-$ states, non-Λ_b^0 backgrounds, and possible broad resonances that smoothly vary with respect to $m_{J/\psi p}$. While the coexistence of these intertwined elements poses some challenges, the whole dataset is an essential foundation for confirming the existence of the resonance and opens the way to analyze further with appropriate selection criteria. The inclusive dataset is remarkable in that it contains more than $246,000$ reconstructed $\Lambda_b^0 \to J/\psi p K^-$ decays, which represents a ninefold increase in size with respect to the previously published LHCb dataset [155].

These improvement in statistical measures in [19] significantly enhance the potential to recognize more subtle structures in the $J/\psi\, p$ invariant mass spectrum and to distinguish features that were previously not resolvable. The inclusiveness of the dataset ensures a full representation of the whole decay dynamics of the Λ_b^0, which—on the other hand—requires state-of-the-art analytical techniques in order to extract the P_c^+ resonances from the dominant background contributions. The $P_c(4312)^+$ resonance is seen in this data sample as a distinct peak whose width, measured to be 9.8 MeV, is consistent with the experimental resolution in the J/ψ invariant mass region. This peak is overlaid by a complex background that is affected by $\Lambda^* \to pK^-$ reflections, which produce a structured but smooth contribution. These reflections are in the regions of small m_{Kp} in the Dalitz plot and are spread broadly over the $m_{J/\psi p}$ spectrum. The analysis takes advantage of the smooth variation of these backgrounds as a function of $m_{J/\psi p}$, contrasting with the distinctive signature of the $P_c(4312)^+$. A binned χ^2 fit to the $m_{J/\psi p}$ distribution is used to extract the properties of the $P_c(4312)^+$, described by a sum of relativistic Breit-Wigner terms for narrow P_c^+ (see [19]) resonances and a parameterized smooth background. The latter includes detector effects, such as resolution and efficiency, in order to obtain unbiased resonance parameters. In the whole dataset, the $P_c(4312)^+$ signal is observed with a statistical significance of 7.3σ, thereby confirming that the resonance is indeed a real physical entity and not an artifact because of background fluctuations.

2. **The $\cos\theta_{P_c}$-weighted dataset.** The $\cos\theta_{P_c}$-weighted dataset represents a more refined and targeted methodology in the study of the $P_c(4312)^+$ resonance, which improves the signal-to-background ratio by exploiting angular correlations inherent in the decay dynamics. The core of this methodology is

the helicity angle θ_{P_c}, defined as the angle between the K^- meson and the J/ψ in the rest frame of the candidate P_c^+. This angle is highly important for the study of the spin-parity structure of intermediate resonances and also serves as a very powerful tool in distinguishing signal from background components.

In decays $\Lambda_b^0 \to J/\psi p K^-$, the dominant background arises from $\Lambda^* \to pK^-$ reflections, which are confined to certain angular regions, mostly in the $\cos\theta_{P_c} > 0$ domain due to their kinematic and dynamical properties. The converse is true for isotropic decays of narrow P_c states, such as the $P_c(4312)^+$: they distribute more uniformly across $\cos\theta_{Pc}$. To take advantage of this contrast, a weighting function $w(\cos\theta_{Pc})$ is implemented, which is calculated as being inversely proportional to the background density in the $\cos\theta_{Pc}$ distribution. This weighting enhances P_c signal contributions while suppressing Λ^* induced background effects. A key component of this analysis is the construction of the weighting function $w(\cos\theta_{Pc})$. Obtained directly from data, it takes as input the observed density of candidates in the $\cos\theta_{Pc}$) distribution as a proxy for the background, assuming negligible signal. This procedure suppresses background-dominated regions and enhances those with a larger signal-to-background ratio, thus optimizing the dataset for the study of the $m_{J/\psi p}$ invariant mass spectrum.

The cosine weighting of the dataset shows the $P_c(4312)^+$ resonance in much clearer detail and with much greater statistical significance, 8.2σ, than that in the inclusive dataset. The mass and width of $P_c(4312)^+$ are in good agreement with those in other datasets, demonstrating the stability of this method used in [19]. The weighted dataset also reduces the systematic biases induced by Λ^*-induced background fluctuations, providing cleaner and more precise measurements of resonance parameters. The $\cos\theta_{P_c}$-weighted dataset is also able to provide insight into the interfering amplitudes that much more nuanced. While the analysis models P_c^+ contributions primarily as incoherent relativistic Breit–Wigner terms in [19], this dataset is sensitive to potential interference effects between resonances or between the signal and background. Such sensitivity allows for the estimation of systematic uncertainties associated with interference the analysis of the signals. The cosine weighting of the dataset significantly amplifies the experimental sensitivity of the narrow P_c^+ states due to its emphasis on angular features of the decay. Since this is confirmation not

only of the existence but also the independence of $P_c(4312)^+$ from background-induced artifacts, these results highlight the effectiveness of using angular information in resonance analysis and justify applying such methods in the wide study of exotic hadronic states.

3. **The $m_{Kp} > 1.9\,\text{GeV}$ dataset.** This third dataset is a significant refinement in the analysis of the $P_c(4312)^+$ resonance with the use of a selection criterion that suppresses one of the most dominant sources of background: the $\Lambda^* \to pK^-$ reflections onto the $J/\psi p$ subchannel. These reflections, resulting from a variety of excited Λ^* states populate predominantly the low K^-p invariant mass region and give a structured but broad contribution to the$m_{J/\psi p}$ spectrum. By imposing a lower bound of 1.9 GeV on m_{Kp}, the analysis effectively removes more than 80% of these contributions, yielding a much cleaner dataset for studies of P_c^+ resonances. This selection criterion exploits the Dalitz plot structure of the $\Lambda_b^0 \to J/\psi p K^-$ decay: the K^-p and $J/\psi p$ invariant masses are correlated through the three-body decay kinematics. The $\Lambda^* \to pK^-$ contributions are dominant in regions of low, particularly below, as evidenced by the dense vertical bands in the Dalitz plot. Cuts on the region, thus isolate, which exhibit as horizontal bands associated with, $P_c(4312)^+$, $P_c(4440)^+$, and $P_c(4457)^+$ and resonances. This separation of the invariant mass features in the $J/\psi p$ is clearer for the $m_{Kp} > 1.9\,\text{GeV}$ dataset, where these overlapping Λ^* reflections are suppressed.

   The resulting $m_{J/\psi p}$ spectrum includes a striking enhancement of the narrow peak of the $P_c(4312)^+$ relative to a smoother and significantly reduced background. The latter reduction allows a substantially more precise measurement of the properties of this resonance, as systematic biases related to Λ^*-dominated backgrounds are drastically reduced. In this dataset, the $P_c(4312)^+$ is observed with a statistical significance of 7.6σ, further confirming its existence with high confidence. The extracted mass and width of the resonance are also in good agreement with those obtained from inclusive as well as $\cos\theta_{P_c}$-weighted datasets, which reassures the consistency and reliability among the results from different methods. The threshold choice at $m_{Kp} > 1.9$ is not arbitrary but relies on a detailed analysis of the background composition and expected signal significance. A decrease in the threshold would add back a large fraction of the Λ^*-induced background, making it hard to isolate the signals for P_c^+. While a high cut on t is effective for background rejection,

excessively increasing it loses much statistics for the study of P_c^+, probably resulting in a loss of statistical power for the measurement. A cutoff of 1.9 GeV offers the best compromise for maximum background suppression while retaining an ample dataset that is statistically significant for the resonance analysis. Besides background suppression, the criterion of $m_{Kp} > 1.9\,\text{GeV}$ provides an indirect probe of the interplay between the contributions from $\Lambda^* \to pK^-$ and $P_c^+ \to J/\psi p$. But instead, this dataset allows the study of possible interference effects between these components in a cleaner way, shedding light on the dynamics of the decay process, by removing the dominant Λ^* region. Although the analysis assumes an incoherent sum of relativistic Breit–Wigner amplitudes for the P_c^+ states, the suppression of Λ^*-induced interference ensures that the parameters extracted for the $P_c(4312)^+$ suffer the least from such effects. This makes the $m_{Kp} > 1.9\,\text{GeV}$ dataset one that plays a great role in the study and analysis of the $P_c(4312)^+$ resonance. This will supplement the inclusive and $\cos\theta_{P_c}$-weighted datasets, providing a cleaner environment in which to study the $J/\psi p$ invariant mass features and thereby offering a key cross-check of the properties of this resonance.

The consistency of the $P_c(4312)^+$ signal across all datasets reinforces its interpretation as a genuine physical state.

3.2.2 Near-threshold amplitude analysis

We employ a coupled-channel amplitude formalism involving the $J/\psi p$ and $\Sigma_c^+ \bar{D}^0$ channels to conduct a detailed analysis of the $J/\psi p$ subchannel spectrum arising from the $\Lambda_b^0 \to J/\psi p K^-$ decay, as measured by the LHCb collaboration. Our investigation focuses on the energy region between 4250 and 4380 MeV, where the presence of the $P_c(4312)^+$ signal has been experimentally observed. In this analysis, we assume that the $P_c(4312)^+$ signal is characterized by a precise and specific spin quantum number, which restricts its contribution to a single partial wave, denoted as $F(s)$. To account for other effects, we also include background contributions, $B(s)$, which arise from additional partial waves and remote singularities. These background contributions are modeled incoherently and represented as a linear polynomial of the form $B(s) = b_0 +$

$b_1 s$, where b_0 and b_1 are parameters to be determined. [1] Therefore, the distribution of events is expressed as [168, 169]:

$$\frac{dN}{d\sqrt{s}} = \rho(s)\left[|F(s)|^2 + B(s)\right] = \rho(s)\left[|P_1(s)T_{11}(s)|^2 + b_0 + b_1 s\right], \tag{3.10}$$

with $\rho(s)$ is the phase space factor of the decay $\Lambda_b^0 \to J/\psi\, p\, K^-$, given by $\rho(s) = m_{\Lambda_b} p\, q$ with $p = \lambda^{1/2}(s, m_{\Lambda_b}^2, m_K^2)/2m_{\Lambda_b}$ and $q = \lambda^{1/2}(s, m_p^2, m_\psi^2)/2\sqrt{s}$. $P_1(s)$ accounts for the Λ_b^0 decay and the $J/\psi\, p\, K^-$ production. It also takes into account the effects of other signals projected onto the same partial wave of the $P_c(4312)^+$ (for example, the Λ^* contributions from the $K^- p$ subchannel). The function $P_1(s)$ is analytic within the examined region and, due to the limited mass range under consideration, it can be expressed as a first-order polynomial, say, $P_1(s) = p_0 + p_1 s$. This formulation assumes that the resonance manifests in the S-wave. This is actually a good approximation even if the signal is on another partial wave. Going beyond the S wave multiplying the amplitude $F(s)$ q^ℓ term, which in practice remains constant because q varies slowly within the considered energy range. The $T_{11}(s)$ amplitude describes the $J/\psi\, p \to J/\psi\, p$ subchannel, where the $P_c(4312)^+$ is found.

Near the $\Sigma_c^+ \bar{D}^0$ threshold the two coupled-channels T matrix in the scattering length approximation can be written as it was shown in section 2.4:

$$T_{11}(s) = \frac{\mu_{22}(s) - ik_2}{[\mu_{11}(s) - ik_1]\,[\mu_{22}(s) - ik_2] - \mu_{12}^2(s)}, \tag{3.11a}$$

$$T_{12}(s) = \frac{-\mu_{12}(s)}{[\mu_{11}(s) - ik_1]\,[\mu_{22}(s) - ik_2] - \mu_{12}^2}, \tag{3.11b}$$

$$T_{22}(s) = \frac{\mu_{11}(s) - ik_1}{[\mu_{11}(s) - ik_1]\,[\mu_{22}(s) - ik_2] - \mu_{12}^2(s)}, \tag{3.11c}$$

Here, k_i is defined as $\sqrt{s - s_i}$, with $s_1 = (m_p + m_\psi)^2$ and $s_2 = (m_{\bar{D}^0} + m_{\Sigma_c^+})^2$, which correspond to the threshold values for the respective channels. The functions $\mu_{11}(s)$,

[1] An analytical function can, in a formal sense, be expressed as a Laurent series expansion around a singularity located at $z = z_0$, as outlined in [63]: $F(z) = \frac{R}{z - z_0} + a_0 + a_1 z + a_2 z_2 + \cdots$, where R denotes the residue of the pole at $z = z_0$, and c_i represent the coefficients of the polynomial terms in the series. At sufficiently large distances from the singularity, the contributions from the polynomial terms $a_0 + a_1 z + a_2 z^2 + \cdots$ become dominant, effectively diminishing the impact of the singular term $\frac{R}{z - z_0}$ on the overall behavior of the function.

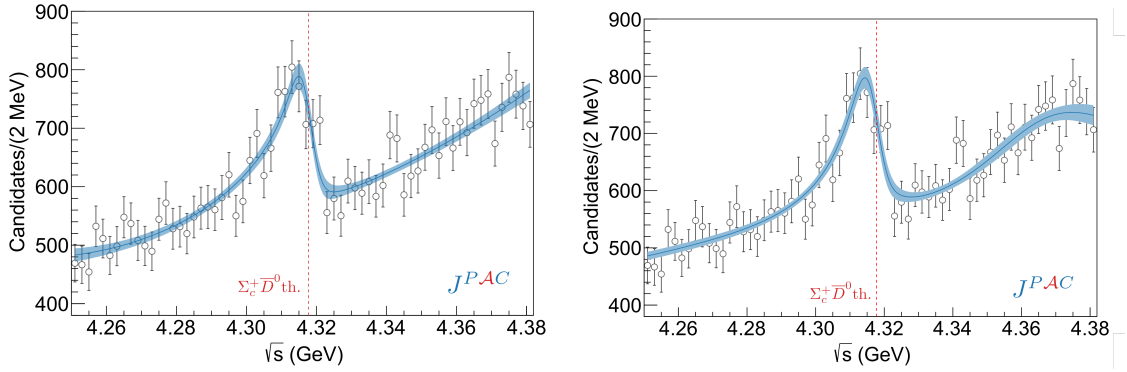

Figure F.3.6: Fits to the $\cos\theta_{P_c}$-weighted $J/\psi p$ mass distribution measured by LHCb [19], shown for cases A (left) and B (right). For case A, the amplitude is modeled using the scattering length approximation, where $c_{ij} = 0$ in Eq. (2.68), enabling the description of either molecular (bound) states or virtual states. In contrast, case B employs the effective range approximation, characterized by finite c_{ii} values, which expands the interpretation to include genuine pentaquark states. The solid curve represents the best-fit result, while the blue band illustrates the one sigma (1σ) confidence interval derived from a bootstrap analysis. Figures adapted from [169].

$\mu_{22}(s)$, and $\mu_{12}(s)$ are expressed in Equation (2.68). The term $T_{11}(s)$ corresponds to the process $J/\psi p \to J/\psi p$, while $T_{22}(s)$ describes the process $\Sigma_c^+\bar{D}^0 \to \Sigma_c^+\bar{D}^0$; in contrast, the off-diagonal elements $T_{12}(s)$ and $T_{21}(s)$ describe the transitions $J/\psi p \to \Sigma_c^+\bar{D}^0$ and $\Sigma_c^+\bar{D}^0 \to J/\psi p$, respectively. The parameters in the expressions for $\mu_{ij}(s)$ play an important role in fixing the location of the pole. It should be stressed that, since the other thresholds and singularities are far away from the region of interest, their influence can safely be absorbed in the amplitude parameters. While it is formally justified to include the off-diagonal term $P_2(s)T_{12}(s)$, dropping it does not alter the analytic properties or the poles of the amplitude. Consequently, this term is neglected to reduce the free parameters number in the model [168, 169].

We analyze the data under both the scattering length (case A) and the effective range (case B) approximations. In the latter we take the expression $\mu_{ij}(s) = M_{ij} + c_{ij}s$ with $c_{12} = 0$, while in the former we fix all $c_{ij} = 0$, i.e. $\mu_{ij}(s) = M_{ij}$. In case A, the amplitude can only have poles on the II and the IV sheets, but not on the I or the III. In case B, we let the diagonal effective ranges c_{ii} float. The off-diagonal c_{12} does not add other singularities and is not needed to

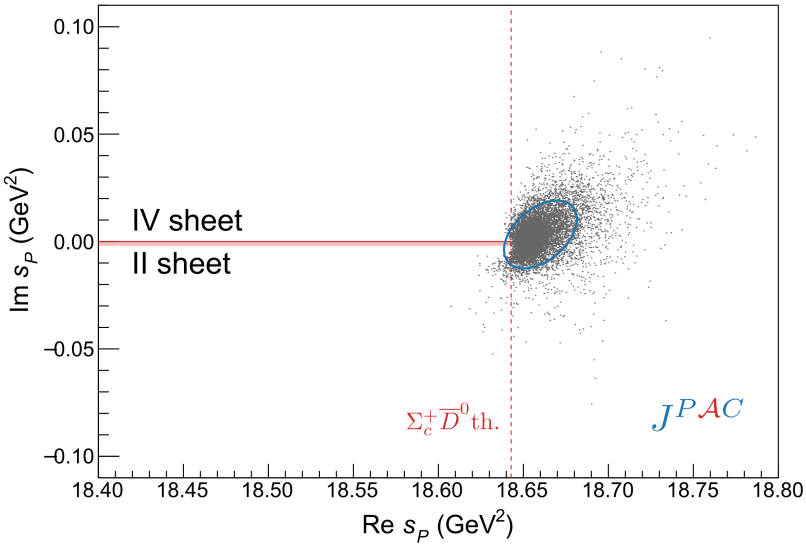

(a)

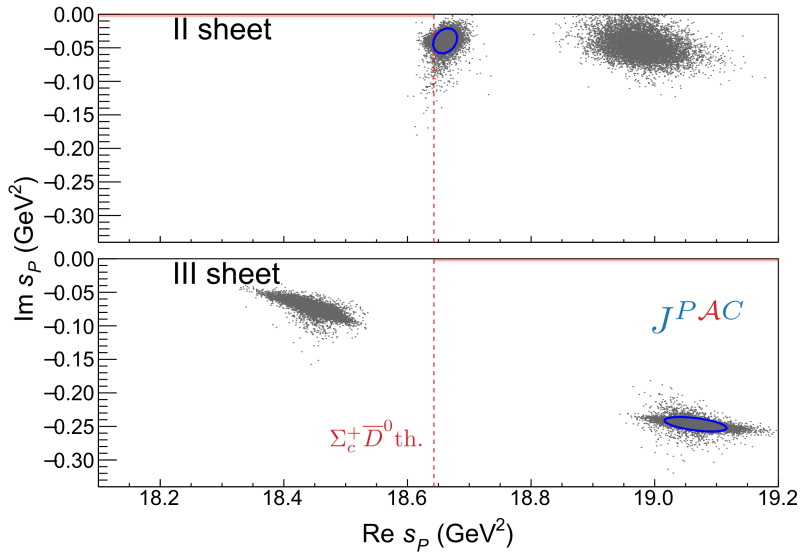

(b)

Figure F.3.7: The poles derived from the 10^4 bootstrap fits are displayed for scenarios A (top) and B (bottom), with the physical region delineated by a pink band. For scenario A, the poles reside on the second and fourth Riemann sheets, which are seamlessly connected above the ΣD threshold. Each bootstrap fit yields a single pole within this region, with the blue ellipse enclosing 68% of the cluster concentrated above the threshold. The plots on the right correspond to scenario B, where each bootstrap fit identifies a pole on the second sheet accompanied by its counterpart on the third sheet. The higher-mass pole on the second sheet, along with its partner on the third sheet, lies beyond the fitted energy spectrum, attempting to encapsulate the bump-like feature observed near 4370 MeV. Conversely, the lower-mass pole on the second sheet and its counterpart on the third sheet are associated with the P_c signal. The blue ellipses indicate the regions containing 68% of both clusters. Figure adapted from Fig. 2 in [168].

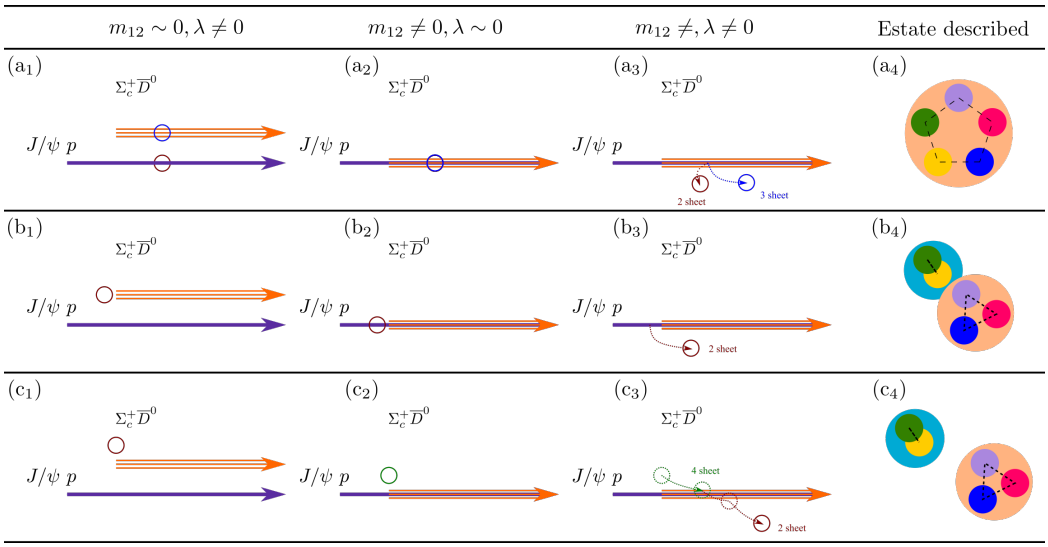

Figure F.3.8: Pole movement for the amplitude described in equations (3.11a), (3.11b) and (3.11c) with $mu_{12}(s) = m_{12}$ and a λ parameter in front of each k_i such that $0 \leq \lambda \leq 1$. The (a_i) row describes a compact pentaquark, the (b_i) a molecular state and the (c_i) one a virtual state. See the text for the discussion and also figure 2 in reference [87].

describe data, so we set it to zero. In this case, poles related to the threshold as the ones just discussed are possible; however, other poles can appear on the I and III sheet. Any fit which contains poles on the I sheet would be discarded.

We fit the $\cos\theta_{P_c}$-weighted spectrum $dN/d\sqrt{s}$ measured in [19], with $\sqrt{s}$ being the $J/\psi\, p$ invariant mass, using MINUIT [110].[2] For particle masses, we use the PDG values $m_{\Sigma_c^+} = 2452.9\,\text{MeV}$ and $m_{\bar{D}^0} = 1864.83\,\text{MeV}$ [8]. Since the width of the Σ_c^+ is smaller than the experimental resolution, its effects can be neglected.

To compare the theory to the experiment it is necessary to take into account the experimental resolution. This is provided by LHCb [19] and reads:

$$R(E_0) = 2.71 - 6.56 \times 10^{-6}(E_0 - 4567)^2, \tag{3.12}$$

where $E_0 = \sqrt{s_0}$ in MeV. Then, to obtain the amplitude at $E \equiv \sqrt{s}$, the theory has

[2] We also analyze the other LHCb datasets reported in [19] which are the full dataset without the $\cos\theta_{P_c^+}$-dependent weights in the region and the one which only considers events with $m_{K_p} > 1.9$ GeV which effectively removes over 80% of the Λ^0 that could interfere with the P_c signal. This selection criterion is essential for isolating the P_c states from background noise. The conclusions are the same as for the $\cos\theta_{P_c}$ datatset.

Table C.3.5: Comprehensive summary of the fit results corresponding to the two scenarios examined in this thesis. All numerical values are expressed with the appropriate implied powers of GeV *units. The χ^2/dof value represents the best-fit solution obtained for each case, providing a quantitative measure of the fit quality. For an in-depth explanation of the methodology and further discussion of the results, refer to [168].*

	Case A		Case B	
χ^2/dof	$48.1/(66-7) = 0.82$		$43.0/(66-9) = 0.75$	
	best fit	bootstrap	best fit	bootstrap
b_0	402.95	446 ± 73	0.74	6.1 ± 6.0
b_1	-15.00	-17.4 ± 4.1	7.22	6.93 ± 0.36
p_0	423.16	437 ± 16	85.06	92.6 ± 8.8
p_1	-23.53	-24.28 ± 0.81	-5.30	-5.70 ± 0.47
m_{11}	2.60	2.65 ± 0.28	151.29	151.35 ± 0.23
m_{22}	0.22	0.223 ± 0.078	38.81	39.12 ± 0.28
m_{12}	0.85	0.86 ± 0.11	1.03	1.035 ± 0.062
m_{23}	0	0	0	0
c_{11}	0	0	8.00	8.007 ± 0.015
c_{22}	0	0	2.06	2.081 ± 0.016
c_{12}	0	0	0	0

to be convoluted with the experimental resolution as follows:

$$\frac{dN(E)}{d\sqrt{s}} = \frac{1}{A_0(E)} \int_{m_\psi + m_p}^{m_{\Lambda_b} - m_K} \frac{dN(E_0)}{dE_0} \exp\left[-\frac{(E-E_0)^2}{2R^2(E)}\right] dE_0, \tag{3.13}$$

and the normalization A_0 is given by:

$$A_0(E) = \int_{m_\psi + m_p}^{m_{\Lambda_b} - m_K} \exp\left[-\frac{(E-E_0)^2}{2R^2(E)}\right] dE_0. \tag{3.14}$$

Table C.3.5 summarizes the results of fits to cases A and B, both of which yield consistent descriptions of the signal. In particular, case A yields a goodness-of-fit of

$\chi^2/\text{dof} \sim 0.82$, and case B $\chi^2/\text{dof} \sim 0.75$. In order to quantify the uncertainties in the parameters and observables, we use the bootstrap procedure outlined in Section 2.6.1. This involves creating 10^4 pseudodata sets from the original data set using Gaussian distributions, resampling, and fitting each of these sets individually. The resultant statistical fluctuations are denoted by the uncertainty bands shown in Figures F.3.6(a) and F.3.6(b). For every bootstrap fit, we also derive the pole positions, and these are displayed in Figures F.3.7(a) and F.3.7(b). Figure F.3.7 shows, as a result of a careful examination, definite pole configurations in the two scenarios under discussion. In scenario A, there is a distinct grouping of poles on the second (II) and fourth (IV) Riemann sheets, above the $\Sigma_c^+ \bar{D}^0$ threshold. They are defined in terms of the usual definitions of the mass and width: $M_P = \Re\sqrt{s_p}$ and $\Gamma_P = -2\Im\sqrt{s_p}$. The parameters of the dominant pole cluster for this solution are found to be $M_P = 4319.7 \pm 1.6$ MeV and $\Gamma_P = -0.8 \pm 2.4$ MeV. Indeed, the sign of the width, Γ_P, plays a crucial role in distinguishing poles on the second sheet, which have a positive width, from those on the fourth sheet with negative width. By contrast, in scenario B, two distinct clusters are observed on the second sheet by the poles. The cluster closest to the $\Sigma_c^+ \bar{D}^0$ threshold is identified with the $P_c(4312)^+$ signal. Fitted parameters for the latter signal are $M_P = 4319.8 \pm 1.5$ MeV and $\Gamma_P = 9.2 \pm 2.9$ MeV. These results highlight the differences between the two scenarios regarding pole distributions and their respective physical interpretations.In both cases, the pole clusters are, on average, located closer to the IV sheet. As discussed in the introduction of this work, poles lying near the physical region may be interpreted directly as resonances (see also discussion in Ref. [21, 170]). The above observation is a first indication that the signal likely originates from a virtual state.

Studying the movement of poles in the complex plane as we vary the parameters of the scattering amplitude provides valuable insights into the nature of resonances. This approach allows us to explore the plausibility of different physical scenarios, such as the emergence of bound states, virtual states, or resonances, depending on how the poles evolve with respect to changes in parameters like energy or coupling constants, for instance. However, this analysis is inherently model-dependent, as it relies on the assumption that one can vary a single parameter while keeping others fixed. Let us put a parameter λ in front of each k_i in (3.11a), (3.11b) and (3.11c), such that $0 \leq \lambda \leq 1$, with the purpose of turning on or off the phase space contribution, and consider the case $\mu_{ij}(s) = m_{ij}$. If $m_{12} = 0$ and $\lambda \neq 0$, we have decoupled the channels and turned

off the phase space, *i.e.* any pole would appear in the real axis. Hence, there are two amplitudes $T_{11}(s)$ and $T_{22}(s)$ that are unconnected. If the $P_c(4312)^+$ were a compact pentaquark there would be two poles, one in each amplitude on top of its respective original cut and at the same mass, as depicted in figure F.3.8.(a_1), for a molecule and a virtual state there is a pole below the $\Sigma_c^+\bar{D}^0$ threshold as in F.3.8.(b_1) and F.3.8.(c_1), but no pole in the $J/\psi\, p$ channel. If we recouple the channels by turning on the m_{12} parameter ($m_{12} \neq 0$), the amplitudes $T_{11}(s)$ and $T_{22}(s)$ are connected, and the $T_{12}(s)$ [$T_{12}(s)$] is different form zero. The compact pentaquark interpretation is depicted in figure F.3.8.(a_2). In the molecular interpretation, the pole that was in the real axis of the I Riemann sheet below the $\Sigma_c^+\bar{D}^0$ threshold now appears in the real axis of the II Riemann sheet (as a consequence of coupling the channels, we move from two unconnected Riemann sheets for each channel to four connected Riemann Sheets relating both channels) as shown in F.3.8.(b_2). For the virtual state case, the pole was in the real axis of the II Riemann sheet below the $\Sigma_c^+\bar{D}^0$ threshold, and once we couple the channels, it appears in the real axis, at the same energy, but in the IV Riemann Sheet F.3.8.(c_2). Once the channels are coupled ($m_{12} \neq 0$), we can turn on the phase space, and slowly increment the value of λ from zero to one. In the compact pentaquark picture, the two overlapped poles move to the second and third sheet, depending on their original channel, as in F.3.8.(a_3). For the molecular interpretation, the pole moves to the II sheet F.3.8.(b_3) and, for the virtual one, the pole makes a transition from the fourth to the second Riemann sheet F.3.8.(c_3). See also figure 2 in reference [87] as well as the animations in the supplemental material of Ref. [88].

In the current study, the parameters' values are determined by fitting them to the empirical data, enabling an exploration of the phenomenon known as "pole movement" by systematically switching off the parameters λ and m_{12}. As the parameters are sequentially turned off, divergent patterns of behavior manifest in the two disjoint scenarios. In case A, the fraction of poles that move to the real axis from the lower half of the second (II) Riemann sheet—an event indicative of a molecular interpretation—is found to be only 0.7%, a statistically insignificant result. This finding offers strong support for the interpretation of the pole as an unbound virtual state, and thus, the interaction between the Σ_c^+ and $\bar{D}^0$ does not have the strength needed to create a bound molecular state. In scenario B the dynamics of the lighter pole cluster, shown in Figure F.3.7(b), are very different. As the parameter m_{12} is reduced to zero this

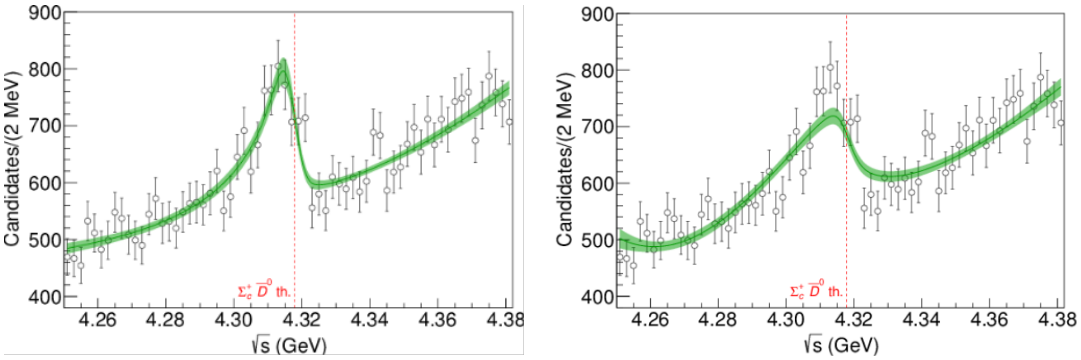

Figure F.3.9: (a) K-matrix fit with a constant background to the $\cos\theta_{P_c}$ data set, this analysis produces a pole in the second Riemann sheet as in the case with $c_{ij} \neq 0$. (b) Flatté fit for the same dataset as case (a), this fit does not generates stable poles in the interest region. Figures taken from [168].

cluster moves onto the fourth (IV) Riemann sheet where it meets the zero of $T_{11}(s)$ and is finally annihilated. That the pole is removed when decoupling shows that it is entirely an effect of the coupling of the two channels. Furthermore, its position on the furthest unphysical sheet provides additional confirmation of its identification as a virtual state in agreement with the interpretation of the P_c pole in case A.

We also performed other systematic analyses employing both the Flatté and K-matrix parameterizations in order to explore in more detail the behavior of the system. If one uses a single K-matrix pole with an off-diagonal constant background, then one finds a pole on the second (II) Riemann sheet, which lies at the same location as that found in case A. On the other hand, the Flatté parameterization cannot reproduce the P_c peak properly and provides unstable poles in the pre-defined region. In order to verify the robustness of these findings, we have performed cross-checks by fitting all of the above approaches to the unweighted $J/\psi p$ mass spectrum within the same kinematic range both with and without the cut of $m_{Kp} > 1.9$ GeV criterion. The results of these fittings are coherent across all examined methodologies, thereby strengthening the validity of the findings.

In section 2.4 we compared the near-threshold amplitude of Refs. [84] and [88] by Dong, Guo and Zou (DGZ) and JPAC collaboration, respectively. The main difference between both amplitudes is the treatment of the breakup momentum of the $J/\psi p$ channel, i.e. k_1. In the case of DGZ it is a constant and, hence, the first cut starting

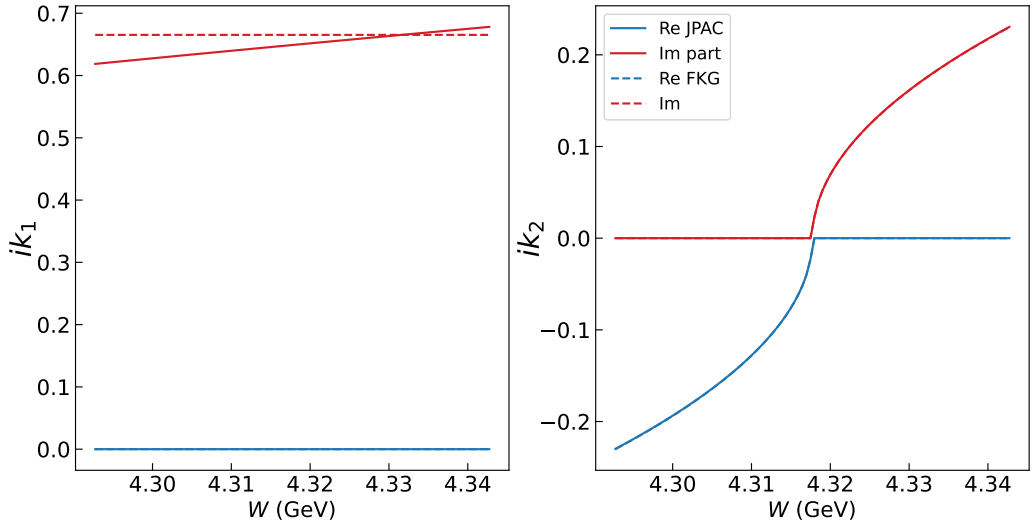

Figure F.3.10: DGZ vs. JPAC momenta. k_2 momenta fully overlap showing that both are the same definition. The momenta are computed for the $P_c(4312)^+$ case. The only difference appears in the real part of the ik_1 momentum, which for the DGZ amplitude is a constant.

from the first threshold has been washed away. In the JPAC amplitude, that is not the case as the square root is kept. Figure F.3.10 shows the DGZ and JPAC momenta for the pentaquark case. On Fig. F.3.11 the parameters obtained for the pentaquark amplitude using the JPAC amplitude are plugged in into the DGZ amplitude and both ampliudes are compared. The differences are shown to be minimal.

The pole position for the JPAC amplitude is [88]:

$$M_P = 4319.7 \pm 1.6\,\text{MeV}, \qquad \Gamma_P = -0.8 \pm 2.4\,\text{MeV}, \tag{3.15}$$

where the $-$ $(+)$ sign in the width stands for IV(II) Riemann sheet, and for the DGZ amplitude using Eq. (2.79):

$$E_p = 4319.45 + i\,0.476\,\text{MeV}, \tag{3.16}$$

$$M_P = 4319.45\,\text{MeV}, \qquad \Gamma_P = 0.95\,\text{MeV}, \tag{3.17}$$

and the pole lays on the upper plane of the II Riemann sheet. Remember that the threshold sits at $\Sigma_2 = 4317.73$ MeV. So, we can conclude that both models give compatible interpretations for the $P_c(4312)^+$ signal.

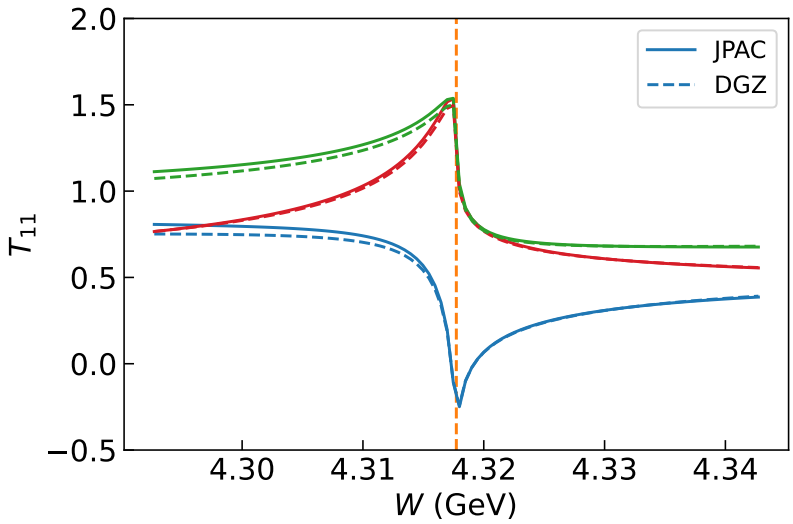

Figure F.3.11: Comparison between the DGZ and JPAC amplitudes for the $J/\psi p \to J/\psi p$ [$T_{11}(s)$]channel using the parameters from [168]. Blue: $\Re[T]$; Red: $\Im[T]$; Green: $|T|$. The orange vertical line highlights the $\Sigma_c^+ \bar{D}^0$ threshold.

3.3 Study of the $f_0(980)$ signal

The study of meson-meson interactions at low energy provides crucial insights on the nonperturbative regime of QCD. This field of research has particular importance to understand possible resonance structures that could deviate from the conventional quark-antiquark picture in the naive quark model. Such interaction will bring a deeper understanding of the strong force at energy scales where QCD is not perturbative and will open up ways to investigate exotic hadronic states, arising from the intricate dynamics of QCD interactions [1].

The scattering of pions and kaons are the simplest two-body reactions involving mesons, i.e. $\pi\pi \to \pi\pi$, $\pi\pi \to K\bar{K}$ and $\pi K \to \pi K$ constitute the major sources of information on the existence and properties of various meson resonances such as the σ, ρ, κ or $f_0(980)$, which are of great interest to understand the light meson spectrum. The scalar meson $f_0(980)$ is particularly interesting given its location very close to the $K\bar{K}$ threshold, making it a primary candidate for a $K\bar{K}$ molecule. Nevertheless, its nature is still an open question, with the conjectured nature going from a compact tetraquark state [171–174] to a $K\bar{K}$ bound state [175, 176]. Following the work for the

$P_c(4312)^+$ in 3.2, we perform a coupled-channel amplitude analysis of the $\pi\pi \to \pi\pi$ and $\pi\pi \to K\bar{K}$ S wave. The $f_0(980)$ resonance is well suited for study within an S wave amplitude model, as the absence of spin simplifies the scattering amplitude and avoids the complications introduced by helicity. This S wave treatment then allows a near-threshold analysis that is not only analytically manageable but also provides flexibility in the interpretation of the resonance as a bound state, virtual state, or molecular state as is possible using the model discussed in [88], by focusing on the narrow energy region around the $K\bar{K}$ threshold, where the coupled-channel effects of the resonance are pronounced, we can give a systematic basis to the understanding of the $f_0(980)$ resonance. This model allows for an interpretation of the resonance structure based on its pole position in the complex energy plane and accommodates many hypotheses on the internal structure of the resonance without implying a rigid classification. In that way, it will be possible to conclude if the $f_0(980)$ behaves like a molecular state, bound state, or virtual state by studying the nature of its pole parameters.

In this work, we analyze the dispersive analysis of $\pi\pi \to \pi\pi$ and $\pi\pi \to K\bar{K}$ channels done in [177] focusing on the near-threshold data for $\pi\pi \to \pi\pi$ and $\pi\pi \to K\bar{K}$ interactions, which allows performing an analysis that is sensitive to the coupled-channel dynamics of the resonance. We assume that the 4π channel is negligible at the energies under study. We reduce the problem to a two-channel case in which $\pi\pi \to \pi\pi$, $\pi\pi \to K\bar{K}$, and $K\bar{K} \to K\bar{K}$ are part of a coupled-channel amplitude, given by two phase-shifts ($\delta_{\pi\pi}(s)$, $\delta_{K\bar{K}}(s)$) and an inelasticity ($\eta(s)$). Both $\pi\pi \to \pi\pi$ and $\pi\pi \to K\bar{K}$ processes have been extensively studied in the literature (see for instance [177, 178]) predominantly because the experimental information is much more favorable than for $K\bar{K} \to K\bar{K}$ scattering.

In a two-channel scenario, these final states are enough to reconstruct the full amplitude, as the third $K\bar{K} \to K\bar{K}$ channel is given by unitarity, as shown in Eq. (2.49). Hence, both $\pi\pi \to \pi\pi$ and $\pi\pi \to K\bar{K}$ amplitudes are given by the same phase-shift below the $K\bar{K}$ threshold. This is known as the Fermi–Watson theorem [179], arising as a result of unitarity. In principle, the ideal situation to describe a resonance around a threshold opening includes experimental information above and below it. However, even if the phase of $\pi\pi \to K\bar{K}$ is given by data on $\pi\pi \to \pi\pi$, the modulus cannot be fixed as there is no data below the $K\bar{K}$ threshold.

In our case, we will make use of information coming from the "CFD" results of [180] for $\pi\pi \to \pi\pi$. We will also use the results "CFD$_{\rm C}$" and "CFD$_{\rm B}$" from appendix C of [177], although, for the energies under scrutiny, these solutions and the ones in the main text of the manuscript are pretty much identical. Specifically, we are interested in a narrow energy region of $40 - 50\,\text{MeV}$ around the $K\bar{K}$ threshold. Both $\pi\pi \to \pi\pi$ and $\pi\pi \to K\bar{K}$ dispersion relations are applicable in that window and their dispersive results are considered robust inputs to our analysis.

It is worth noting that these dispersive results are not coupled to one another, *i.e.*, no coupled-channel dispersive analysis has been performed. In practice, there is evidence that there are channels other than $K\bar{K}$ that can couple to $\pi\pi$ interactions around the 1 GeV region, most probably the 4π threshold. We consider this contribution subdominant however and we will neglect it entirely. Moreover, the $\pi\pi \to K\bar{K}$ dispersive modulus for the amplitude [177, 181, 182] deviates from the available $\pi\pi \to K\bar{K}$ data around the $K\bar{K}$ threshold, which will induce some noticeable tension in the following fits.

The "CFD$_{\rm C}$" and "CFD$_{\rm B}$" results come from using different sets of $\pi\pi \to K\bar{K}$ data for the modulus of the scalar partial-wave g_0^0. These data were measured by the Argonne and Brookhaven experimental collaborations. The former is based on the results of [183, 184], while the latter uses the data from [185]. These data sets produce different, incompatible results. Note that, in the past, some analyses [186, 187] have rescaled the latter results by an overall normalization to make them compatible with the previous measurements. In previous dispersive works [177, 188] an attempt was made to study both solutions separately, with the aim to understand if dispersion relations could select a preferred set. No significant preference was found, and thus we will use both sets of results in our analysis.

These results come in the form of results from an integral equation, which are smooth functions of the energy, for which an arbitrary set of bins can be produced. In practice, the binning for $\pi\pi \to \pi\pi$ is given every 2.1 MeV, and for $\pi\pi \to K\bar{K}$ it is given by 2.3 MeV. Roughly speaking, we take values of these dispersive results every 1 MeV in the energy. We fit these pseudo-data and perform the uncertainties analysis using bootstrap.In what follows we will refer to dataset B(C) as the one made out of combining the binned "CFD" and "CFD$_{\rm B}$"("CFD$_{\rm C}$") results.

In the standard analysis of the partial wave, an amplitude is postulated and data/partial waves are fitted with such amplitude. In our case, we are interested in an energy region close to the $K\bar{K} \to K\bar{K}$ threshold where the $f_0(980)$ appears. For that purpose, we use a two-channel amplitude under the effective range (ER) approximation to describe the dispersive S waves for $\pi\pi \to \pi\pi, K\bar{K}$ channels shown in F.3.6, i.e. equation (2.66), for the sake of clarity, we re-write the equation below:

$$T_{ij}^{-1}(s) = \mu_{ij}(s) - ik_i\,\delta_{ij}, \tag{3.18}$$

with $i, j = 1, 2$. Here $k_i = \sqrt{s - s_i}$ with $s_1 = 4m_\pi^2$, $s_2 = 4m_K^2$ are the thresholds of the two channels. Consistently with the ER expansion near threshold [49, 83, 87] we use k_i instead of the two-body phase space, and we approximate it by a square root.

As we discuss in section 2.4, the pole position is determined by solving

$$(M_{11} - c_{11}s - ik_1)(M_{22} - c_{22}s - ik_2) - (M_{12} - c_{12}s)^2 = 0, \tag{3.19}$$

which corresponds to the denominator of T. By defining in $q = -ik_2$, (3.19) becomes a four degree polynomial in s,

$$\begin{aligned}&(s_2 - s_1 - q^2)\left[M_{22} + q - c_{22}(s_2 - q^2)\right]^2 \\ &+ \Big\{\left[M_{12} - c_{12}(s_2 - q^2)\right]^2 \\ &\quad + \left[c_{11}(s_2 - q^2) - M_{11}\right]\left[M_{22} + q - c_{22}(s_2 - q^2)\right]\Big\}^2 = 0,\end{aligned} \tag{3.20}$$

with eight poles solutions. Equation (2.87) presented in section 2.4 is equivalent to (3.19) but we present here the previous step before re-writing it as a function of the variable change q.

To identify the Riemann sheet for each pole we have to pay attention to the sign of:

$$R_2 = -ik_2 = -i\sqrt{s - s_2}, \tag{3.21a}$$
$$R_1 = -ik_1 = -i\sqrt{s - s_1}. \tag{3.21b}$$

The poles in s are obtained solving $s = (m_K + m_K)^2 - q^2$. The poles appears in

conjugate pairs, each on a sheet identified by (η_1, η_2) pair:

$$\eta_1 = \text{Sign}\,\Re\left[\frac{(M_{12} - c_{12}s)^2}{M_{22} + q - c_{22}s} + c_{11}s - M_{11}\right], \tag{3.22a}$$

$$\eta_2 = \text{Sign}\;\Re\left[q\right], \tag{3.22b}$$

or by the customary naming scheme presented in 2.4.

As in the case for the $P_c(4312)^+$ discussed in 3.2, the physical interpretation of the poles is provided by the Morgan-Pennington criterion [189, 190]. By definition, a resonance is a pole in the closest unphysical Riemann sheet, however, with the proliferation of Riemann sheets as new channels open, it is possible for an unique resonance to have poles in the additional Riemann sheets. In the two-channel case at hand of a resonance below the second threshold, *i.e.* $K\bar{K} \to K\bar{K}$, the expectation is that the $f_0(980)$ is a pole on sheet II. The key question is if it has an additional pole on sheet III given that such pole is sufficiently close to the $K\bar{K} \to K\bar{K}$ threshold. The appearance of such pole indicates a quark-model-like composition making a pure molecular interpretation impossible. Consequently, the lack of a pole on sheet III is evidence of the molecular nature of the state. The reasoning, based on the analytical properties of the amplitude, is illustrated in F.3.8 (there the cuts and states corresponds to the $P_c(4312)^+$ case, but it is similar for the f_0). Three cases are presented: compact, molecular, and virtual. The *uncoupled channels* case depicts the situation where the $\pi\pi$ and $K\bar{K} \to K\bar{K}$ channels are decoupled. Each channel would have two Riemann sheets with the unitarity cut starting at the corresponding threshold. If the $f_0(980)$ resonance is a compact quark state it is present as a pole in each channel (top). Most likely with a small imaginary part. If it is a $K\bar{K} \to K\bar{K}$ molecule it has to be a pole below threshold on sheet I of the $K\bar{K} \to K\bar{K}$ channel with no pole appearing in the $\pi\pi$ channel (center), and finally if it is a $K\bar{K} \to K\bar{K}$ virtual state it should appear as a pole below threshold on sheet II of the $K\bar{K} \to K\bar{K}$ channel with, again, no pole appearing in the $\pi\pi$ channel (bottom). When the channels are coupled the amplitude contains four Riemann sheets as shown in F.3.12 and any pole in the real axis has to move to an unphysical sheet as they acquire a width. This is depicted in the *coupled channels* case. Bear in mind that the analyticity of the amplitude demands that poles cannot just "disappear", they have to move somewhere, although that somewhere could be

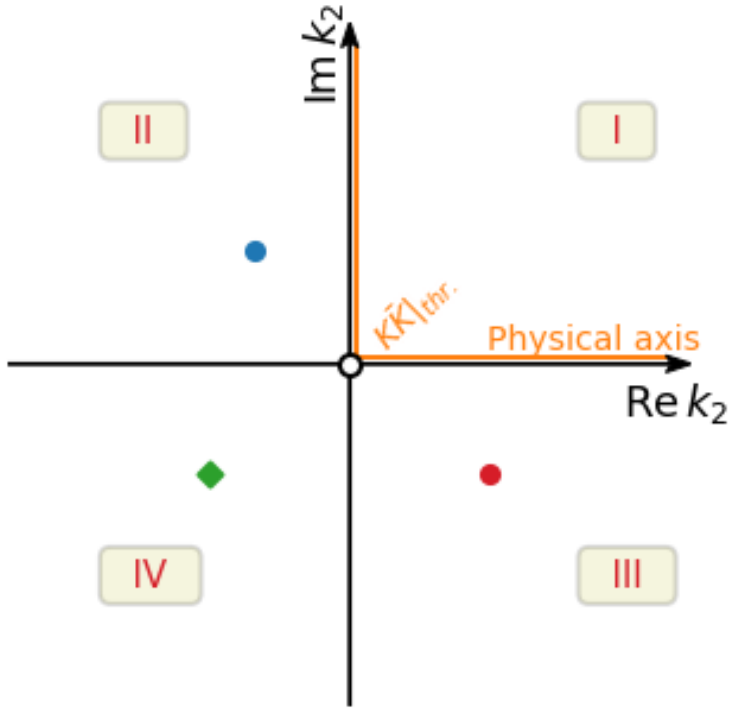

Figure F.3.12: Analytical structure in the k_2-plane of the coupled-channel amplitude in the proximity of the $K\bar{K} \to K\bar{K}$ threshold. The amplitude can have poles on sheets II and IV under the scattering length approximation and on both sheets II, III, and IV under the effective range approximation.

infinity. In the compact case each pole would be located in its closest sheet, *i.e.* the one on the $\pi\pi$ channel to sheet II and the one on the $K\bar{K} \to K\bar{K}$ channel to sheet III. In the molecular case there is only one pole which can only migrate to sheet II. In the virtual state case, the coupling of the two channels puts automatically the pole on sheet IV and either stays on it or migrates to the nearby sheet II. In essence, one unaccompanied sheet II pole indicates a molecular state, while a pair of poles on sheets II and III is evidence of a state originating from antiquark-quark forces.

We perform least-square fits to the B and C datasets using both the SL and ER approaches. Results for the fits are shown in F.3.14. Fit parameters and pole extractions are given in C.3.6. The first apparent result is that the qualitative features of the partial wave are reproduced just with the SL approach. Quantitatively, dataset B is poorly reproduced while dataset C is reasonably well reproduced with both the SL and ER approaches. The best fit using any approach provides a single pole on the II RS in the region near the $K\bar{K} \to K\bar{K}$ threshold,

Table C.3.6: Summary of best fits and pole locations (s_p) in the complex s-plane.

	dataset B		dataset C	
Model	Scattering Length	Effective Range	Scattering Length	Effective Range
# params.	3	6	3	6
χ^2/dof	11.7	4.5	6.8	1.8
M_{11}	0.17(5)	2.9(1.0)	0.0(1)	4.7(6)
M_{22}	−0.1290(4)	−1.5(2)	−0.1287(3)	−0.8(2)
M_{12}	−0.379(7)	1.4(2)	−0.398(8)	0.8(1)
c_{11}	–	3.4(1.1)	–	5.2(7)
c_{22}	–	−1.4(2)	–	−0.7(3)
c_{12}	–	1.8(2)	–	1.3(2)
Riemann Sheet	II	II	II	II
$\sqrt{s_p}$ (MeV)	$992(2) - i\,22(1)$	$1000.5(9) - i\,3.8(9)$	$997(2) - i\,21(3)$	$1002(1) - i\,3.8(9)$
$M_p = \mathrm{Re}\sqrt{s_p}$ (MeV)	992(2)	1000.5(9)	997(2)	1002(1)
$\Gamma_p = -2\,\mathrm{Im}\sqrt{s_p}$ (MeV)	45(2)	7.6(1.5)	42(5)	7.5(1.8)

hinting to a $K\bar{K} \to K\bar{K}$ molecular interpretation.

The uncertainties are computed using the bootstrap technique as discussed in section 2.6.1. In the standard bootstrap approach [21] the error is computed by resampling each data point according to a Gaussian distribution whose width is that of the experimental datapoint. The uncertainties are reported in C.3.6 and F.3.13.

In table C.3.6, the inspection of resonance $f_0(980)$ displays critical insight into the behavior of the real and imaginary parts of its pole position. These parameters show the manifestation of the resonance for various models and datasets in the complex energy plane, helping to connect theoretical constructs to the precision of the available data. The real part of the resulting poles is rather stable across models and datasets, ranging from 992 MeV (dataset B, SL) to 1002 MeV (dataset C, ER), which implies stable estimation of the energy of the resonance around the $K\bar{K} \to K\bar{K}$ threshold. In contrast, the imaginary part of the resonance differs quite a bit between models. In SL fits, the imaginary part enters larger decay properties $-i22$ MeV, while ER fits gives more precise values $-i3.8$ MeV. The difference highlights that ER models are most sensitive to parameter changes, depending more on higher-order corrections, which could, in principle, impose too strong constraints on the dynamics disregarding multi-channel effects, or contributions from 4π or isospin-breaking terms.

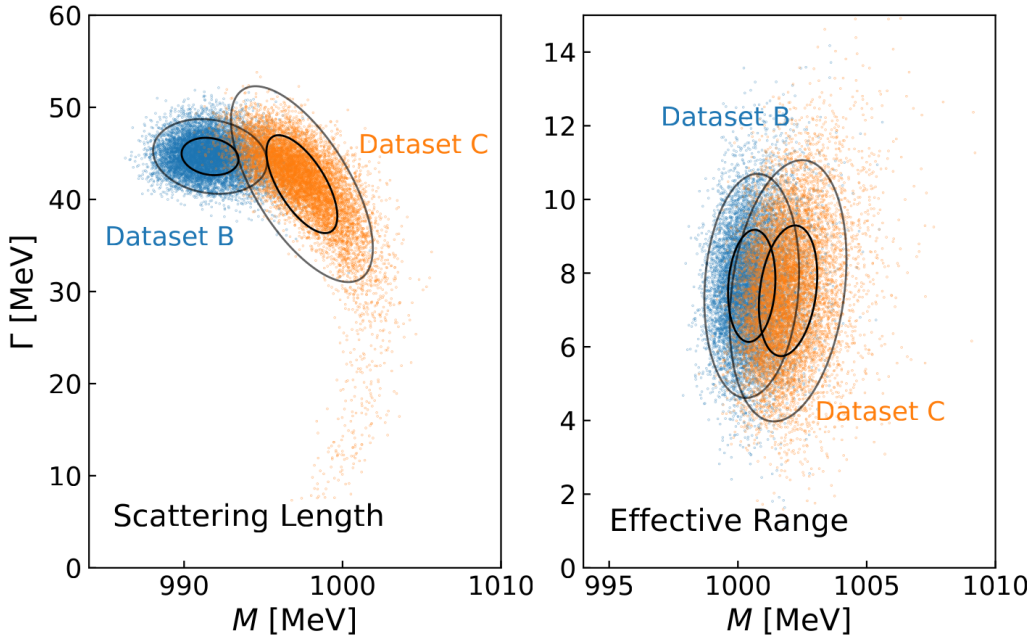

Figure F.3.13: Masses ($M = \Re\sqrt{s_p}$) and widths $\Gamma = -2\Im\sqrt{s_p}$ obtained from the bootstrap analysis for datasets B (blue) and C (orange) using the SL (left) and ER (right) models. The ellipses represent the 1 and 2σ uncertainties for each pole.

The χ^2/dof decreases with increasing parameters, which indicates a trade-off between fit quality and physical interpretability. In both data sets, ER fits give much smaller χ^2/dof values (4.5 for dataset B and 1.8 for dataset C) compared to SL fits (11.7 and 6.8, respectively). Although this improvement is associated with a better statistical fit to the data, decreased flexibility in ER models justifies questions about their wider applicability. For instance, the strictly limited imaginary part in ER diverges from results obtained by robust methods like unitarized chiral perturbation theory, which implies that more channels or corrections may have to be explicitly included.

Comparisons of datasets further emphasize the significance of data quality in the determination of poles. Dataset B demonstrates elevated χ^2/dof values and marginally greater fluctuations in pole positions relative to dataset C, suggesting the possibility of inferior resolution or more extensive systematic uncertainties. Conversely, dataset C, characterized by stricter pole constraints and diminished χ^2/dof, seems more appropriate for resonance analysis, highlighting the critical nature of accurate experimental inputs in the examination of near-threshold

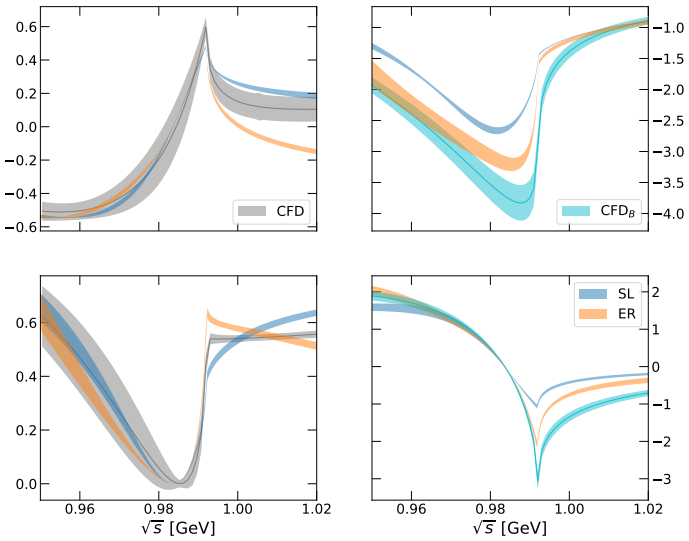

(a)

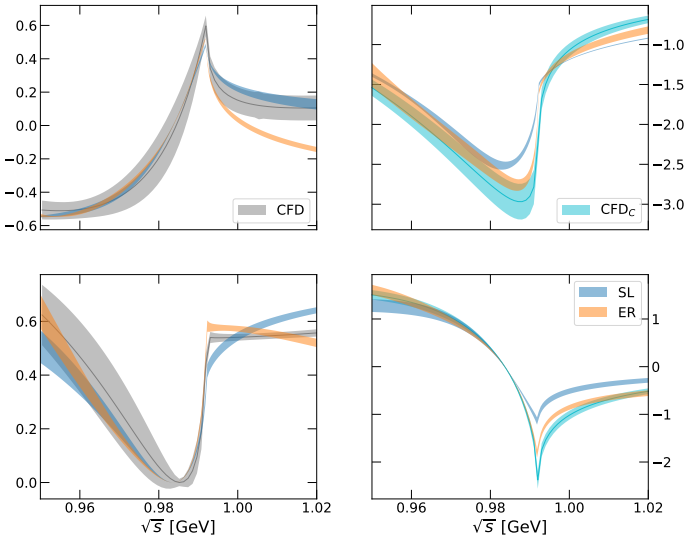

(b)

Figure F.3.14: Fits to the experimental data using the model described in Section 2.4. Panel (a) illustrates the fits to the $\pi\pi \to \pi\pi$ data (left) and the CFD_B data (right), with the gray and aquamarine bands representing the experimental $\pi\pi \to \pi\pi$ and CFD pseudodata respectively, the blue bands indicating the fit with the SL model, and the orange bands corresponding to the ER model. Similarly, panel (b) shows the fits to the $\pi\pi \to \pi\pi$ data (left) and the CFD_C data (right), following the same color identification as in panel (a). The thickness of the bands is proportional to the error band associated with the pseudodata points. In both cases, the ER model demonstrates a better fit to the CFD data compared to the SL model.

dynamics. These results confirm the $f_0(980)$ classification as a near-threshold resonance strongly coupled to the $K\bar{K} \rightarrow K\bar{K}$ channel. The observed model-dependent variations of the imaginary part of the pole clearly show the importance of an adequate choice of the framework for amplitude analysis. While the SL models provide a robust and global characterization of the $f_0(980)$, the ER models show promise for detailed studies, but require careful handling to avoid overfitting and to remain consistent with established theoretical and empirical findings. This review also underscores the need to incorporate additional channels and dynamics, hence offering a crucial guideline for future studies of hadronic resonances. Building on the analysis, extra channels and corrections will play an important role in the deeper understanding of $f_0(980)$ resonance dynamics. Of these, the channel 4π is important, as this will contribute to the inelasticity seen close to the resonance. This would resolve the discrepancies in the imaginary part of the pole, mainly in the ER models. Moreover, explicit consideration has to be given to isospin-breaking effects due to the mass difference between K^+K^- and $K^0\bar{K}^0$ thresholds. These thresholds induce subtle but significant variations in the coupling and position of the resonance poles, which are ignored in the strict isospin symmetry assumption.

The analysis presented in this thesis, despite its limitations, is far from redundant; it plays an essential role in teasing apart the theoretical and empirical intricacies associated with the $f_0(980)$ resonance. This work has brought forth, by making use of near-threshold formalisms such as Scattering Length (SL) and Effective Range (ER), how crucial effects that gain importance around thresholds are: the interaction of neglected channels such as 4π and isospin breaking contributions. The discrepancies in this work, compared with other studies of the pole extractions, reveal how near-threshold effects, often simplified or ignored, can play a dominant role in the understanding of the resonances. This analysis acts as a diagnostic tool that helps to identify the sources of systematic discrepancies, creating a floor for improving methods that match near-threshold expansions to coupled-channel models. By doing so, it not only ascertains the practicality of the models used but also opens up an insight into the intricate dynamics that prove essential for a full understanding of the $f_0(980)$ and similar resonances.

4. Conclusions

To explain all nature is too difficult a task for any one man or even for any one age. It is much better to do a little with certainty and leave the rest for others that come after than to explain all things by conjecture without making sure of any thing.

I. Newton

The findings in this thesis synthesize the results of three interrelated studies on the physics of hadrons, bringing into the spotlight the intricate interactions between the analytic features of scattering amplitudes and dynamics near threshold. These have generated a wealth of knowledge on the N^* and Δ^* baryonic resonances using Regge theory, the hidden-charm pentaquark $P_c(4312)^+$, and the scalar meson $f_0(980)$. By integrating advanced modeling methodologies with statistical validation frameworks that range from simple parametric uncertainty analysis to more advanced bootstrap analyses, this research significantly extends our theoretical understanding of dynamics governing such resonances.

Contrary to the conventional applications to slopes and intercepts of trajectories, the present investigation considers the general analytic continuation of the scattering amplitudes. By using the basic principles of unitarity, analyticity, and crossing symmetry, the present study shows that the singularities in the complex angular momentum plane carry significant physical information concerning N^* and Δ^* resonances. These findings go on to make the analytical framework associated with Regge trajectories more versatile for a better comprehension of the dynamics. Validation of parameters derived here, by statistical techniques—most dominantly the bootstrap resampling—assures the stability and robustness of these results considering statistical fluctuations in data inputs; hence, pushing the phenomenology of Regge theory even further and increasing the range to higher energies within hadron-hadron interactions. The study of the $P_c(4312)^+$ resonance is

particularly important for the characterization of this state, lying near the threshold of $\Sigma_c^+ \bar{D}^0$. Using a coupled-channel amplitude formalism, this work determines a pole on the IV Riemann sheet, which conclusively provides the evidence for its classification as a virtual state rather than a molecular bound state. This study is based on a thorough analysis of the pole's behavior as a function of various channel couplings and parameter values, demonstrating that the attractive forces existing near threshold, although appreciable, are not strong enough to bind the system within a molecular structure. Instead, the observed behavior is consistent with the properties of a virtual state, a conclusion sustained also by the regular poles' movement across Riemann sheets.

Statistical methods, such as the bootstrap techniques, give a quantitative estimate of the uncertainty, increasing the credibility of such results. These results explain the properties of $P_c(4312)^+$ and show the complex dynamics that are typical for near-threshold phenomena. The $f_0(980)$ scalar meson is studied in the analogous framework of coupled-channel dynamics near the $K\bar{K}$ threshold. Analytic continuation of the scattering amplitude suggests the existence of a pole structure that indicates the existence of a dynamically generated state, with properties mainly determined by $K\bar{K}$ interactions. The very same methodological framework widely applied to $P_c(4312)^+$ and $f_0(980)$ underlines the strength and universality of the analytic and statistical techniques developed in this thesis. By inclusion of dispersion relations and extensive statistical verification, the present analysis ensures the reliability of the results, which afford a rational explanation for peculiar properties of the scalar meson deviating from conventional quark-model predictions.

In addition to the specific case studies, this thesis presents more general methodological developments relevant to the study of hadronic systems. The general amplitude analysis framework developed in this work is a versatile tool for the study of complex multi-channel and multi-threshold dynamics. By emphasizing the importance of analytic properties and implementing strict statistical validation, this work bridges the gap between phenomenological models and empirical data, thus providing a sound foundation for future research efforts.

While this research acknowledges some limitations of experimental uncertainties and model dependencies, it recognizes that future improvements in experimental data with higher precision, refined theoretical constraints, and incorporation of results from

lattice QCD will be beneficial for such analyses. Furthermore, a deeper extension of the statistical framework to Bayesian methods or other resampling techniques may still improve the robustness and interpretative power of such analyses. In summary, this dissertation increases the knowledge of hadronic resonances by incorporating theoretical precision, new modeling techniques, and statistical reliability.

The tests of N^*, Δ^*, $P_c(4312)^+$, and $f_0(980)$ demonstrate the effectiveness of a coherent framework in dealing with the intricate interplay of analytic and dynamic characteristics in the hadronic spectrum. These contributions will serve to shed light on the properties of certain resonances, while setting a basis for future research, especially on near-threshold phenomena and their far-reaching implications in hadronic physics.

References

[1] T. Muta, *Foundations Of Quantum Chromodynamics: An Introduction to Perturbative Methods in Gauge Theories*. World Scientific Lecture Notes in Physics, World Scientific Publishing Company, 3 ed., 2009.

[2] M. E. Peskin and D. V. Schroeder, *An introduction to Quantum Field Theory*. Frontiers in Physics, Addison-Wesley Pub. Co, 1995.

[3] S. Narison, *QCD as a Theory of Hadrons: From Partons to Confinement (Cambridge Monographs on Particle Physics, Nuclear Physics and Cosmology)*. Cambridge University Press, 1 ed., 2004.

[4] J. Greensite, "An introduction to the confinement problem," *Lect. Notes Phys.*, vol. 821, 2011.

[5] S. Scherer, "Introduction to chiral perturbation theory," *Adv. Nucl. Phys.*, vol. 27, p. 277, 2003.

[6] R. Flores-Mendieta and J. L. Goity, "Baryon vector current in the chiral and $1/N_c$ expansions," *Phys. Rev. D*, vol. 90, no. 11, p. 114008, 2014.

[7] I. P. Fernando and J. L. Goity, "Baryon chiral perturbation theory combined with the $1/N_c$ expansion in $SU(3)$: Framework," *Phys. Rev. D*, vol. 97, p. 54010, mar 2018.

[8] M. Tanabashi and Others, "Review of Particle Physics," *Phys. Rev.*, vol. D98, no. 3, p. 30001, 2018.

[9] A. D. Martin and T. D. Spearman, *Elementary Particle Theory*. North-Holland Publishing Company-Amsterdam, 1970.

[10] B. L. Ioffe, V. S. Fadin, and L. N. Lipatov, *Quantum Chromodynamics: Perturbative and Nonperturbative Aspects*. Cambridge Monographs on Particle Physics, Nuclear Physics and Cosmology, CUP, 2010.

[11] M. Gell-Mann, "A schematic model of baryons and mesons," *Physics Letters*, vol. 8, no. 3, p. 214–215, 1964.

[12] A. Petermann, "Propriétés de l'étrangeté et une formule de masse pour les mésons vectoriels," *Nucl. Phys.*, vol. 63, no. 2, pp. 349–352, 1965.

[13] G. Zweig, "An SU(3) model for strong interaction symmetry and its breaking. Version 2," in *Developments in the Quark Theory of Hadrons, Volume 1. Edited*

by D. Lichtenberg and S. Rosen. pp. 22-101 (D. B. Lichtenberg and S. P. Rosen, eds.), p. 22–101, Hadronic Press, 1964.

[14] A. De Rújula, "Archeology and evolution of QCD," *EPJ Web Conf.*, vol. 137, p. 01007, 2017.

[15] S. L. Glashow, "The Standard Model," 2018.

[16] V. V. Anisoich, M. N. Kobrinsky, J. Nyiri, and Y. M. Shabelski, *Quark Model and High Energy Collisions*. World Scientific, 2nd ed., 2004.

[17] R. Aaij and Others, "Observation of $J/\psi p$ Resonances Consistent with Pentaquark States in $\Lambda_b^0 \to J/\psi K^- p$ Decays," *Phys. Rev. Lett.*, vol. 115, no. 7, p. 72001, 2015.

[18] R. Aaij and Others, "Model-Independent Evidence for $J/\psi p$ Contributions to $\Lambda_b^0 \to J/\psi p K^-$ Decays," *Phys. Rev. Lett.*, vol. 117, no. 8, p. 82002, 2016.

[19] R. Aaij and Others, "Observation of a narrow pentaquark state, $P_c(4312)^+$, and of two-peak structure of the $P_c(4450)^+$," *Phys.Rev.Lett*, vol. 122, p. 222001, 2019.

[20] C. Fernández-Ramírez, M. Mikhasenko, and A. Pilloni, "Joint Physics Analysis Center github: Charmonia plot project," 2024.

[21] M. Albaladejo *et al.*, "Novel approaches in hadron spectroscopy," *Prog. Part. Nucl. Phys.*, vol. 127, p. 103981, 2022.

[22] M. Mikhasenko, A. Pilloni, J. Nys, M. Albaladejo, C. Fernández-Ramírez, A. Jackura, V. Mathieu, N. Sherrill, T. Skwarnicki, and A. P. Szczepaniak, "What is the right formalism to search for resonances?," *Eur. Phys. J.*, vol. C78, no. 3, p. 229, 2018.

[23] M. Jacob and G. C. Wick, "On the General Theory of Collisions for Particles with Spin," *Annals of Physics*, vol. 7, no. 4, p. 404–428, 1959.

[24] S. Prelovsek, U. Skerbis, and C. B. Lang, "Operators for scattering of particles with spin," *PoS*, vol. LATTICE201, p. 98, 2016.

[25] F. Calogero, J. M. Charap, and E. J. Squires, "The continuation in total angular momentum of partial-wave scattering amplitudes for particles with spin," *Annals of Physics*, vol. 25, no. 3, p. 325–339, 1963.

[26] B. E. Y. Svensson, "On the kinematic singularities of helicity amplitudes for multi-particle processes," *Nuclear Physics B*, vol. 15, no. 1, p. 93–117, 1970.

[27] G. Cohen-Tannoudji, A. Morel, and H. Navelet, "Kinematical singularities, crossing matrix and kinematical constraints for two-body helicity amplitudes," *Annals of Physics*, vol. 46, no. 2, p. 239–316, 1968.

[28] J. M. Charap and E. J. Squires, "On complex angular momentum in many-channel potential-scattering problems. I," *Annals of Physics*, vol. 20, no. 1,

p. 145–156, 1962.

[29] J. M. Charap and E. J. Squires, "On complex angular momentum in many-channel potential-scattering problems, II," *Annals of Physics*, vol. 21, no. 1, p. 8–28, 1963.

[30] J. M. Charap and E. J. Squires, "On complex angular momentum in many-channel potential-scattering problems, III," *Annals of Physics*, vol. 25, no. 2, p. 143–154, 1963.

[31] Y. Hara, "Analyticity Properties of Helicity Amplitudes and Construction of Kinematical Singularity-Free Amplitudes for Any Spin," *Phys. Rev.*, vol. 136, p. B507——B514, oct 1964.

[32] E. Byckling and K. Kajantie, *Particle Kinematics*. John Wiley & Sons, 1972.

[33] W. Rindler, *Relativity: special, general, and cosmological*. Oxford University Press, USA, 2 ed., 2006.

[34] G. Källén, *Elementary Particle Physics*. Addison-Wesley Publishing Company, 1 ed., 1964.

[35] M. Maggiore, *A Modern Introduction to Quantum Field Theory*. Oxford Master Series in Physics, Oxford University Press, 2004.

[36] A. V. Anisovich, V. V. Anisovich, M. A. Matveev, V. A. Nikonov, J. Nyiri, and A. V. Sarantsev, *Three-Particle Physics and Dispersion Relation Theory*. World Scientific, 1st ed., 2013.

[37] R. J. Eden, P. V. Landshoff, D. I. Olive, and J. C. Polkinghorne, *The Analytic S-Matrix*. Cambridge, UK: Cambridge University Press, 1966.

[38] P. D. B. Collins, *An Introduction to Regge Theory and High-Energy Physics*. Cambridge Monographs on Mathematical Physics, Cambridge, UK: Cambridge Univ. Press, 2009.

[39] N. N. Bogolubov, A. A. Logunov, A. I. Oksak, and I. Todorov, *General principles of quantum field theory*. Mathematical Physics and Applied Mathematics, Springer, 1 ed., 1989.

[40] A. Bohm, *Quantum Mechanics: Foundations and Applications*. Texts and Monographs in Physics, Springer Berlin Heidelberg, 1986.

[41] V. N. Gribov, *Strong interactions of hadrons at high energies: Gribov lectures on Theoretical Physics*. Cambridge University Press, 2012.

[42] W. S. C. Williams, *An Introduction to Elementary Particles*. Pure and Applied Physics 12, Academic Press Inc, 2nd ed., 1971.

[43] R. J. Eden, *High Energy Collisions of Elementary Particles*. Cambridge University Press, 1967.

[44] H. M. Nussenzveig, *Causality and Dispersion Relations*. Mathematics in Science

and Engineering 95, Academic Press, 1972.

[45] R. J. Eden and P. V. Landshoff, "The problem of causality in S-matrix theory," *Annals of Physics*, vol. 31, no. 2, p. 370–390, 1965.

[46] R. G. Newton, *Scattering Theory of Waves and Particles*. Texts and Monographs in Physics, Springer-Verlag Berlin Heidelberg, 2 ed., 1982.

[47] G. Baym, *Lectures On Quantum Mechanics*. Lecture Notes and Supplements in Physics, The Benjamin / Cummings Publishing Company, CRC, 1 ed., 1969.

[48] R. J. Eden, "Regge Poles and Elementary Particles," *Reports on Progress in Physics*, vol. 34, no. 3, 1971.

[49] C. Fernández-Ramírez, I. V. Danilkin, D. M. Manley, V. Mathieu, and A. P. Szczepaniak, "Coupled-channel model for $\bar{K}N$ scattering in the resonant region," *Phys. Rev.*, vol. D93, no. 3, p. 34029, 2016.

[50] S. Mandelstam, "Determination of the Pion-Nucleon Scattering Amplitude from Dispersion Relations and Unitarity. General Theory," *Phys. Rev.*, vol. 112, no. 4, p. 1344–1360, 1958.

[51] S. Mandelstam, "Analytic Properties of Transition Amplitudes in Perturbation Theory," *Phys. Rev.*, vol. 115, no. 6, p. 1741–1751, 1959.

[52] R. Blankenbecler, M. L. Goldberger, N. N. Khuri, and S. B. Treiman, "Mandelstam representation for potential scattering," *Annals of Physics*, vol. 10, no. 1, p. 62–93, 1960.

[53] J. Franklin, "Kinematic Singularities of Partial-Wave Scattering Amplitudes," *Phys. Rev.*, vol. 152, no. 4, p. 1437–1441, 1966.

[54] N. Johannesson, "Kinematic singularities in multi-particle processes derived from basic properties of spinor amplitudes," *Nuclear Physics B*, vol. 28, no. 1, p. 51–60, 1971.

[55] L. C. Wang, "General Method of Constructing Helicity Amplitudes Free from Kinematic Singularities and Zeros," *Phys. Rev.*, vol. 142, p. 1187–1194, feb 1966.

[56] G. C. Fox, "Methods for Constructing Invariant Amplitudes Free from Kinematic Singularities and Zeros," *Phys. Rev.*, vol. 157, p. 1493–1502, may 1967.

[57] K. Hepp, "On the analitycity properties of the scattering amplitude in relativistic quantum field theory," *Helvetica Physica Acta (Switzerland)*, vol. 37, 1964.

[58] C. Itzykson and J. Zuber, *Quantum Field Theory*. Dover Publications, 2006.

[59] A. B. de Monvel, D. Buchholz, D. Iagolnitzer, and U. Moschella, *Rigorous Quantum Field Theory: A Festschrift for Jacques Bros*. Progress in Mathematics 251, Birkhäuser Basel, 1 ed., 2007.

[60] A. Duncan, *The Conceptual Framework of Quantum Field Theory*. Oxford University Press, 1 ed., 2012.

[61] J. Bros, H. Epstein, and V. Glaser, "A proof of the crossing property for two-particle amplitudes in general quantum field theory," *Communications in Mathematical Physics*, vol. 1, no. 3, p. 240–264, 1965.

[62] V. N. Gribov, *The theory of complex angular momenta: Gribov lectures on theoretical physics*. Cambridge Monographs on Mathematical Physics, Cambridge University Press, 2007.

[63] G. B. Arfken, H. J. Weber, and F. E. Harris, *Mathematical Methods for Physicists, Seventh Edition: A Comprehensive Guide*. Academic Press, 7 ed., 2012.

[64] R. Omnès and M. Froissart, *Mandelstam Theory and Regge Poles. An Introduction for Experimentalists*. Frontiers in Physics, W.A. Benjamin, 1963.

[65] A. V. Anisovich, V. V. Anisovich, M. A. Matveev, V. A. Nikonov, J. Nyiri, and A. V. Sarantsev, *Mesons and baryons: systematization and methods of analysis*. World Scientific, 2008.

[66] H. W. Hammer and S. König, "Constraints on a possible dineutron state from pionless EFT," *Phys.Lett.*, vol. B736, p. 208–213, 2014.

[67] F. W. King, *Hilbert transforms:*, vol. 1 of *Encyclopedia of Mathematics and its Applications*. CUP, 2009.

[68] F. W. King, *Hilbert transforms:*, vol. 2 of *Encyclopedia of Mathematics and its Applications*. Cambridge University Press, 1 ed., 2009.

[69] G. Barton, *Introduction to Dispersion Techniques in Field Theory*. Lecture Notes and Supplements in Physics, W A. Benjamin, INC. New York, 1965.

[70] M. Sugawara and A. Kanazawa, "Subtractions in Dispersion Relations," *Phys. Rev.*, vol. 123, p. 1895–1902, sep 1961.

[71] T. Kitazoe and T. Ogimoto, "Subtraction of Dispersion Relation in Multi-Channel Scattering," *Progress of Theoretical Physics*, vol. 29, no. 2, p. 275–278, 1963.

[72] Y. S. Jin and A. Martin, "Number of Subtractions in Fixed-Transfer Dispersion Relations," *Phys. Rev.*, vol. 135, no. 6B, p. B1375——B1377, 1964.

[73] M. Froissart, "Asymptotic Behavior and Subtractions in the Mandelstam Representation," *Phys. Rev.*, vol. 123, no. 3, p. 1053–1057, 1961.

[74] I. T. Todorov and D. T. Haar, *Analytic Properties of Feynman Diagrams in Quantum Field Theory*. Monographs in Natural Philosophy, Elsevier Ltd, Pergamon Press, 1 ed., 1971.

[75] E. C. Titchmarsh, *Introduction to the theory of Fourier integrals*. Oxford

University Press, 2 ed., 1948.

[76] H. Muirhead, *The Physics of Elementary Particles*. Pergamon Press Ltd., 1965.

[77] E. W. Weisstein, *CRC Concise Encyclopedia of Mathematics, Second Edition*. Chapman & Hall/CRC, 2 ed., 2002.

[78] R. Hagedorn, *Introduction to field theory and dispersion relations*. Akademie, 1963.

[79] Y. V. Novozhilov and D. ter Haar, *Introduction to Elementary Particle Theory*. Pergamon Press, 1 ed., 1975.

[80] L. Castillejo, R. H. Dalitz, and F. J. Dyson, "Low's Scattering Equation for the Charged and Neutral Scalar Theories," *Phys. Rev.*, vol. 101, no. 1, p. 453–458, 1956.

[81] D. Hornidge *et al.*, "Accurate Test of Chiral Dynamics in the $\gamma \to p \to \pi 0 p$ Reaction," *Phys. Rev. Lett.*, vol. 111, no. 6, p. 062004, 2013.

[82] S. Schumann *et al.*, "Threshold $\pi 0$ photoproduction on transverse polarised protons at MAMI," *Phys. Lett. B*, vol. 750, pp. 252–258, 2015.

[83] W. R. Frazer and A. W. Hendry, "S-Matrix Poles Close to Threshold," *Phys. Rev.*, vol. 134, p. B1307——B1314, jun 1964.

[84] X.-K. Dong, F.-K. Guo, and B.-S. Zou, "Explaining the Many Threshold Structures in the Heavy-Quark Hadron Spectrum," *Phys. Rev. Lett.*, vol. 126, no. 15, p. 152001, 2021.

[85] S. Weinberg, "Evidence That the Deuteron Is Not an Elementary Particle," *Phys.Rev.*, vol. 137, p. B672–B678, 1965.

[86] M. Mikhasenko, "A triangle singularity and the LHCb pentaquarks," 2015.

[87] A. Pilloni, C. Fernández-Ramírez, A. Jackura, V. Mathieu, M. Mikhasenko, J. Nys, and A. P. Szczepaniak, "Amplitude analysis and the nature of the $Z_c(3900)$," *Phys. Lett.*, vol. B772, p. 200–209, 2017.

[88] C. Fernández-Ramírez, A. Pilloni, M. Albaladejo, A. Jackura, V. Mathieu, M. Mikhasenko, J. A. Silva-Castro, and A. P. Szczepaniak, "Interpretation of the LHCb $P_c(4312)^+$ Signal," *Phys. Rev. Lett.*, vol. 123, no. 9, p. 92001, 2019.

[89] T. Regge, "Introduction to Complex Orbital momenta," *Il Nuovo Cimento (1955-1965)*, vol. 14, no. 5, p. 951–976, 1959.

[90] T. Regge, "Bound States, Shadow States and Mandelstam Representation," *Il Nuovo Cimento (1955-1965)*, vol. 18, no. 5, p. 947–956, 1960.

[91] V. N. Gribov, "Analytic properties of the partial wave amplitudes and the asymptotic behavior of the scattering amplitude," *Sov. Phys. JETP*, vol. 15, p. 873, 1962.

[92] A. Erdelyi, *Higher transcendental functions*, vol. 1. Krieger Pub Co, 1953.

[93] P. D. B. Collins and E. J. Squires, *Regge poles in Particle Physics*. Springer Tracts in Modern Physics 45, Springer Berlin Heidelberg, 1968.

[94] J. T. Londergan, J. Nebreda, J. R. Peláez, and A. Szczepaniak, "Identification of non-ordinary mesons from the dispersive connection between their poles and their Regge trajectories: The $f_0(500)$ resonance," *Phys. Lett.*, vol. B729, p. 9–14, 2014.

[95] J. A. Silva-Castro, C. Fernández-Ramírez, M. Albaladejo, I. V. Danilkin, A. Jackura, V. Mathieu, J. Nys, A. Pilloni, A. P. Szczepaniak, and G. Fox, "Regge phenomenology of the N^* and Δ^* poles," *Phys. Rev. D*, vol. 99, no. 3, p. 34003, 2019.

[96] R. Omnès, *Introduction to Particle Physics*. Wiley, 1971.

[97] G. F. Chew and S. C. Frautschi, "Regge Trajectories and the Principle of Maximum Strength for Strong Interactions," *Phys. Rev. Lett.*, vol. 8, p. 41–44, 1962.

[98] G. C. Rossi and G. Veneziano, "A Possible Description of Baryon Dynamics in Dual and Gauge Theories," *Nucl. Phys.*, vol. B123, p. 507–545, 1977.

[99] L. Montanet, G. C. Rossi, and G. Veneziano, "Baryonium Physics," *Phys. Rept.*, vol. 63, p. 149–222, 1980.

[100] R. Fiore, L. L. Jenkovszky, V. Magas, F. Paccanoni, and A. Papa, "Analytic model of Regge trajectories," *Eur. Phys. J.*, vol. A10, p. 217–221, 2001.

[101] R. Fiore, L. L. Jenkovszky, F. Paccanoni, and A. Prokudin, "Baryonic regge trajectories with analyticity constraints," *Phys. Rev.*, vol. D70, p. 54003, 2004.

[102] C. Fernández-Ramírez, I. V. Danilkin, V. Mathieu, and A. P. Szczepaniak, "Understanding the Nature of $\Lambda(1405)$ through Regge Physics," *Phys. Rev.*, vol. D93, no. 7, p. 74015, 2016.

[103] S. W. MacDowell, "Analytic Properties of Partial Amplitudes in Meson-Nucleon Scattering," *Phys. Rev.*, vol. 116, p. 774–778, 1959.

[104] Y. Georgelin, "Generalized MacDowell Symmetry as a Consequence of CT Invariance," *Phys. Rev. D*, vol. 1, p. 1782–1785, mar 1970.

[105] G. Cowan, K. Cranmer, E. Gross, and O. Vitells, "Asymptotic formulae for likelihood-based tests of new physics," *Eur. Phys. J. C*, vol. 71, p. 1554, 2011. [Erratum: Eur.Phys.J.C 73, 2501 (2013)].

[106] G. Cowan, "Statistical Models with Uncertain Error Parameters," *Eur. Phys. J. C*, vol. 79, no. 2, p. 133, 2019.

[107] J. S. Devinderjit Sivia, *Data Analysis: A Bayesian Tutorial*. , Oxford University Press, USA, 2 ed., 2006.

[108] B. Efron and R. J. Tibshirani, *An Introduction to the Bootstrap*. Chapman &

Hall/CRC Monographs on Statistics & Applied Probability, Taylor & Francis, 1994.

[109] L. A. S. Dennis D. Boos, *Essential Statistical Inference: Theory and Methods*. Springer Texts in Statistics, Springer, 2013 ed., 2013.

[110] F. James and M. Roos, "Minuit: A System for Function Minimization and Analysis of the Parameter Errors and Correlations," *Comput. Phys. Commun.*, vol. 10, p. 343–367, 1975.

[111] K. Levenberg, "A method for the solution of certain non-linear problems in least squares," *Quart. Appl. Math.*, vol. 2, no. 2, p. 164–168, 1944.

[112] D. W. Marquardt, "An algorithm for least-squares estimation of nonlinear parameters," *J. Soc. Ind. Appl. Math.*, vol. 11, p. 431–441, June 1963.

[113] D. Ireland, S. Janssen, and J. Ryckebusch, "A genetic algorithm analysis of resonances in p(γ,K+)Λ reactions," *Nuclear Physics A*, vol. 740, p. 147–167, Aug. 2004.

[114] C. Fernández-Ramírez, E. M. de Guerra, A. Udías, and J. M. Udías, "Properties of nucleon resonances by means of a genetic algorithm," *Physical Review C*, vol. 77, June 2008.

[115] J. Landay, M. Döring, C. Fernández-Ramírez, B. Hu, and R. Molina, "Model Selection for Pion Photoproduction," *Phys. Rev.*, vol. C95, no. 1, p. 15203, 2017.

[116] C. F. J. Wu, "Jackknife, Bootstrap and Other Resampling Methods in Regression Analysis," *The Annals of Statistics*, vol. 14, no. 4, pp. 1261 – 1295, 1986.

[117] S. N. Lahiri, *Bootstrap Methods: A Review*, pp. 231–255. World Scienticic, 2006.

[118] B. Efron and R. Tibshirani, "Bootstrap Methods for Standard Errors, Confidence Intervals, and Other Measures of Statistical Accuracy," *Statistical Science*, vol. 1, no. 1, pp. 54 – 75, 1986.

[119] P. J. Bickel and D. A. Freedman, "Asymptotic normality and the bootstrap in stratified sampling," *The Annals of Statistics*, vol. 12, no. 2, pp. 470–482, 1984.

[120] D. R. Mooney C.Z., *Bootstrapping: A Nonparametric Approach to Statistical Inference*. Quantitative Applications in the Social Sciences, Sage, 1993.

[121] D. V. H. A. C. Davison, *Bootstrap Methods and their Application*. Cambridge Series in Statistical and Probabilistic Mathematics, Cambridge University Press, 1997.

[122] A. R. Henderson, "The bootstrap: A technique for data-driven statistics. using computer-intensive analyses to explore experimental data," *Clinica Chimica Acta*, vol. 359, no. 1, pp. 1–26, 2005.

[123] R. E. Cutkosky, C. P. Forsyth, R. E. Hendrick, and R. L. Kelly, "Pion - Nucleon

Partial Wave Amplitudes," *Phys. Rev.*, vol. D20, p. 2839, 1979.

[124] R. E. Cutkosky, C. P. Forsyth, J. B. Babcock, R. L. Kelly, and R. E. Hendrick, "Pion - Nucleon Partial Wave Analysis," in *Baryon 1980. Proceedings, 4th International Conference on Baryon Resonances, Toronto, Canada, July 14-16, 1980*, p. 19, 1980.

[125] D. Rönchen, M. Döring, and U. G. Meißner, "The impact of $K^+\Lambda$ photoproduction on the resonance spectrum," *Eur. Phys. J.*, vol. A54, no. 6, p. 110, 2018.

[126] A. V. Anisovich, R. Beck, E. Klempt, V. A. Nikonov, A. V. Sarantsev, and U. Thoma, "Properties of baryon resonances from a multichannel partial wave analysis," *Eur. Phys. J.*, vol. A48, p. 15, 2012.

[127] V. Sokhoyan and Others, "High-statistics study of the reaction $\gamma p \to p2\pi^0$," *Eur. Phys. J.*, vol. A51, no. 8, p. 95, 2015.

[128] A. Švarc, M. Hadžimehmedović, H. Osmanović, J. Stahov, and R. L. Workman, "Pole structure from energy-dependent and single-energy fits to GWU-SAID πN elastic scattering data," *Phys. Rev.*, vol. C91, no. 1, p. 15207, 2015.

[129] R. L. Workman, R. A. Arndt, W. J. Briscoe, M. W. Paris, and I. I. Strakovsky, "Parameterization dependence of T matrix poles and eigenphases from a fit to πN elastic scattering data," *Phys. Rev.*, vol. C86, p. 35202, 2012.

[130] A. Švarc, M. Hadžimehmedović, R. Omerović, H. Osmanović, and J. Stahov, "Poles of Karlsruhe-Helsinki KH80 and KA84 solutions extracted by using the Laurent-Pietarinen method," *Phys. Rev.*, vol. C89, no. 4, p. 45205, 2014.

[131] G. Höhler, *Pion Nucleon Scattering. Part 2: Methods and Results of Phenomenological Analyses.* Landolt-Bornstein, Springer-Verlag Berlin Heidelberg, 1983.

[132] R. Koch, "Improved πN Partial Waves Consistent With Analyticity and Unitarity," *Z. Phys.*, vol. C29, p. 597, 1985.

[133] R. Koch, "A Calculation of Low-Energy pi N Partial Waves Based on Fixed t Analyticity," *Nucl. Phys.*, vol. A448, p. 707–731, 1986.

[134] G. Höhler, "Determination of πN resonance pole parameters," *πN Newsletter*, vol. 9, p. 1, 1993.

[135] T. P. Vrana, S. A. Dytman, and T. S. H. Lee, "Baryon resonance extraction from pi N data using a unitary multichannel model," *Phys. Rept.*, vol. 328, p. 181–236, 2000.

[136] M. Shrestha and D. M. Manley, "Multichannel parametrization of πN scattering amplitudes and extraction of resonance parameters," *Phys. Rev.*, vol. C86, p. 55203, 2012.

[137] H. Kamano, S. X. Nakamura, T. S. H. Lee, and T. Sato, "Nucleon resonances within a dynamical coupled-channels model of πN and γN reactions," *Phys. Rev.*, vol. C88, no. 3, p. 35209, 2013.

[138] V. Shklyar, H. Lenske, and U. Mosel, "η-meson production in the resonance-energy region," *Phys. Rev.*, vol. C87, no. 1, p. 15201, 2013.

[139] M. Batinic, S. Ceci, A. Svarc, and B. Zauner, "Poles of the Zagreb analysis partial-wave T matrices," *Phys. Rev.*, vol. C82, p. 38203, 2010.

[140] G. F. Chew and S. Mandelstam, "Theory of low-energy pion pion interactions," *Phys. Rev.*, vol. 119, p. 467–477, 1960.

[141] C. B. Chiu, "Evidence for regge poles and hadron collision phenomena at high energies," *Ann. Rev. Nucl. Part. Sci.*, vol. 22, p. 255–316, 1972.

[142] S. Mandelstam, "Dynamics Based on Rising Regge Trajectories," *Phys. Rev.*, vol. 166, p. 1539–1552, 1968.

[143] N. Isgur and J. E. Paton, "A Flux Tube Model for Hadrons in QCD," *Phys. Rev.*, vol. D31, p. 2910, 1985.

[144] M. G. Olsson, S. Veseli, and K. Williams, "Fermion confinement by a relativistic flux tube," *Phys. Rev.*, vol. D53, p. 4006–4012, 1996.

[145] C. Semay, F. Buisseret, N. Matagne, and F. Stancu, "Baryonic mass formula in large N(c) QCD versus quark model," *Phys. Rev.*, vol. D75, p. 96001, 2007.

[146] G. Veneziano, "Construction of a crossing - symmetric, Regge behaved amplitude for linearly rising trajectories," *Nuovo Cim.*, vol. A57, p. 190–197, 1968.

[147] W. H. Press, S. A. Teukolsky, W. T. Vetterling, and B. P. Flannery, *Numerical Recipes 3rd Edition: The Art of Scientific Computing*. New York, NY, USA: Cambridge University Press, 3 ed., 2007.

[148] D. Molina, M. De Sanctis, and C. Fernández-Ramírez, "Charmonium spectrum with a Dirac potential model in the momentum space," *Phys. Rev.*, vol. D95, no. 9, p. 94021, 2017.

[149] J. de Wiele and S. Ong, "Regge description of two pseudoscalar meson production in antiproton-proton annihilation," *Eur. Phys. J.*, vol. A46, p. 291–298, 2010.

[150] J.-J. Wu, R. Molina, E. Oset, and B. S. Zou, "Prediction of narrow N^* and Λ^* resonances with hidden charm above 4 GeV," *Phys. Rev. Lett.*, vol. 105, p. 232001, 2010.

[151] J.-J. Wu, R. Molina, E. Oset, and B. S. Zou, "Dynamically generated N^* and Λ^* resonances in the hidden charm sector around 4.3 GeV," *Phys. Rev. C*, vol. 84, p. 15202, 2011.

[152] W. L. Wang, F. Huang, Z. Y. Zhang, and B. S. Zou, "$\Sigma_c\bar{D}$ and $\Lambda_c\bar{D}$ states in a chiral quark model," *Phys. Rev. C*, vol. 84, p. 15203, 2011.

[153] Z.-C. Yang, Z.-F. Sun, J. He, X. Liu, and S.-L. Zhu, "The possible hidden-charm molecular baryons composed of anti-charmed meson and charmed baryon," *Chin. Phys. C*, vol. 36, p. 6–13, 2012.

[154] C. W. Xiao, J. Nieves, and E. Oset, "Combining heavy quark spin and local hidden gauge symmetries in the dynamical generation of hidden charm baryons," *Phys. Rev. D*, vol. 88, p. 56012, 2013.

[155] R. Aaij and Others, "Observation of $J/\psi p$ Resonances Consistent with Pentaquark States in $\Lambda_b^0 \to J/\psi K^- p$ Decays," *Phys. Rev. Lett.*, vol. 115, p. 72001, 2015.

[156] F.-K. Guo, C. Hidalgo-Duque, J. Nieves, and M. P. Valderrama, "Consequences of Heavy Quark Symmetries for Hadronic Molecules," *Phys. Rev. D*, vol. 88, p. 054007, 2013.

[157] L. Roca, J. Nieves, and E. Oset, "LHCb pentaquark as a $\bar{D}^*\Sigma_c - \bar{D}^*\Sigma_c^*$ molecular state," *Phys. Rev.*, vol. D92, no. 9, p. 94003, 2015.

[158] C. W. Xiao, J. Nieves, and E. Oset, "Heavy quark spin symmetric molecular states from $\bar{D}^{(*)}\Sigma_c^{(*)}$ and other coupled channels in the light of the recent LHCb pentaquarks," *Phys. Rev. D*, vol. 100, no. 1, p. 014021, 2019.

[159] Y. Yamaguchi, A. Giachino, A. Hosaka, E. Santopinto, S. Takeuchi, and M. Takizawa, "Hidden-charm and bottom meson-baryon molecules coupled with five-quark states," *Phys. Rev. D*, vol. 96, no. 11, p. 114031, 2017.

[160] M.-Z. Liu, Y.-W. Pan, F.-Z. Peng, M. Sánchez Sánchez, L.-S. Geng, A. Hosaka, and M. Pavon Valderrama, "Emergence of a complete heavy-quark spin symmetry multiplet: seven molecular pentaquarks in light of the latest LHCb analysis," *Phys. Rev. Lett.*, vol. 122, no. 24, p. 242001, 2019.

[161] T. J. Burns and E. S. Swanson, "Molecular interpretation of the $P_c(4440)$ and $P_c(4457)$ states," *Phys. Rev. D*, vol. 100, no. 11, p. 114033, 2019.

[162] M.-L. Du, V. Baru, F.-K. Guo, C. Hanhart, U.-G. Meißner, J. A. Oller, and Q. Wang, "Interpretation of the LHCb P_c States as Hadronic Molecules and Hints of a Narrow $P_c(4380)$," *Phys. Rev. Lett.*, vol. 124, no. 7, p. 72001, 2020.

[163] R. Zhu and C.-F. Qiao, "Pentaquark states in a diquark–triquark model," *Phys. Lett. B*, vol. 756, p. 259–264, 2016.

[164] A. Ali and A. Y. Parkhomenko, "Interpretation of the narrow $J/\psi p$ Peaks in $\Lambda_b \to J/\psi p K^-$ decay in the compact diquark model," *Phys. Lett. B*, vol. 793, p. 365–371, 2019.

[165] P. Holma and T. Ohlsson, "Phenomenological predictions for pentaquark masses

from fits to baryon masses," *Phys. Lett. B*, vol. 800, p. 135108, 2020.

[166] L. Maiani, A. D. Polosa, and V. Riquer, "The New Pentaquarks in the Diquark Model," *Phys. Lett.*, vol. B749, p. 289–291, 2015.

[167] S. X. Nakamura, "$P_c(4312)^+$, $P_c(4380)^+$, and $P_c(4457)^+$ as double triangle cusps," *Phys. Rev. D*, vol. 103, p. 111503, 2021.

[168] C. Fernandez-Ramirez, A. Pilloni, M. Albaladejo, A. Jackura, V. Mathieu, M. Mikhasenko, J. A. Silva-Castro, and A. P. Szczepaniak, "Interpretation of the LHCb Pc(4312) Signal," 2019.

[169] J. A. Silva-Castro, "On the possible virtual state nature of the lhcb pc(4312)+ signal," *Journal of Physics: Conference Series*, vol. 1610, p. 012015, sep 2020.

[170] A. Rodas and Others, "Determination of the pole position of the lightest hybrid meson candidate," *Phys.Rev.Lett.*, vol. 122, no. 4, p. 42002, 2019.

[171] R. J. Jaffe, "Multiquark hadrons. i. phenomenology of $Q^2\overline{q}^2$ mesons," *Phys. Rev. D*, vol. 15, pp. 267–280, Jan 1977.

[172] M. Alford and R. Jaffe, "Insight into the scalar mesons from a lattice calculation," *Nuclear Physics B*, vol. 578, no. 1, pp. 367–382, 2000.

[173] L. Maiani, F. Piccinini, A. D. Polosa, and V. Riquer, "New look at scalar mesons," *Phys. Rev. Lett.*, vol. 93, p. 212002, Nov 2004.

[174] G. 't Hooft, G. Isidori, L. Maiani, A. Polosa, and V. Riquer, "A theory of scalar mesons," *Physics Letters B*, vol. 662, no. 5, pp. 424–430, 2008.

[175] J. Weinstein and N. Isgur, "$K\overline{K}$ molecules," *Phys. Rev. D*, vol. 41, pp. 2236–2257, Apr 1990.

[176] T. Branz, T. Gutsche, and V. E. Lyubovitskij, "f0(980) meson as a K anti-K molecule in a phenomenological Lagrangian approach," *Eur. Phys. J. A*, vol. 37, pp. 303–317, 2008.

[177] J. R. Peláez and A. Rodas, "Dispersive $\pi\mathrm{K}\to\pi\mathrm{K}$ and $\pi\pi\to\mathrm{K}\bar{K}$ amplitudes from scattering data, threshold parameters, and the lightest strange resonance κ or K0$*$(700)," *Phys. Rept.*, vol. 969, pp. 1–126, 2022.

[178] R. Garcia-Martin, R. Kaminski, J. R. Pelaez, and J. Ruiz de Elvira, "Precise determination of the f0(600) and f0(980) pole parameters from a dispersive data analysis," *Phys. Rev. Lett.*, vol. 107, p. 072001, 2011.

[179] K. M. Watson, "The Effect of final state interactions on reaction cross-sections," *Phys. Rev.*, vol. 88, pp. 1163–1171, 1952.

[180] R. Garcia-Martin, R. Kaminski, J. R. Pelaez, J. Ruiz de Elvira, and F. J. Yndurain, "The Pion-pion scattering amplitude. IV: Improved analysis with once subtracted Roy-like equations up to 1100 MeV," *Phys. Rev. D*, vol. 83, p. 074004, 2011.

[181] P. Büttiker, S. Descotes-Genon, and B. Moussallam, "A new analysis of πK scattering from Roy and Steiner type equations," *Eur. Phys. J.*, vol. C33, pp. 409–432, 2004.

[182] J. Peláez and A. Rodas, "$\pi\pi \to K\bar{K}$ scattering up to 1.47 GeV with hyperbolic dispersion relations," *Eur. Phys. J. C*, vol. 78, no. 11, p. 897, 2018.

[183] D. H. Cohen, D. S. Ayres, R. Diebold, S. L. Kramer, A. J. Pawlicki, and A. B. Wicklund, "Amplitude analysis of the K^-K^+ system produced in the reactions $\pi^- p \to K^-K^+n$ and $\pi^+ n \to K^-K^+p$ at 6 GeV/c," *Phys. Rev.*, vol. D22, p. 2595, 1980.

[184] A. Etkin *et al.*, "Amplitude analysis of the $K^0_S K^0_S$ system produced in the reaction $\pi^- p \to K^0_S K^0_S n$ at 23-GeV/c," *Phys. Rev.*, vol. D25, p. 1786, 1982.

[185] R. S. Longacre *et al.*, "A measurement of $\pi^- p \to K^0_S\ K^0_S n$ at 22-GeV/c and a systematic study of the 2^{++} meson spectrum," *Phys. Lett.*, vol. B177, pp. 223–227, 1986.

[186] K. L. Au, D. Morgan, and M. R. Pennington, "Meson dynamics beyond the Quark Model: A study of final state interactions," *Phys. Rev.*, vol. D35, p. 1633, 1987.

[187] D. Morgan and M. Pennington, "New data on the $K\bar{K}$ threshold region and the nature of the $f_0(S^*)$," *Phys. Rev. D*, vol. 48, pp. 1185–1204, 1993.

[188] J. R. P. Sagredo and A. Rodas, "Dispersive study of $\pi\pi \to K\bar{K}$ scattering data up to 1.47 GeV.," *PoS*, vol. CD2018, p. 079, 2019.

[189] D. Morgan and M. R. Pennington, "f0 (S*): Molecule or quark state?," *Phys. Lett. B*, vol. 258, p. 444–450, 1991. [Erratum: Phys.Lett.B 269, 477 (1991)].

[190] D. Morgan, "Pole counting and resonance classification," *Nucl. Phys. A*, vol. 543, p. 632–644, 1992.